EVALUATING THE PHOTOCATALYTIC AND ANTIBACTERIAL ACTIVITY OF COPPER-DOPED TITANIUM DIOXIDE NANOPARTICLES

by

Naizhen Yu

Submitted in partial fulfillment of the requirements for the degree of Master of Science

at

Dalhousie University
Halifax, Nova Scotia
December 2022

Dalhousie University is located in Mi'kma'ki, the ancestral and unceded territory of the Mi'kmaq. We are all treaty people.

To my grandparents

TABLE OF CONTENTS

LIST OF TABLES

LIST OF FIGURES

ABSTRACT

Organic pollutants and pathogenic microbes exist in water systems causing many communities, especially in developing countries, to have a high risk of infection with water-borne diseases. Developing a simple, cost-effective, and efficient sunlight-driven water treatment technology is crucial for people to access clean and safe water. The most widely studied photoactive and antibacterial material is titanium dioxide (TiO_2) nanoparticles (NPs). TiO_2 NPs can produce highly reactive free radicals to oxidize organic pollutants and deactivate biological pollutants. However, pristine TiO_2 NPs have a large band gap and only harvest solar radiation in the UV region. This thesis focuses on developing copper-doped titanium dioxide ($TiCu_xO_2$) catalysts and exploring its photocatalytic activity in the visible-light region.

The first project focuses on synthesizing Cu-doped white TiO_2 ($wTiCu_xO_2$) NPs using the solvothermal approach. The second project is a comprehensive study on Cu-doped black TiO_2 ($bTiCu_xO_2$) NPs. The photocatalytic performance of the resulting $TiCu_xO_2$ catalysts (white and black particles) were evaluated using degradation of Rhodamine B (RhB) dye and disinfection of *Escherichia coli* (*E. coli*) under visible light irradiation. We show that introducing a Cu dopant and surface defects on the catalysts enhances its photodegradation ability. The mechanism of increased photocatalytic activity for $TiCu_xO_2$ is hypothesized to be due to band gap narrowing and accelerated charge separation. For disinfection ability, the activity might be related to the free Cu ions increasing the radical species under irradiation. In the project, I have developed two efficient photocatalysts for water treatment; the mechanistic studies of the nano-catalysts increase our understanding of the heterogeneous catalysts for photo-degradation of industrial dyes and inactivation of waterborne microbes, which are useful for engineering more efficient and sustainable water treatment devices.

LIST OF ABBREVIATIONS USED

A	Absorbance
AO	Ammonium Oxalate Monohydrate
AOPs	Advanced Oxidation Processes
BE	Binding Energy
BQ	1,4-benziquinone
BSEs	Back Scattered Electrons
$bTiCu_xO_2$	Copper-doped Black Titanium Dioxide
$bTiO_2$	Black Titanium Dioxide
CB	Conduction Band
CCD	Charged-coupled Device
CO_2	Carbon Dioxide
Cu	Copper
$Cu(OAc)_2$	Cupric Acetate Hydrate
Cu_2O	Cuprous Oxide
DMSO	Dimethyl Sulfoxide
E. coli	*Escherichia Coli*
EDTA	Ethylenediaminetetraacetic Acid
EJ	Exajoules
E_k	Kinetic Energy
FESEM	Field Emission Scanning Electron Microscope
H	Hydrogen
HAADF	High-angle Annular Dark-field

H_2O	Water
H_2O_2	Hydrogen Peroxide
HCl	Hydrochloride Acid
HR-TEM	High-resolution Transmission Electron Microscopy
$KBrO_3$	Potassium Bromate
LB	Luria Bertani
LPS	Lipopolysaccharides
MES	4-morpholineethanesulfonic Acid Monohydrate
$NaBH_4$	Sodium Borohydride
NaCl	Sodium Chloride
Nickel	Ni
NaN_3	Sodium Azide
NPs	Nanoparticles
O	Oxygen
O(1D)	Atomic Oxygen
O_3	Ozone
•OH	Hydroxyl Radicals
$O_2^{\bullet-}$	Superoxide Ions
•OOH	Hydroperoxyl Radical
OVs	Oxygen Vacancies
RhB	Rhodamine B
ROS	Reactive Oxygen Species
SEM	Scanning Electron Microscopy
SEs	Secondary Electrons

T	Transmittance
TEM	Transmission Electron Microscopy
Ti	Titanium
Ti^{4+}-OH	Titianol Group
$TiCu_xO_2$	Copper-doped Titanium Dioxide
TiO_2	Titanium Dioxide
TMB	3,3',5,5'-tetramethyl Benzidine
TS	Tryptic Soy
TTIP	Titanium Isopropoxide
UHV	Ultra-high Vacuum
UV-vis	Ultraviolet-visible
VB	Valence Band
$wTiCu_xO_2$	Copper-doped White Titanium Dioxide
$wTiO_2$	White Titanium Dioxide
XPS	X-ray Photoelectron Spectroscopy
XRD	X-ray Diffractions
λ	Wavelength

ACKNOWLEDGEMENTS

First, I would like to thank my supervisor, Dr. Mita Dasog. I will never forget she taught me how to do a great scientific work started from my first days in the lab. Every step she told me in detail such as experimental design, experiment set-up, and results collection and analysis, and encouraged and helped build my confidence. I clearly remembered how she introduced all experimental equipment and informed me of research details personally. When I struggled with the experimental results, Mita worked with me to analyze the results and go through each part of the experiment. She guided me to figure out problems and search-related literature, which let me have a new understanding of science and my research direction. She was the most excellent supervisor to teach me research knowledge and encourage me to explore new fields.

I would also like to acknowledge my co-supervisor Dr. Xu Zhang for supporting and helping me finish my master's degree. He always encourages me to do more experiments and sum up all the error experience. I would like to thank my committee member, Dr. Peng Zhang and Dr. Ken Oakes, who provided suggestions for this thesis.

I would like to thank both lab mates from Dalhousie University and Cape Breton University for their fellowship and helping on each presentation and practical. A special thank you to Reem Karaballi for training me on the synthesis procedures and technique experiments. I would like to thank Matt Margeson for XPS spectra training. I would like to thank Joseph Weatherby and Andrew Carrier for helping me to improve the writing skill. In addition, I have so appreciated everyone who has offered their services and/or guidance for the characterization of materials in this work: Collins Nganou (UV-vis spectrometer), Pat Scallion (SEM), Andy George (XPS), and Carmen Andrei (HR-TEM) and Judy

Maclnnis (TEM). Many thanks to all the professors and faculty at Dalhousie University and Cape Breton University who made an impact during my degree. I would like to especially thank Dr. Jennifer MacDonald for encouraging and helping me to complete the work as a teaching assistant in the first year. I would also like to thank Lea Gawne for all the administrative support during my graduate period.

Finally, I was grateful to my grandparents for always loving me and being there for me no matter how difficult it is, and thanks to my parents for doing so much for me over my years and my entire life.

CHAPTER 1. Introduction

1.1. Wastewater Treatment

Water resources have been contaminated because of industrialization and urbanization, and as a result wastewater management and environmental contamination have become one of the major challenges globally.[1,2] Organic, inorganic, and pathogenic microbe pollutants enter the aqueous system *via* multiple routes, including household sewage discharge, industrial waste disposal, reclaimed wastewater irrigation, and leaky sewer pipes etc.[3,4] If contaminants are not properly treated, such as improper disposal or direct discharge into the water, there would be an increased risk to public health. In 2020, almost 30 % of the people in the world cannot access a safe drinking water source, and 6% of deaths in low-income countries are the result of unsafe water sources.[5,6] The current techniques for water treatment involve chemical precipitation,[9] coagulation and flocculation,[7] filtration,[7] adsorption,[8] ion exchange,[9] etc.; however, these treatments produce sludge.[10] Due to economic, environmental and regulatory factors, sludge disposal is a huge challenge to the wastewater treatment plants.[11] Pollutants such as pesticides, dyes, aromatic compounds, and pathogenic microorganisms in a sludge cannot be removed efficiently and need costly and advanced treatment.[10,12,13] Further, the maintenance costs of such treatment facilities and the amount of energy consumed for secondary treatment are high. Developing a simple, cost-effective, green, and efficient water treatment technology would be a significant step in resolving this serious problem.

1.2. Advanced Oxidation Processes

Advanced oxidation processes (AOPs) are potential pathways for decomposing organic pollutants and disinfecting pathogenic microbes. AOPs depend on the production of highly reactive oxygen species (ROS) to oxidize and decompose pollutant molecules. The oxidation produces non-toxic by-products such as carbon dioxide (CO_2), water (H_2O) or specific inorganic compounds, i.e., salts, they undergo mineralization.[12,14,15] The AOPs are presented in **Figure 1.1**. During this process, hydroxyl radicals (•OH) are formed which have a high oxidation potential (2.80 eV) and can attack and decompose a broad class on pollutant molecules.[16]

Figure 1.1. The schematic diagram of AOPs.

Traditionally, the formation of •OH are based on ozone (O_3) or hydrogen peroxide (H_2O_2) reactions.[16] After absorbing high energy photon ($\leq$ 254 nm), O_3 can decompose to form molecular O_2 and atomic oxygen O (1D) (Eq. 1.1).[17] The •OH are formed by O (1D) reacting with water (Eq. 1.2).[18] Since the process requires consuming high energy photons to split O_3, it limits its utility due to cost and safety issues associated with the UV sources in this energy range.[17] H_2O_2 can also undergo photolysis to yield •OH; the quantum yield of the formed radicals is very high.[19] A maximum of two •OH form from one H_2O_2 molecule, as shown in Eq. 1.3.[19] However, high concentrations of

H_2O_2 drives the reaction to the left thus consuming •OH.[19] Adjusting the concentration of H_2O_2 to maintain a chemical reaction equilibrium is an outstanding challenge.[20] In addition, the raw reaction materials in both methods cannot be recycled, which will increase the cost of production and operation.[19]

O_3 based AOPs reactions:

$$O_3 + h\nu \rightarrow O_2 + O\ (1D) \qquad \text{Eq. 1.1}$$

$$O\ (1D) + H_2O \rightarrow 2\ \bullet OH \qquad \text{Eq. 1.2}$$

H_2O_2 based AOPs reactions:

$$H_2O_2 + h\nu \rightarrow 2\ \bullet OH \qquad \text{Eq. 1.3}$$

1.3. Solar-driven Photocatalysis

Solar power as clean energy is a potentially sustainable alternative to fossil fuels. The total potential energy production of solar irradiation is approximately 3,850,000 exajoules (EJ) per year,[22,23] almost twice as much as the energy produced from all the non-renewable resources on the earth.[21] The use of solar energy to generate highly active and renewable free radicals through AOPs is an attractive solution for water treatment proces.[22] The viability of this solution depends on many factors including the development of photocatalytic semiconductors that can harvest a broad light spectrum and generate large number of carriers to increase the free radical formation *via* and accelerate the photochemical reaction.[23–25]

The photocatalytic semiconductor has an energy band gap (E_g) that is the difference between the conduction band (CB) and valence band (VB).[26] As shown in **Figure 1.2**, the VB is filled with electrons.[26] The CB contains unoccupied electron states.[27] When a semiconductor absorbs a photon with energy larger than the band gap, the electrons in VB can be excited into the CB.[27] Simultaneously, a hole forms in the electron's place; creating an electron-hole pair.[27] These electron-hole pairs (i.e., charge carriers) can be transferred to adsorbed species on the semiconductor surface to participate in a series of chemical reactions, resulting in the decomposition of organic pollutants and inactivation of pathogenic bacteria.[28] However, if the electrons and holes are not used for photochemical reactions fast enough, they can recombine and release the absorbed energy as heat.[29]

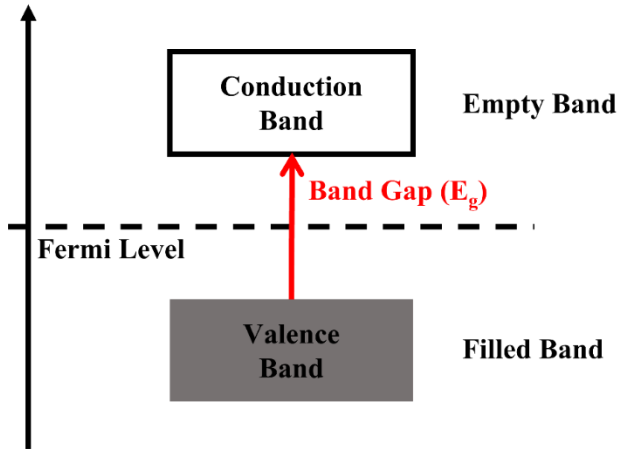

Figure 1.2. The schematic diagram of semiconductor band structure.

The band structure of the semiconductor determines the energy of the photons absorbed, electron-hole fate (separation, recombination, migration), and redox

capacities.[26] Thus, there are many avenues to design and modify the photocatalytic ability of semiconductors and are based on band gap engineering techniques.[27]

1.4. Titanium Dioxide

TiO_2 is the most common heterogeneous semiconductor applied for water treatment because of its chemical stability, nontoxicity, and high reactivity. Fujishima and Honda first reported the use of TiO_2 photocatalyst in 1972.[30] Initially, TiO_2 electrodes were used in solar energy driven water splitting to produce hydrogen gas (H_2).[30] In 1977, Frank and Bard found that TiO_2 can completely remove toxic species (cyanide) in oxygen saturated solution under ultraviolet (UV) illumination.[31] This is the earliest experiment in which TiO_2 had a photocatalytic capacity to treat toxic chemicals in water.

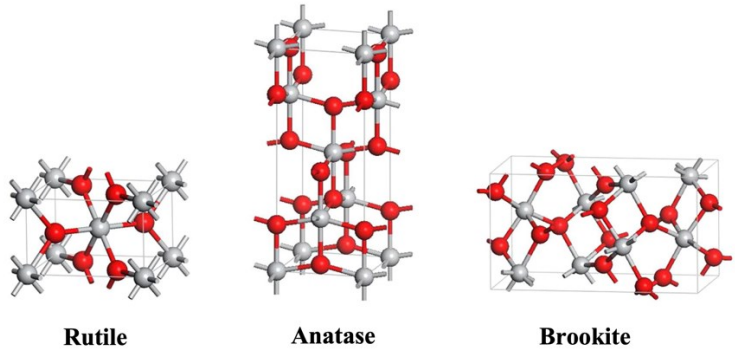

Figure 1.3. Crystal structures of three TiO_2 phases: rutile, anatase, and brookite.[32]

1.4.1. Polymorphs of TiO_2

TiO_2 has three crystalline polymorphs: anatase, rutile, and brookite, as shown in **Figure 1.3**.[33] Rutile and anatase are both tetragonal structures, containing six atoms in the unit cell.[34] Each titanium (Ti) atom is surrounded by six oxygen atoms, and each oxygen

(O) atom is surrounded by three Ti atoms to form a trigonal planar geometry.[34] Compared to the rutile phase, the anatase crystal is more distorted; both O-Ti-O bond angles in anatase deviate from 90 degrees.[34] The structure of the anatase phase is more unstable than the rutile phase in general.[35] The third crystalline polymorph is the brookite phase, composed of disordered octahedra. Six Ti-O bond angles and twelve O-Ti-O bond lengths are all different.[36] The different distortions of lattice structure determine the characteristics Ti-O bonds, which play an important role in the structure and electronic properties of TiO_2. Detailed information about the crystalline phases of TiO_2 discussed in this section are shown in **Table 1.1**.

Table 1.1. Structural information of TiO_2 crystalline polymorphs.[37]

Property	**Rutile**	**Anatase**	**Brookite**
Density (g/cm3)	4.13	3.79	3.99
Lattice Constant (Å)	a = 4.5936 c = 2.9587	a=3.784 c= 9.515	a=9.184 b=5.447 c=5.154
Space Group	$P4_2/mnm$	$I4_1/amd$	pbca
Dielectric Constant	114	31	14-110
Atoms Per Unit Cell	2	4	8
Ti-O Bond Length (Å)	1.949(4) 1.980(2)	1.937(4) 1.965(2)	1.87~2.04
O-Ti-O Bond Angle	81.2° 90.0°	77.7° 92.6°	77.7° ~ 105°
Bravais Lattice	Tetragonal	Tetragonal	Orthorhombic

Brookite TiO_2 has a complex synthesis procedure compared to anatase and rutile and is the least studied in heterogeneous photocatalysis.[38] Currently, anatase TiO_2 is the most widely used for photocatalytic applications.[38–40]. Copious studies show that anatase TiO_2 has much higher photocatalytic activity than rutile,[41–46] but the detailed mechanism and factors leading to the photocatalytic activity difference are still under debate.[47] Some possible explanations are summarized follows:

First, the band structure impacts the adsorption of surrounding molecules onto the anatase phase. Rutile has a broader sunlight absorbance because its band gap (3.02 eV) is smaller than that of anatase (3.20 eV). However, the large band gap places to the CB of anatase TiO_2 (-0.2 eV) is more negative than rutile (-0.02 eV), which raises the reducing ability of electrons and accelerates electron transfer from TiO_2 to adsorbed molecule, as shown in **Figure 1.4**.[39,48,49]

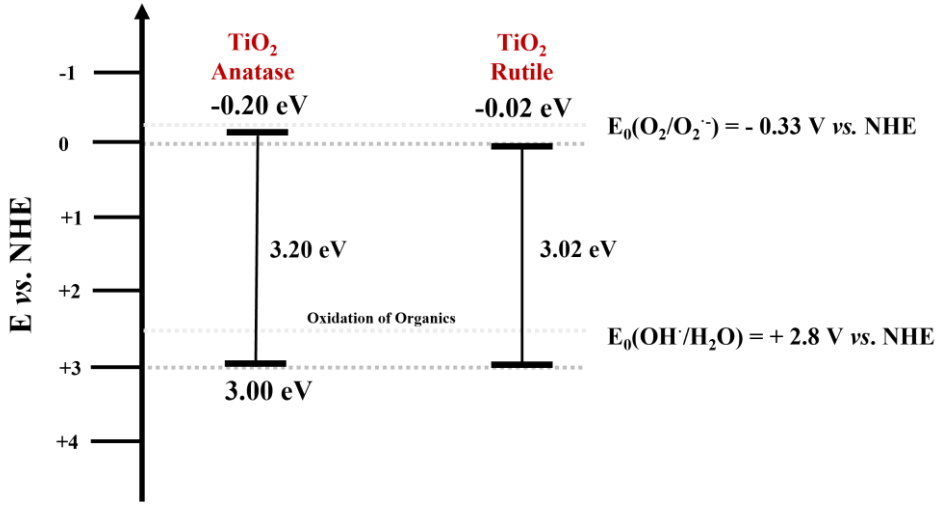

Figure 1.4. The energy band structure of rutile and anatase TiO_2.[50,51]

Second, the surface structures contribute to varying photocatalytic activity. The photocatalytic reactions mainly occur on the (101), (001), and, to a lesser extent, (100) crystal facets.[46] The Wulff shapes for anatase and rutile TiO_2 are shown in **Figure 1.5**. Anatase TiO_2 consists of a truncated tetragonal bipyramid exposing majority (101) and minority (001) facets where photocatalytic reactions occur.[46] The sharp crystals of anatase are dominated by (101) facets that constitute more than 94 % of the exposed surface,[52] with higher surface energy causing higher reactivity.[53] In addition, some literature reports that (101) facets can strongly adsorb small molecules such as water, oxygen etc.[46] However, most exposed facets of rutile are (110), with lower surface energy and reactivity.[46]

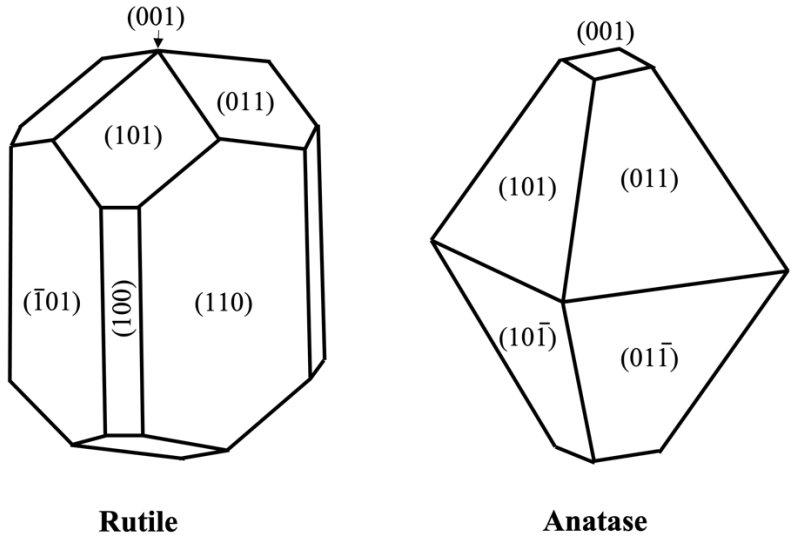

Figure 1.5. Equilibrium shape using Wulff construction for macroscopic crystals of rutile and anatase TiO_2. Adapted from Reference 54, Copyright Elsevier, 2003.

Third, the lifetime and diffusion length of electron-hole in anatase TiO_2 is impacted by its indirect band gap.[38,47] During charge carrier recombination, the excited electrons will release their extra energy as photons with a frequency corresponding to the band gap when they return from the CB to the VB. The band gap energy is represented by

Planck's equation (Eq. 1.4).[55] The excited electrons must follow the transition selection rule of momentum conservation (Eq. 1.5).[56]

Planck's equation:

$$h\nu = E_g \qquad \text{Eq. 1.4}$$

where E_g represents the photon energy, h is the Plank's constant, and ν is the frequency of the photon.

The transition selection rule for momentum conservation:

$$\hbar_1 k_{e(CB)} - \hbar_1 k_{e(VB)} = \hbar_1 q_{phonon} \qquad \text{Eq. 1.5}$$

where $\hbar_1$ is the reduced Planck's constant, $k_{e(CB)}$ and $k_{e(VB)}$ are the electron wave vectors at the CB_{minmum} and $VB_{maximum}$, respectively, q is the wave vector of the assisted phonon.[55]

As shown in **Figure 1.6**, rutile TiO_2 is a direct band gap semiconductor, whereas anatase is an indirect band gap semiconductor.[56] For rutile TiO_2, $k_{e(CB)} = k_{e(VB)}$, which gives a vertical transition, and an electron only emits a photon following the recombination of the photogenerated charge carriers.[56,57] But, for anatase TiO_2, $k_{e(CB)} \neq k_{e(VB)}$， with a non-vertical transition to the CB minimum that is shifted in the k-dimension representing that a vibration of the solid lattice (phonon) is coupled to electronic movement.[57] Therefore, the excited electrons cannot recombine directly with holes, resulting in an electron-hole pair lifetime increase in anatase relative to rutile,[58] enhancing photocatalytic activity.[39]

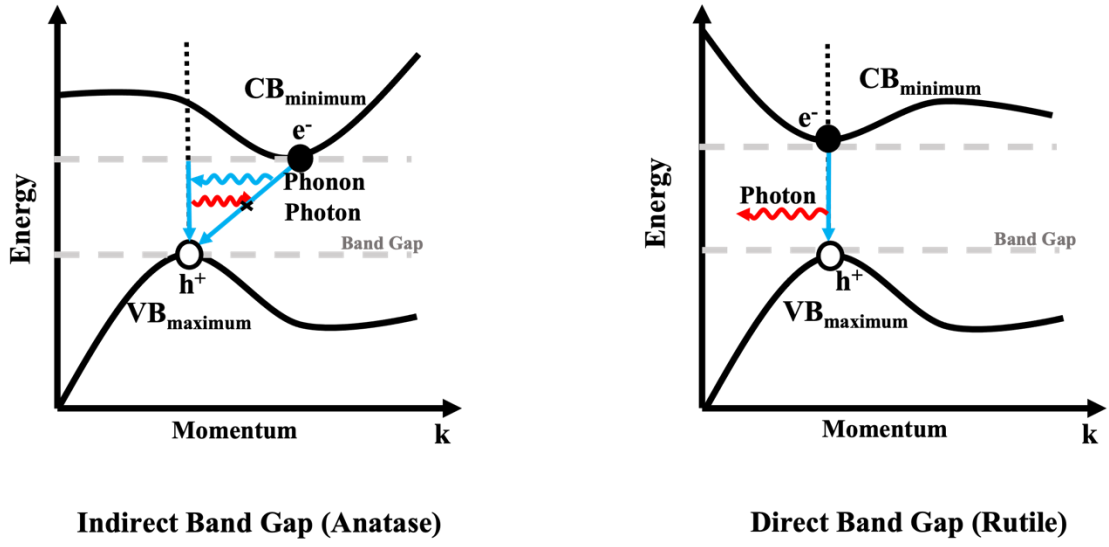

Figure 1.6. Schematic of recombination processes of photogenerated electrons and holes within indirect gap anatase and direct gap rutile TiO_2.[56]

The photocatalytic efficiency, ζ, is an indicator to evaluate the photocatalytic ability.[59] Although anatase TiO_2 has a higher photocatalytic efficiency than rutile, its ζ-values is still low (ζ-values <10%).[58] Limited solar energy harvesting and the low concentration of electron-hole pairs participating in photoredox reactions reduce the production of free radicals and restrict its applicability in water treatment. To address these issues, many efforts have been devoted to developing visible light active TiO_2-based photocatalysts with high electron-hole separation efficiency, mainly focusing on metal and non-metal doping.[60–62]

1.5. Methods for Enhancing the Photocatalytic Activity of TiO_2

Although anatase TiO_2 is more photocatalytically efficient than rutile, its wide band gap restricts anatase TiO_2 ability to harvest large portions of sunlight. Another limitation is rapid recombination of photogenerated carriers on its surface.[63] Currently,

metal and non-metal doping are popularly used for accelerating photocatalytic reactions. Doping narrows the band gap and broadens the absorbed range of wavelengths.[63]

1.5.1. Metal Modification

Metal doping is the process by which atoms in the lattice are substituted by other metals such as copper (Cu), iron (Fe), gold (Au), silver (Ag), and platinum (Pt), creating a new energy level below the conduction band,[64–67] as shown in **Figure 1.7**. Defect state appears in the band gap of the TiO_2 due to doping metal or vacancies.[67] Electrons can be excited from the defects state to the CB of TiO_2 by photons with the energy less than 3.2 eV.[68] The photocatalyst with narrowed band gap can shift the absorption from UV to visible light region of the solar spectrum. However, metal doped TiO_2 have a disadvantage. At high concentrations the metal dopant can form metal clusters, blocking the TiO_2 surface, and subsequently reducing light absorption and photocatalytic performance.[69]

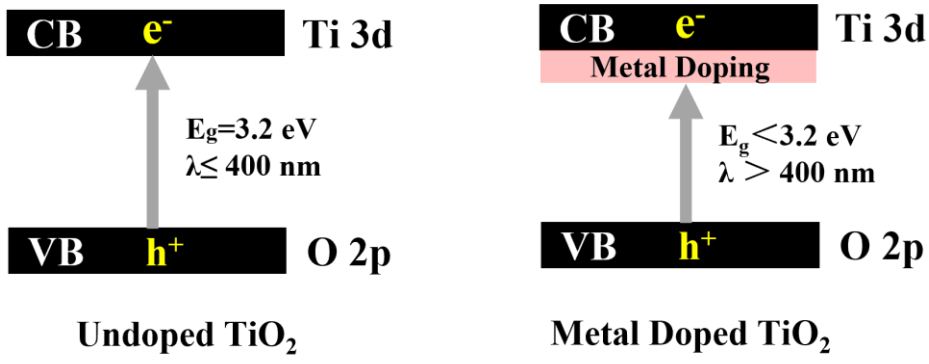

Figure 1.7. A schematic diagram comparing the band gap structure of undoped TiO_2 and metal doped TiO_2.

Noble Metal Doping

Deposition of noble metal NPs, such as Ag, Pt, and Au with a large work function, on the TiO_2 surface effectively retards electron-hole recombination because a Schottky barrier forms at the interface between the metal and TiO_2.[70]

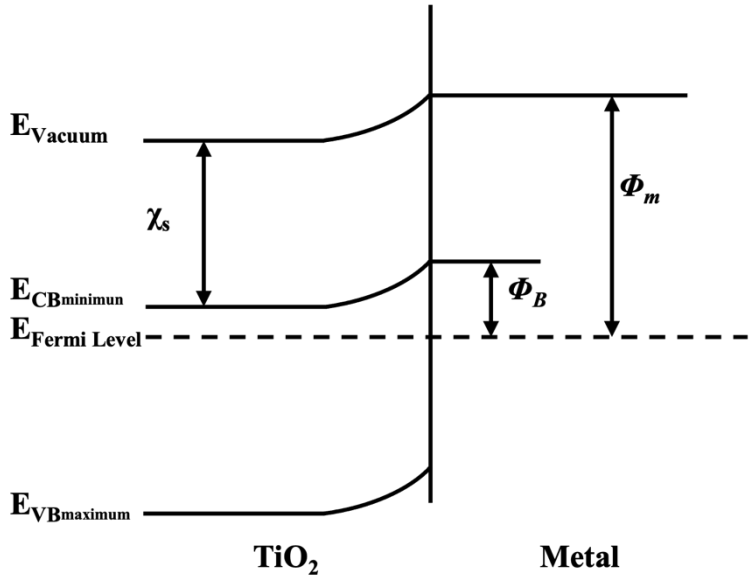

Figure 1.8. Schematic of a Schottky barrier between TiO_2 and a metal.[71]

As shown in **Figure 1.8**, metals have lower Fermi energies than semiconductors. When metals contact TiO_2, electrons flow from TiO_2 into the metal until different Fermi energies reach equilibrium.[71] Band bending occurs when an excess of positive charge in TiO_2 is generated from migrating electrons.[71] The bending at the interface creates a small barrier acting as an electron trap to prevent photogenerated electrons from flowing back to the TiO_2 surface.[71] This Schottky barrier is represented as follows:

$$\Phi_B = \Phi_m - \chi_s \quad \text{Eq. 1.6}$$

where Φ_B is the Schottky barrier, the energy difference between the Fermi level of the metal and the band edge of the TiO_2 that most carriers reside. Φ_m is the work function of the metal, and χ_s is the electron affinity of TiO_2.

Through this mechanism, the separated charge carriers then diffuse on the TiO_2 surface where photoredox reactions occur. Iliev *et al*. reported that high Ag doping on a TiO_2 surface improved the photodegradation of oxalic acid through Schottky barrier formation, which accelerated electron-hole pair separation and a higher rate of O_2 reduction.[72] However, Ag absorbs in the shorter wavelength region (320–450 nm) and does not benefit visible light absorption.[72] Au has better optical properties than Ag. In 2011, Rahulan *et al*., doped Au NPs onto TiO_2 to improve its light absorption. After Au doping, the new nanomaterials had high chemical stability and strong visible light absorption over a wide region (400–650 nm).[73]

Transition Metal Doping

The high cost and scarcity of noble metals have hindered their use in large-scale applications. Hence, current interest is in the use of Earth-abundant metals as TiO_2 dopants.[74] Transition metals, such as Fe and Cu, are abundant and have good light absorption properties.[74,75] These metal atoms either have or can produce cations with an incomplete d-subshell that can accommodate more electrons.[74,76] After doping TiO_2 with transition metals, the transition metal can trap photogenerated electrons or holes from the VB of TiO_2 to prevent charge carrier recombination.[76] The current transition metal doping method uses the corresponding transition metal salt as a dopant source, producing a

homogenized speciation throughout the TiO_2 matrix or surface.[77] Furthermore, transition metals in TiO_2 have two or more oxidation states that accelerate charge transfer at the interface.[78] For example, Fe oxidation states include Fe^{3+} and Fe^{4+}. Fe^{3+} traps photogenerated holes and forms Fe^{4+}.[78] Then, Fe^{4+} further reacts with photogenerated electrons to produce Fe^{3+}.[78] During the process, the separated holes and electrons continuously produce to participate in photocatalytic reactions.[78]

Cu is a typical transition metal and many studies report Cu is an effective dopant for TiO_2.[79–84] Like most transition metals, Cu narrows the band gap of TiO_2, shifting the light absorption edge. It also has more than two oxidation states that enhance photocatalytic activity.[85] The most common oxidation states of Cu are Cu^+ and Cu^{2+}. Cu^+ is unstable and is rapidly oxidized in the presence of oxygen (Eq. 1.7).[86] Cu^{2+} can continuously react with superoxide ions ($O_2^{\bullet-}$) to produce Cu^+ (Eq. 1.8).[86]

$$Cu^+ + O_2 \rightarrow Cu^{2+} + O_2^{\bullet-} \qquad \text{Eq. 1.7}$$

$$Cu^{2+} + O_2^{\bullet-} \rightarrow Cu^+ + O_2 \qquad \text{Eq. 1.8}$$

Therefore, Cu^+ or Cu^{2+} rapidly interconvert. During this process, $O_2^{\bullet-}$ are generated, which can kill pathogenic bacteria.[86] Even in the dark, the Cu^+ modified TiO_2 also is easily excited by surrounding oxygen to kill microbes.[87] However, because Cu^{2+} is more stable to oxygen than Cu^+, the redox reaction needs to be excited in heterogeneous systems on TiO_2 surfaces. After Cu^{2+} trapped electrons from CB in TiO_2 to produce Cu^+, a Cu photoredox cycle is to build (Eq. 1.9).[88]

$$Cu^{2+} + e^- \rightarrow Cu^+ \qquad \text{Eq. 1.9}$$

Wetchakun *et al*. synthesized Cu^{2+}-doped TiO_2 NPs with the band gap energy of 2.83 eV *via* the sol-gel method, which mineralized oxalic and formic acid under visible light.[89] The Cu dopant acted as an electron acceptor and retarded the electron-hole recombination to enhance the photocatalytic reaction.[89] However, a large amount (5.0 mol%) of Cu decreased the TiO_2 surface area, whereas 2.0 mol% Cu doping was the optimum amount to obtain a sufficient surface area for increased acid adsorption.[89] This result may be caused by different amounts of Cu modified the surface properties of TiO_2. Because of the charge imbalance, when Ti is replaced by Cu a high amount of oxygen vacancies (OVs).[90] The ionic radii of six-fold coordination of Cu^{2+} ions (0.7 Å) is higher than that of Ti^{4+} (0.6 Å).[91] Dopant incorporation can cause tensile strain that results in crystalline size increase.[89] Still, a high dopant concentration can take positions on the surface or interstitial sites of TiO_2 matrices and decrease its surface area.[91] Therefore, controlling the dopant concentration is important to improve the surface properties of synthesized materials.[91]

Advantages and Disadvantages of Metal Doping

Metal doped TiO_2 enhances the visible light absorbance of TiO_2, increasing its applicability. Noble metal dopants enhance photocatalytic ability through localized surface plasmon resonance effects. Readily absorbed photons to migrate electrons in TiO_2 from the VB to the CB. However, TiO_2 decorated with noble metal NPs also reduces electron-hole pair recombination, especially for highly loading samples (> 5%).[92] When negative electrons from the metal accumulate at the interface, the noble metal center develops a negative charge that attracts holes and reduces charge carrier separation.[92] In addition, the high cost of noble metal dopants limits their large-scale application in practical industry.

Transition metals are Earth-abundant and low-cost, so these metals and their compounds have drawn increasing attention as candidates for photocatalytic applications. The photocatalytic enhancement by transition metal dopants mainly relies on trapping photogenerated electrons in the incomplete d-subshell to prevent charge carrier recombination. Additionally, cationic dopants create an energy level under the CB of TiO_2 or create a defect state by triggering the formation of Ti^{3+} and thus lower the band gap. However, excessive doping can decrease photocatalytic activity by occupying surface or interstitial sites and reducing surface area. The adsorption capacity of TiO_2 can affect the photodegradation of organic compounds, especially dyes. If the surface area is reduced, the adsorption area and capacity are also impacted.

Furthermore, all metal doped materials have the same problems: metal doped TiO_2 leaches metal ions into the water and soil and are difficult to remediate. Leached cations, such as Pb and Cr, accumulate in ecosystems and cause toxic effects.[93] Thus, evaluating metal ion leaching is crucial for reducing the risk of metal toxicity and protecting the environment.[60]

1.5.2. Non-metal Modification

Like metals, non-metals have also been doped into TiO_2 nanomaterials to enhance visible light absorption. Doping TiO_2 with non-metals such as carbon (C), nitrogen (N), and hydrogen (H) has received much attention.[60,62]

C-or N-doped TiO_2

Among non-metal dopants, C and N have received the most attention. Compared to metal dopants, non-metal doped TiO_2 can more effectively inhibit charge carrier recombination.[60] As shown in **Figure 1.9**, the impurity states in non-metal doped TiO_2 are near the VB edge but do not act as electron accumulation sites; their role as recombination centers might be minimized.[62] In C-doped TiO_2, the substitutional C atom in the TiO_2 matrix introduces new states (C 2p) close to the VB edge of TiO_2 (O 2p), resulting in the VB edge shifting to higher energy and narrowing the band gap.[94] Yang et.al. fabricated C-doped anatase TiO_2 that exhibited high trichloroacetic acid (TCA) photodegradation under visible light irradiation.[95] Wong *et al*. further analyzed the factor that C-doped TiO_2 may improve.[95] Their explanation included (1) C increases the surface area of the doped TiO_2, which could provide more active sites and adsorb more reactive species for photodegrading targeted pollutants in water and (2) the incorporation of C atoms into TiO_2 introduces lattice defects and OVs that contribute to the absorption of visible light and to the photocatalytic effect.[96]

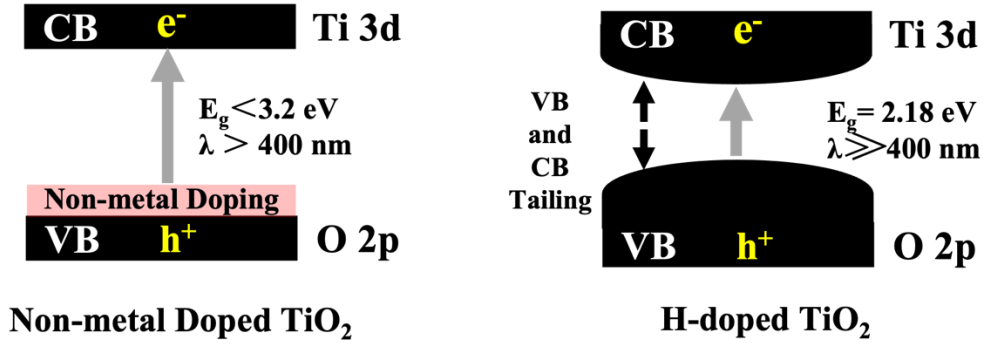

Figure 1.9. Schematic of the band gap structure of non-metal doped TiO_2 and an example of H-doped TiO_2; The disorder layer creases broadened tails of states extending into the forbidden band gap.

Although C-doped TiO_2 has visible light activity, the states introduced by C are too deep in the gap and it cannot overlap sufficiently with the band states of TiO_2 to transfer photoexcited carriers to reactive sites at the catalyst surface within their lifetime.[97] If photoexcited carriers do not transfer to reactive sites completely, the downstream photoredox reaction will be impacted, resulting in insufficient pollutant mineralization.[98] Compared to C, the states introduced by N are lightly shallow because the ionic radius of N (1.71 Å) is greater than the ionic radius of O (1.4 Å).[78] N-doped TiO_2 currently exhibits the greatest optical response to solar radiation among traditional non-metal doping.[99]

H-doped TiO_2

Both metal doping and non-metal doping can improve the solar absorption characteristics of TiO_2. An important factor is that Ti^{3+} defects and OVs generated *via* metal replacement of Ti atoms or non-metal replacement of O atoms reduces electron-hole pair recombination and extend the optical response. However, traditional non-metal doping, and metal doing do not extend absorption sufficiently in the visible and infrared region.[100] H-doped TiO_2 is an alternative approach to improving visible and infrared optical absorption.[101] H-doping does not make a substantial contribution to the CB or VB state.[101] Rather a mid-gap state is introduced by lattice disorder generated by Ti and O atom defects after hydrogenation.[102]

The structure of H-doped TiO_2 includes a TiO_2 nanocrystal as a core and a highly disordered surface layer where dopants are introduced (**Figure. 1.10**).[103] The retained core benefits the photocatalytic process, and the disordered layer benefits enhancing visible and infrared absorption and carrier trapping.[104] Chen *et al*. showed that large amounts of lattice

disorder in TiO_2 yielded mid-gap states that form a continuum extending to overlap with the CB edge (**Figure 1.9**).[103] This extended state is known as the band tail state and merges with the VB.[104] The band tailing in the VB is much stronger than in the CB.[100] The engineered disorder provides trapping sites for photogenerated carriers and inhibits their rapid recombination, thus promoting photocatalytic reactions.[105] The mechanism is attributed to various defective species such as Ti^{3+} defects, OVs, interstitial Ti, and interstitial O, H atoms forming surface OH bonds with oxygen (OH-surface), etc., but the composition of the defects is affected by different synthetic approaches.[101] The most typical defect species that contribute to photocatalytic activity include OVs and Ti^{3+} defects.[105]

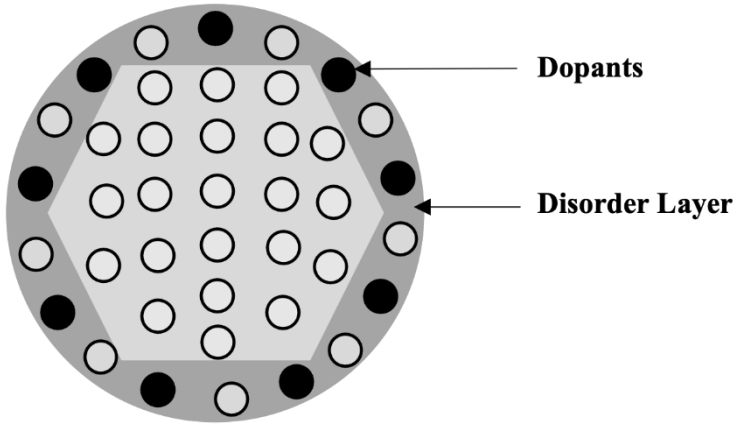

Figure 1.10. Schematic of the structure of $bTiO_2$ in the form of a disorder-engineered nanocrystal with H-dopant incorporation. Doping site are shown as black dots, and disorder is represented in the outer layer of the nanocrystal.[103]

OVs and Ti^{3+} defects highly correlate to the promotion of light absorption, chemisorption, and electron-hole pair separation and lead to superior photocatalytic properties.[106] Typically, H-doped TiO_2 is black and referred to as black TiO_2 ($bTiO_2$).[107]

OVs and Ti^{3+} defects extend the TiO_2 photoresponse range from UV to the infrared and visible light region.[102] Song *et al*. fabricated bTiO_2 with large visible and infrared light absorption corresponding to an increased number of OVs.[108] OVs introduced mid-gap states that allowed electrons to be excited by lower energy photons.[108] OVs are lattice sites missing O atoms.[109] These form moderately deep electron traps (trap depth 1.3−2.7 eV) that inhibit charge carrier recombination.[109] In addition, according to Malwadkar et.al, O_2 irreversibly and dissociatively adsorbs on defective surface sites with excess negative charges.[110] During the photocatalytic process, electrons are excited to the surface and trapped by OVs, which develop excess negative charges and subsequently absorb O_2.[111] The absorbed O_2 are then activated to promote photoredox reactions. Conversely, Ti^{3+} sites preferentially absorb water.[110] As shown in **Figure 1.11**, after adsorption, water diffuses along the Ti rows and dissociates into a bridging Ti^{3+}-OH.[112] Adsorbed water or surface OH groups can be oxidized to •OH, which subsequently degrade organic pollutants.[112] Some studies suggest Ti^{3+} is an active hole trapping site, but this is still controversial.[113]

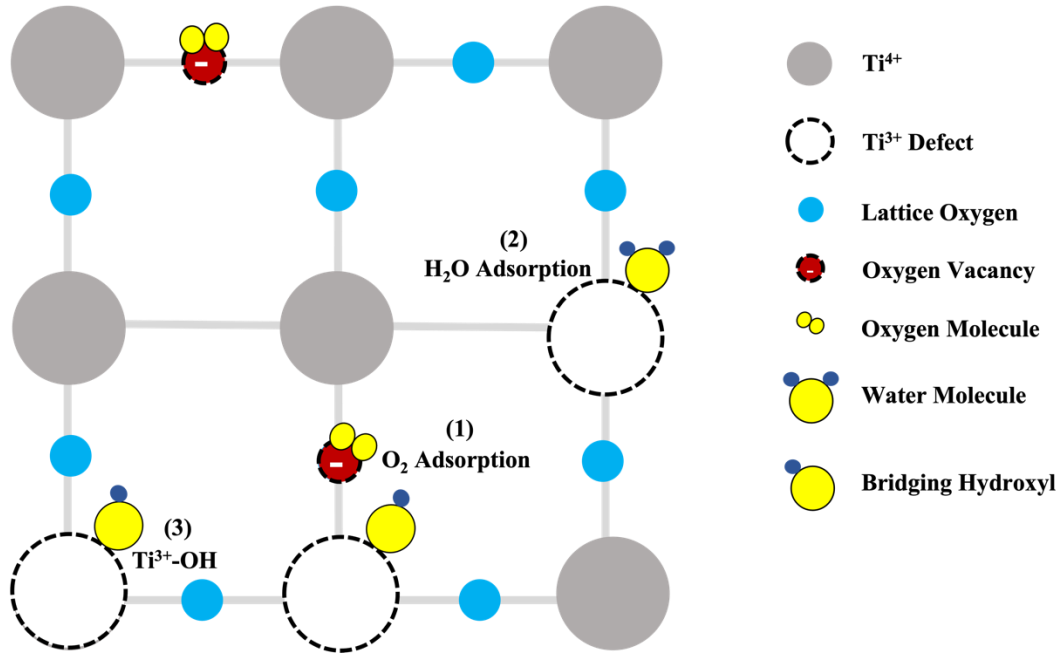

Figure 1.11. Proposed model for the O_2 and H_2O adsorption on $bTiO_2$. (1) An oxygen vacancy is filled by O_2. (2) Ti^{3+}defect is filled by H_2O. (3) Two OH groups are dissociated into a bridging Ti^{3+}-OH.[112]

Although OVs and Ti^{3+} defects in $bTiO_2$ contribute to the increased light-harvesting properties, defects formed at a high annealing temperature result in electron-hole pair recombination and a decrease in photocatalytic efficiency.[104] OVs and Ti^{3+} defects can occur on the surface or in the bulk.[104] Surface defects serve as charge carrier traps and adsorption sites where charge transfer to adsorbed species accelerates electron-hole separation; however, bulk defects only act as charge carrier traps where electron-hole pairs recombine.[114] Surface defects are unstable, and are easily impacted by high annealing temperatures that increase their size and the electron-hole recombination rate.[115] In addition, high temperatures can cause excess bulk defects *via* Ti^{3+} diffusion into TiO_2 interstitial sites causing phase transformation from crystalline to amorphous

structure.[114,115] This phase transformation may decrease the photocatalytic properties.[116] Thus, tuning the surface/bulk defects of TiO_2 nanocrystals is a key to improving the photocatalytic performance of $bTiO_2$.[101] Currently, sodium borohydride ($NaBH_4$) treatment is a practical and common approach to effectively tune the surface and bulk defects of $bTiO_2$.[117] This method will be discussed in detail in Chapter 3.

Advantages and Disadvantages of Non-metal Doping

Like metal doping, non-metal doping of TiO_2 increases visible light harvesting. An advantage of non-metal doped TiO_2 includes simple and cost-effective synthetic methods, inexpensive doping materials, using unsophisticated equipment *etc*. However, all methods have drawbacks. As described above, C-doping can increase the surface area, but strong adsorption prevents the complete mineralization of organic pollutants. $bTiO_2$ has defects that inhibit charge carrier recombination, but these defects are unstable during high temperature annealing. Optimizing synthetic approaches is required to improve the photocatalytic activity of $bTiO_2$. Single doping methods always have limitations. Thus, scientists recommended exploring the effect of co-doping TiO_2 with non-metals and metals.

1.6. Photocatalytic Mechanism of TiO_2

The primary mechanism of TiO_2 photocatalysts are interfacial redox reaction of electrons and holes that are produced after sufficient exposure to solar energy. The main steps are shown in **Figure. 1.12,**[58] which includes: 1) light absorption, 2) charge carrier recombination, 3) hole trapping, 4) electron trapping, 5) initiating an oxidative pathway by a hole in VB, (6) initiating a reductive pathway by an electron in CB, and 7) further

thermal and photocatalytic reactions to attack microbes (7A) and decompose organic dye (7B).[58]

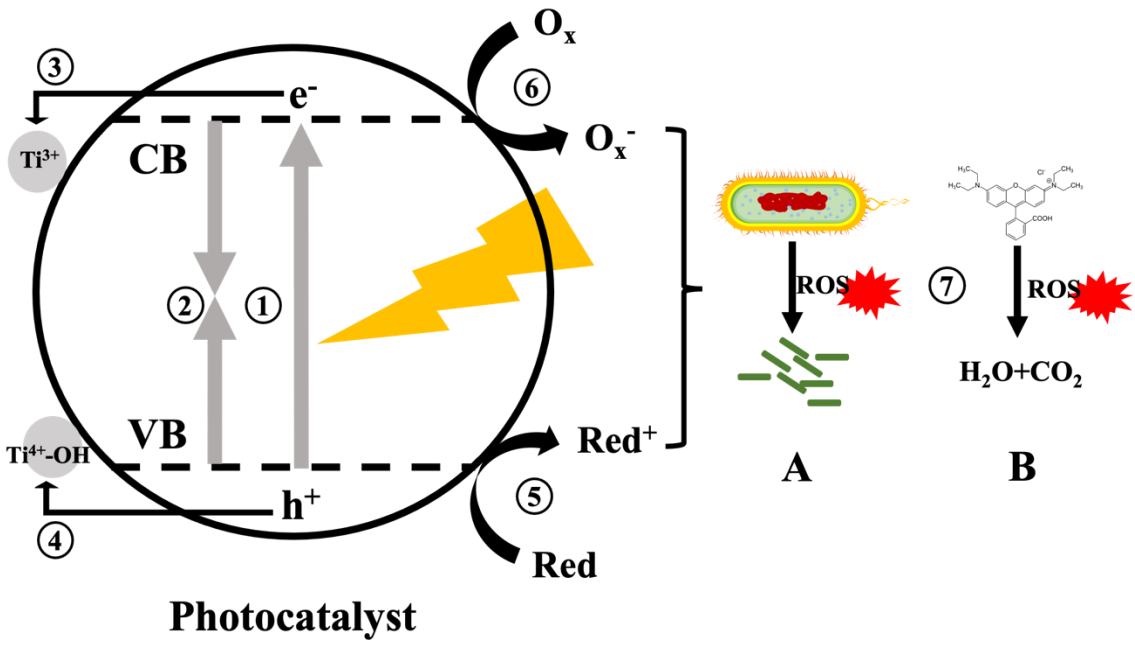

Figure 1.12. Main steps in the mechanism of TiO_2 photocatalysis: (1) production of electron-hole pairs by photon absorption; (2) charge carrier recombination; (3) trapping of an electron in CB; (4) trapping of a hole in VB; (5) initiation of an oxidative pathway by a hole in VB; (6) initiation of a reductive pathway by an electron in CB; (7) further hydrolysis and photocatalytic reactions to decompose dye (7A) or attack microbes (7B). Adapted from Reference 58, Copyright 1995 American Chemical Society.

1.6.1. Light Absorption

In step (1), the light absorption process is very fast and ranges in femtoseconds.[118] The photocatalytic reaction is initiated by the energy of an absorbed photon exceeding the band gap energy of TiO_2. The solar light at the Earth's surface includes wavelengths in the UV, visible, and infrared (IR) regions.[119] Of these,

approximately 4% of the sunlight is in the UV region (wavelengths from 300 to 400 nm), and approximately 45% is in the visible range (400 to 760 nm).[120] The absorbance of traditional white TiO_2 ($wTiO_2$) is below 400 nm, greatly limiting the photocatalytic efficiency.[121]

1.6.2. Electron-hole Pairs Generation, Recombination, and Separation

Light energy excites TiO_2 photocatalyst to form electron and hole pairs, as shown in Eq. 1.10. The excited electrons in CB and holes in VB can either recombine or can be separated by getting trapped in the surface defect sites such as Ti^{3+} and titanol group ($Ti(^{4+})$-OH) or reacting with electron donors and electron acceptors that are adsorbed on the TiO_2 surface.[58]

Charge carrier generation:

$$TiO_2 + h\nu \rightarrow h_{VB}^{+} + e_{CB}^{-} \qquad \text{Eq. 1.10}$$

The electron-hole pairs usually recombine in the absence of suitable electron and hole scavengers (Step (2)). When these scavengers are located at the surface of TiO_2, such as Ti^{4+} and Ti^{4+}-OH, the excited-state electrons and holes will be trapped separately to inhibit recombination (Step (3) and Step (4)).[122] Electrons are trapped in Ti^{3+} (Eq. 1.11); this process is irreversible due to electrons in Ti^{3+} being in deep trap states. Ti^{4+}-OH contributes to hole trapping to form •OH, as shown in Eq. 1.12.[123] The reason is that the standard redox potential $E^0(OH_{aq}^{-}/\bullet OH_{aq}) = 1.9$ V (vs normal hydrogen electrode, NHE) and E^0 ($H_2O_{aq}/\bullet OH_{aq} + H_{aq}$) = 2.73 V (vs NHE) are located at a less positive potential than VB edge of TiO_2, which causes holes to produce •OH. [123] The •OH contains free-state and

surface-bound •OH ($[Ti^{4+}– •OH]^{+}$).[124] The free •OH participates in redox reactions on the interface of TiO_2.[125] Excessive $[Ti^{4+}– •OH]^{+}$ can recombine with electrons, as shown in Eq. 1.14. Also, an electron can be shallowly trapped by $Ti^{4+}– OH$ (Eq. 1.13) to form $Ti^{3+}–$ OH that can recombine with holes (Eq. 1.15).[123]

Charge Carrier Separation:

$$e_{CB}^{-} + Ti^{4+} \rightarrow Ti^{3+} \qquad \text{Eq. 1.11}$$

$$h_{VB}^{+} + Ti^{4+}\text{-}OH \rightarrow [Ti^{4+}– •OH]^{+} \qquad \text{Eq. 1.12}$$

$$Ti^{4+}– OH + e_{CB}^{-} \rightarrow Ti^{3+}– OH \qquad \text{Eq. 1.13}$$

Charge Carrier Recombination:

$$[Ti^{4+}– •OH]^{+} + e_{CB}^{-} \rightarrow Ti^{4+}– OH \qquad \text{Eq. 1.14}$$

$$Ti^{3+}– OH + h_{VB}^{+} \rightarrow Ti^{4+}– OH \qquad \text{Eq. 1.15}$$

There are two competitions between the charge carrier recombination process and the charge carrier trapping process (picoseconds to nanoseconds) followed by the competition between trapped carrier recombination and interfacial charge transfer (microseconds to milliseconds).[58] Higher quantum efficiencies for steady-state photolysis can be achieved by increasing the recombination lifetime of charge carriers and the interfacial electron-transfer rate constant.[126] Simply, if electron-hole pairs are in a de-trapping state, the electrons or holes can be free to be activated, not be recombined.[126]

1.6.3. The Initiation of Oxidative and Reductive Pathway

The oxidative and reductive pathway for the reaction is initiated from electron-hole pairs that migrate to the surface of the TiO_2 photocatalyst. The free electron-hole pairs react with adsorbed species such as oxygen and water to form ROS, which is a type of highly active free radical, that can attack pathogenic microbes (step (7A) organic pollutants (step (7B)).

1.7. Motivation

TiO_2 has become an excellent candidate for water purification through its photocatalytic decomposing pollutant degradation and antibacterial properties. To obtain higher photocatalytic efficiency and broaden their use, pristine TiO_2 catalysts require further engineering of their morphological properties, crystalline structure, particle size, and surface area.[127–131] Currently, TiO_2 modified *via* metal and non-metal doping has shown that both methods improve the photocatalytic ability relative to pristine TiO_2.[28]

The main concerns during water treatment are the removal of organic pollutants and pathogenic microbes. Modified TiO_2 *via* Cu-, Fe-, Au-, Ag- and Pt-doping are effective in removal of environmental pollutants *via* photocatalytic process.[78] However, Au, Ag and Pt are limited for long-term environmental treatment because of cost concerns, legal restrictions, and human health impact. For the Earth abundant metals, Fe has lower antibacterial performance than Cu. In all form factors, Cu and Cu compounds are the most widely used dopants in efforts to enhance the photocatalytic and antibacterial properties of TiO_2.

This thesis reports the successful use of a new modified TiO_2 photocatalyst ($TiCu_xO_2$ NPs) to degrade the organic dye and destroy pathogenic microbes. These photocatalyst NPs are modified pristine TiO_2 with optimal light adsorption ability and ROS generation to accelerate photocatalytic reactions. Cu-doping improves light absorption, electron-hole separation, and antibacterial properties. Because single element doping in TiO_2 limits broad solar spectrum harvesting, I further modified $TiCu_xO_2$ NPs from white to black by hydrogenated treatment. The treatment aims to narrow the band gap, enhance the optical properties, and provide superior photocatalytic abilities relative to white modified catalysts.

The motivation for the research presented in this thesis was to systematically investigate how various parameter affects the photocatalytic and antibacterial performance of $TiCu_xO_2$ NPs. Chapter 3 details the synthetic approach to $TiCu_xO_2$ catalysts, and further investigates the influence of their surface characteristics, metal doping, and H-doping on the photocatalytic activity. Chapter 4 focuses on the best Cu-doping concentration for enhancing photodegradation ability and analyzing the photodegradation mechanism of $TiCu_xO_2$ NPs *via* the ROS scavenger tests. Chapter 5 investigates the best antibacterial performance of $TiCu_xO_2$ catalyst and describes the possible factors for inhibiting bacterial growth. By analyzing the dye degradation kinetics and bacterial inhibition of various catalysts, I determined that lower Cu dopants effectively photodegrade dyes, whereas higher Cu doping concentration benefit killing microbes. Based on all analyses, optimizing the Cu doping concentration may make Cu-doped nanomaterials more widely used in water treatment.

CHAPTER 2. Theory and Details of Characterization Techniques

The photocatalysts synthesized in this thesis were characterized using various techniques to understand their crystallinity, morphology, surface chemistry, and optical properties. A brief summary of the theory and instrumentation details of various techniques used in this thesis are outlined in this chapter.

2.1. Powder X-ray Diffraction

X-rays are electromagnetic radiation with a short wavelength and high frequency. The wavelength and frequency ranges from 10^{-8} to 10^{-12} meters and 10^{16} to 10^{20} hertz, respectively, for X-rays.[132] Powder x-ray diffractometer (XRD) consists of three main components: an X-ray tube, a sample holder and an X-ray detector, as shown in (**Figure 2.1**).[133]

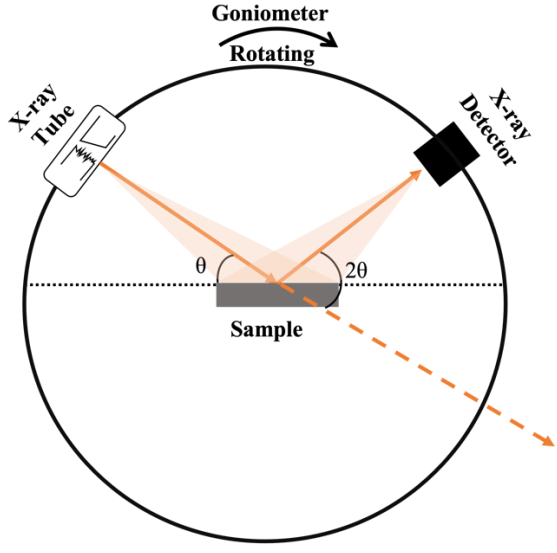

Figure 2.1. A schematic diagram of powder X-ray diffraction. There are three main components: 1) X-ray source, 2) sample holder, and 3) detector.[133]

First, in the cathode ray tube electrons are produced by heating a filament and these electrons are accelerated towards a metal target by applying voltage.[134] When voltage increase from the threshold to the excitation voltage, the electrons will have enough energy to eject inner shell electrons of the target material and produce characteristic X-rays.[135] **Table 2.1** lists some common target materials and the wavelength of the X-ray produced from these metals.

Table 2.1. The characteristic wavelength of common X-ray targets in nm.[133]

Target	$K_{\alpha 1}$	$K_{\alpha 2}$	K_{α} mean	K_{β}
Cr	0.22896	0.22935	0.22909	0.20849
Mn	0.21019	0.21058	0.21031	0.19102
Fe	0.19360	0.19399	0.19373	0.17566
Co	0.17889	0.17928	0.17902	0.16208
Cu	0.15405	0.15444	0.15418	0.13922
Mo	0.07093	0.07135	0.07107	0.06322

Cu is the most common target material.[133] Electrons from the cathode with sufficient energy hit the electron in the K-shell of the target material. The K-shell electron is dislodged to produce a hole in the empty position.[136] According to the selection rule, the electron in L-shell (2p) will transit to K-shell to fill the hole.[136] At the same time, X-rays corresponding to the energy difference between the two energy states will be emitted and are called K_{α}.[137] Similarly, when the electron from M-shell fills the 1s, the X-ray is called K_{β}. These processes are summarized in **Figure 2.2**. In general, the intensity of K_{α} is stronger than K_{β}.[138] Furthermore, in the transition (2p to 1s), the 2p orbital split different

states, $K_{\alpha 1}$ and $K_{\alpha 2}$.[138] $K_{\alpha 1}$ and $K_{\alpha 2}$ are usually used for XRD, and K_{β} will be cut off by a nickel (Ni) filter.[139]

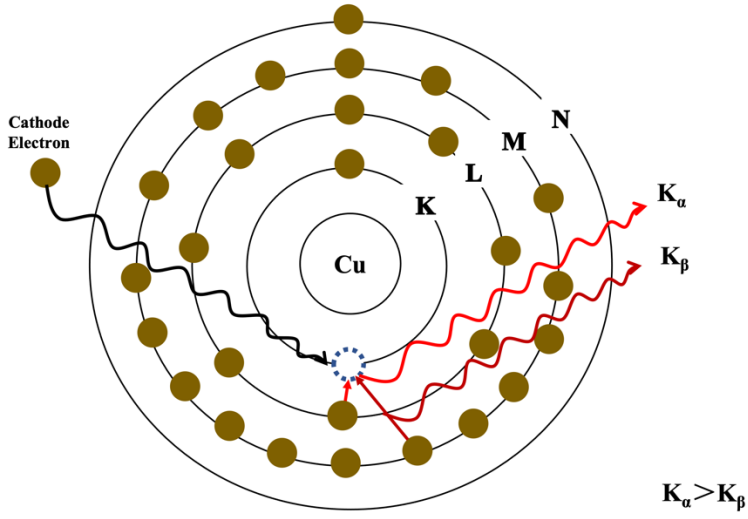

Figure 2.2. The electronic transitions in Cu atoms to generate K_{α} and K_{β} X-rays.

The atoms in crystalline materials are arranged uniformly with a characteristic spacing between the planes. Atoms diffract incoming X-rays when they strike the surface of a crystal and the non-scattered X-rays continue through the material and can be scattered by the next layer, and so on.[133] If beams diffracted by different layers are in-phase, the resulting constructive interference will result in a peak in the diffraction pattern. Alternatively, when the diffracted X-rays are out-of-phase destructive interference will result in no peak detected.[133] As shown in **Figure. 2.3**, the distance between two lattice planes is represented by *d*. When incident X-rays with wavelength (λ) strike the plane (1), and reflected angle is equal to the incident angle (θ).[138] Constructive interference occurs when Bragg's law can be satisfied,[140] i.e., the distance between two incident beams (given

by AB) and the distance between two reflect beams (given by BC) should be equal to a whole number of the wavelength (nλ) (Eq. 2.1).[140]

$$AB + BC = n\lambda. \qquad \text{Eq. 2.1}$$

$$n\lambda = 2d \sin\theta \qquad \text{Eq. 2.2}$$

The extra distance beams have to travel is dependent on the d spacing and the incident angle of the X-ray; therefore, by investigating different angles along the focusing circle, different crystal planes with unique d spacing can be identified. The diffracted intensity is measured as a function of 2θ which results in a diffraction pattern where the intensity of the diffraction peaks is dictated by the amount of constructive interference. Most materials have a characteristic diffraction pattern which allows components in materials to be identified through accesses a database of diffraction patterns.[141]

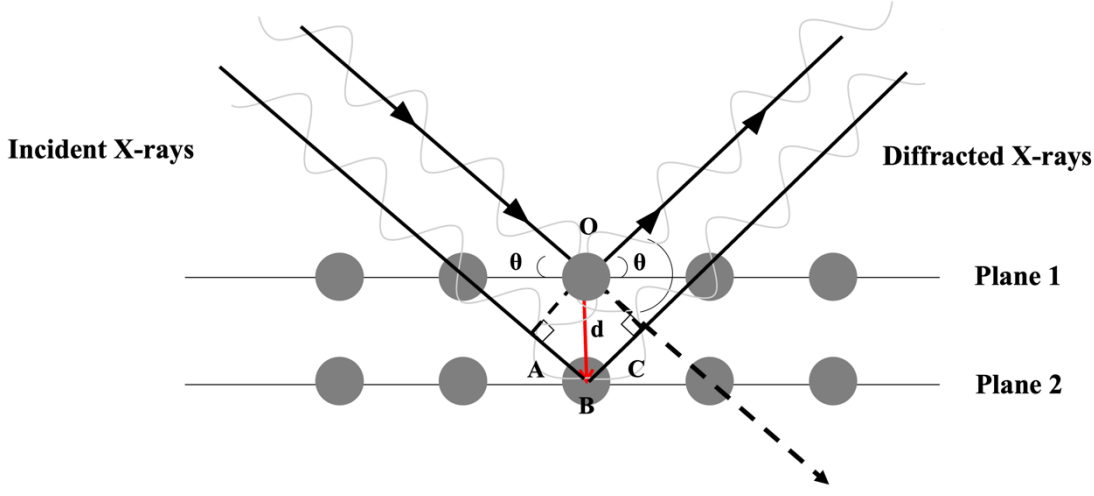

Figure 2.3. A schematic diagram representing Bragg's law. When the distance between AB and BC differs by an integer number of λ, the diffracted X-ray constructively interfere.

Powder XRD measurements in this thesis were performed on a Rigaku Ultima IV X-ray diffractometer with Cu Kα radiation (λ = 1.54 Å) and diffracted beam monochromator, using a step scan mode with the step of 0.05° (2θ) and 3 counts/s per step. The samples were placed on a zero-background Si wafer. Diffraction patterns of anatase TiO_2 powders were compared with reference to International Centre for Diffraction Data (ICDD) database.

2.2. Electron Microscopy

Electron microscopy is a technique used to characterize the morphological and chemical properties of materials.[142] This technique has the ability to image objects at the micro/nano or even down to atomic size.[143] The resolution of electron microscopes is higher than traditional optical microscopes which use visible light radiation.[144] The wavelength of the visible light (400 – 700 nm) limits the resolution of the image.[145] The wavelength of electron beams in electron microscopes is short (10 pm to 10 nm), which can interact with atoms in the system to generate spatial images in high resolution.[146] Electron microscopy can be operated in different modes with two most common ones being scanning electron microscopy (SEM) and transmission electron microscopy (TEM). The operating principle in both types involves the use of an electron beam to capture the material information.[147] **Figure 2.4** illustrates a schematic of the fundamental methodology of SEM and TEM, respectively. SEM examines the surface of the sample by analyzing reflected or knocked-off electrons, but TEM creates 2-D images of the specimens by using the transmitted electrons.[147]

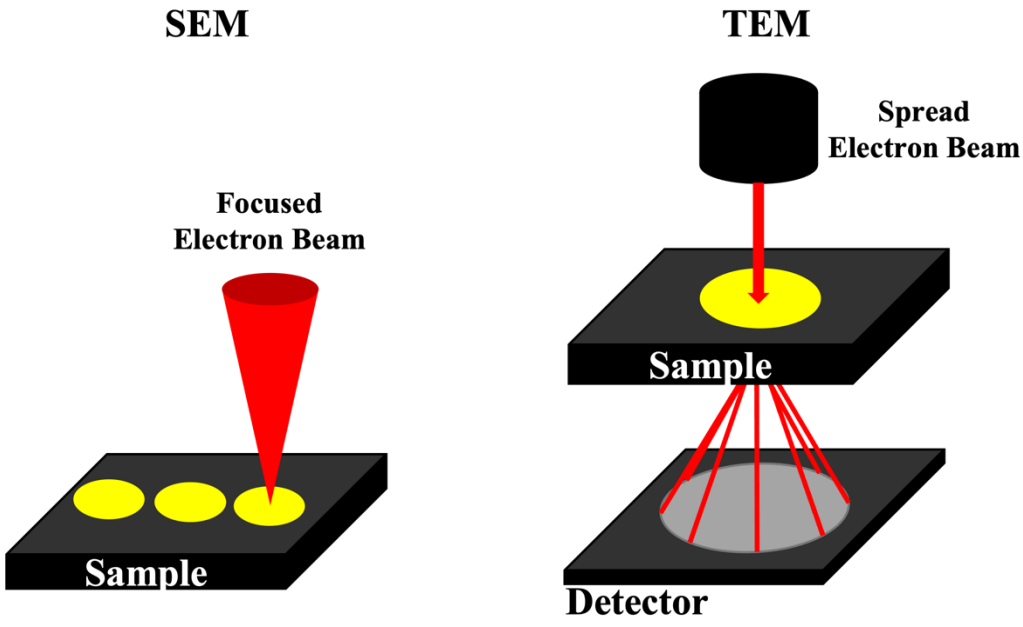

Figure 2.4. A schematic of SEM and TEM instrumental setup.[148]

2.2.1. Scanning Electron Microscopy (SEM)

SEM is a form of electron microscopy and a useful characterization technique that provides information on sample morphology, topography, and differences in chemical composition of the surface.[149] The instrument (**Figure 2.5**) is composed of the electron gun (electron source and anode), a vacuum chamber, a condenser lens, and a selection of detectors.[150] The electron gun at the top of the column produces a source of electrons from a small spot. Common electron sources used are thermionic tungsten, LaB_6 and, hot or cold field emission.[147] The electron beam is passed through the condenser lens and adjusted to a small electron beam for focusing samples.[148] Then, scanning coils deflect the beam in the X and Y axes for faster scanning and cooperate with the objective lens to control the magnification and minification of imaging.[151]

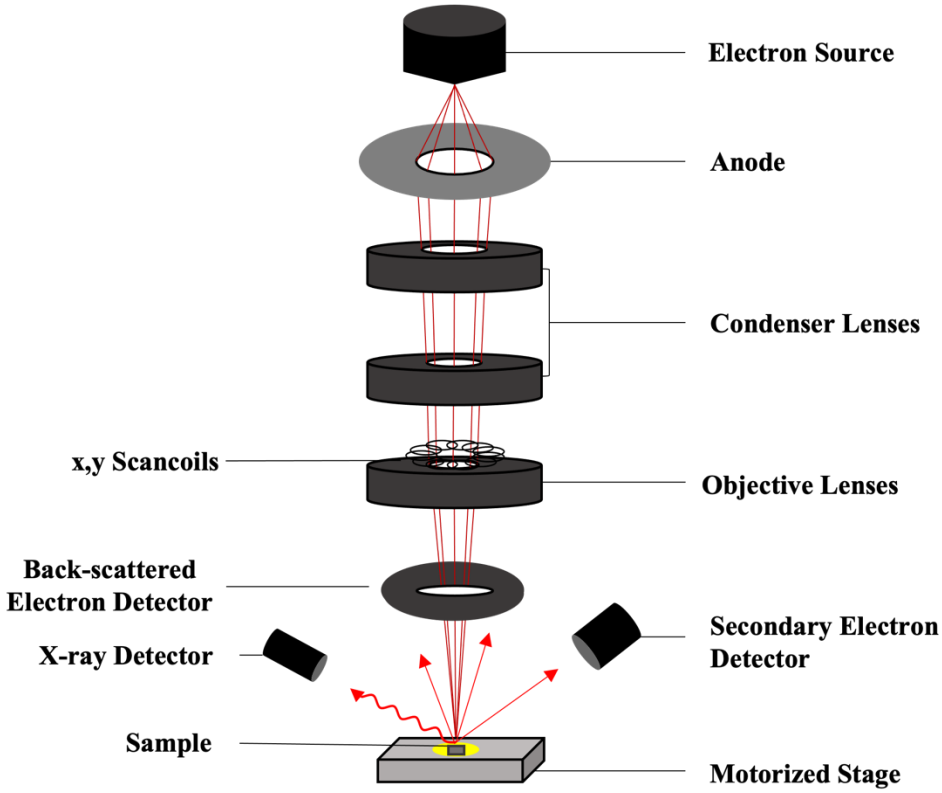

Figure 2.5. The main components of an SEM microscope.[150]

When the electron beam passes the objective lens and interacts with the sample, several processes will occur, as shown in **Figure 2.6**.[152] Secondary electrons (SEs) and backscattered electrons (BSEs) are crucial for image generation.[152] SEs are free electrons that emit from the sample in a vacuum. Because the binding energy is low between nuclear and electrons in the outer shell, the outer electrons are an easy escape from the atoms after acquiring energy from the primary electron beam *via* inelastic collison.[153] The energy of SEs is below 50 eV.[149] The SEs detection is very surface sensitive and is useful in determining topography.[151] On the other hand, BSE are higher energy (over 50 eV) than secondary electrons since they arise from mostly elastic collisions with the nucleus of surface atoms.[154] Compared to SEs, the energy of BSE is much higher and can penetrate

much deeper into the specimen.[152] The higher the atomic number of a material, the more likely that backscattering will occur which allows identification of elemental differences from brightness variation in the resulting image.[150] After scanning sequentially, the signal of reflective electrons and scattered electrons is sent to a computer to produce a three-dimensional image.

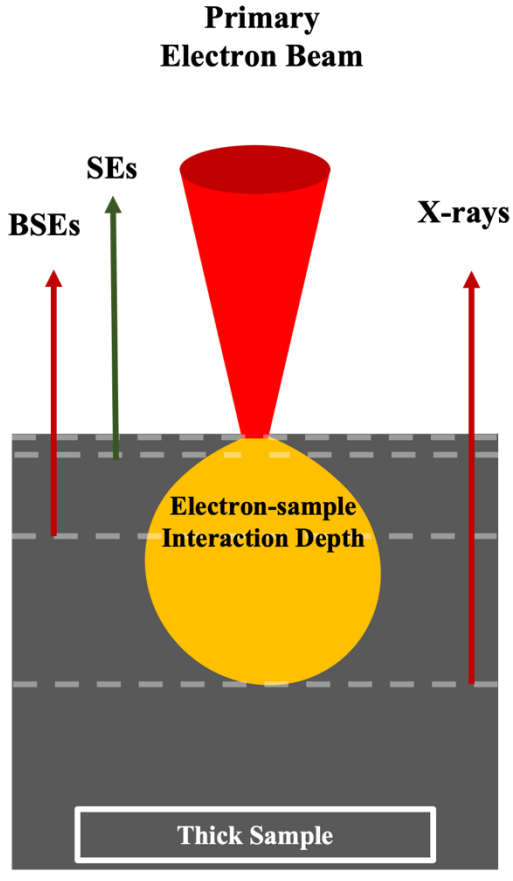

Figure 2.6. The absorbed depth of electrons in the sample.[150,155]

The SEM images of $TiCu_xO_2$ catalysts in this project were collected using a Hitachi S-4700 field-emission scanning electron microscope (FESEM). The $TiCu_xO_2$

catalysts were dispersed in acetone. and drop cast onto a silicon wafer. The images were collected at 3.0 – 5.0 kV accelerating voltage and an emission current of 14 – 16 μA. The SEM images were collected by Sarah Martell and Isabel Curtis at Dalhousie University.

2.2.2. Transmission Electron Microscopy (TEM)

TEM is an electron microscopy technique that is imaged *via* a transmitted electron beam.[150] It is a characterization technique capable of providing information on sample morphology by producing a two-dimensional image as well as information on crystal structure through diffraction.[156] The basic components of TEM are shown in **Figure. 2.7**, and the working principle is very similar to optical microscopy. The electron gun and electromagnetic lenses in TEM are equivalent to the light source and glass lenses in optical microscopy.[150] To collect a TEM image a coherent electron beam of energy ranging from 60 – 150 keV is focused on a thin sample.[148] To do so, the electrons pass through the condenser system to focus the beam and control their diameter. After the generation of a suitable electron beam, the beam transmits the sample for final imaging. The objective lens is located under the sample stage, which is used to form the first image and diffraction pattern. The first image and diffraction pattern are magnified by the projector lens onto the detection system and magnifies the signal of transmitted elections. Then, the image is translated by a charged coupled device (CCD) camera and sent to a computer.

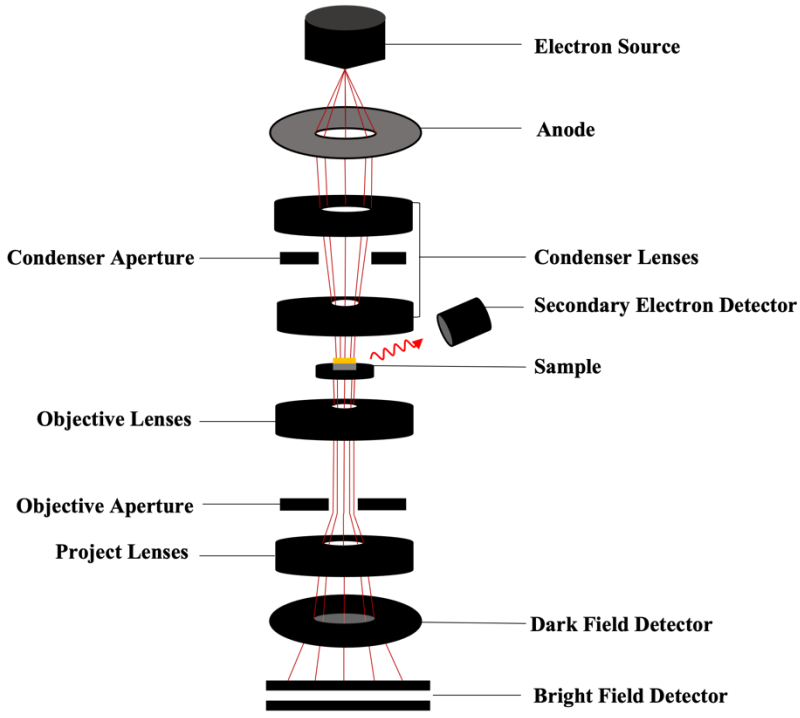

Figure 2.7. The main components on a TEM microscope.[157]

There are three main modes to produce images in TEM, including bright-field imaging, dark-field imaging, and diffraction imaging.[157] Bright-field imaging is a common and straightforward mode. The objective aperture selects the transmitted electrons to form images.[158] If the areas have higher thickness or mass, the electrons are scattered and the transmitted electrons decrease,[158] resulting in an area that is darker.[159] Oppositely, in dark-field imaging, the objective aperture detects the scattered electrons. The area is brighter if more electrons are scattered.[160] The diffraction imaging is caused by the elastic scattering beam and is widely applied in high-resolution transmission electron microscopy (HR-TEM).[161] In HR-TEM, the images of the crystalline structure are created by interference of transmitted and diffracted electron beams.[162] The diffracted electrons interact with the

crystal lattice to reveal the lattice spacing and grain boundaries.[163] The phase crystalline images can be created by HR-TEM when the samples are ultrathin (thickness < 100 nm).[158]

Furthermore, some TEM equipment is equipped with scan coils, which can scan a focused electron beam to scan across the specimens for sequential chemical analysis of the across areas of the specimen.[158] The equipment is called scanning TEM (STEM). Importantly, STEM with extra lenses can correct the spherical aberration and obtain more focused spots.[158] Under this condition, the resolution of the dark-field mode is improved to a high-angle annular dark field (HAADF), which makes it an ideal instrument for analyzing chemistry at the atomic scale.[158]

$TiCu_xO_2$ catalysts in this thesis were analyzed using a Hitachi HT7700 TEM at an operating voltage of 80 to 120 kV. The instrument equips a dual-focus objective, which is useful for swapping between high contrast and high-resolution mode. A CCD camera transforms the signal of electrons into an image. The samples were dispersed in ethanol and sonicated for 20 min. The dispersion was then dropcast onto a carbon coated Ni TEM grid for analysis. TEM images were collected by Judy Maclnnis at Cape Breton university. The images of HAADF in SEM mode was performed with a Thermo Fisher Scientific Talos 200X at an operating voltage of 200 kV with a spot size of < 1nm, and the convergence semi-angle 10.5 mrad. The images were collected by Andrei Carmen at McMaster University.

2.3. X-ray Photoelectron Spectroscopy

X-ray photoelectron spectroscopy (XPS) is a surface-sensitive analysis technique based on the photoelectric effect.[164] When incident X-rays irradiate a material,

the atoms near the surface of the sample absorb these photons and can eject core electrons from the material.[165] Analyzing the kinetic energy of the ejected photoelectron can reveal chemical state information, atomic chemical environment, and elemental composition of the material.[166]

Figure. 2.8 illustrates a schematic diagram of an XPS instrument.[167] The main components are an X-ray source, the sample stage, an electron transfer lens, an analyzer, and a detector.[164] The X-rays are generated using sources such as Al Kα ($h\nu$ = 1486.6 eV) and Mg Kα ($h\nu$ = 1253.6 eV) similar to the process explained in X-ray diffraction technique.[167] After the X-rays irradiate the sample, the ejected electrons collect onto the lens system for signal magnification.[168] Then, electrons with specific energy pass through the concentric hemispherical analyzer to obtain a measurable current pulse.[169] The XPS analysis is performed within an ultrahigh vacuum (UHV) chamber to avoid the photoelectrons colliding with nearby molecules and contaminants.[170]

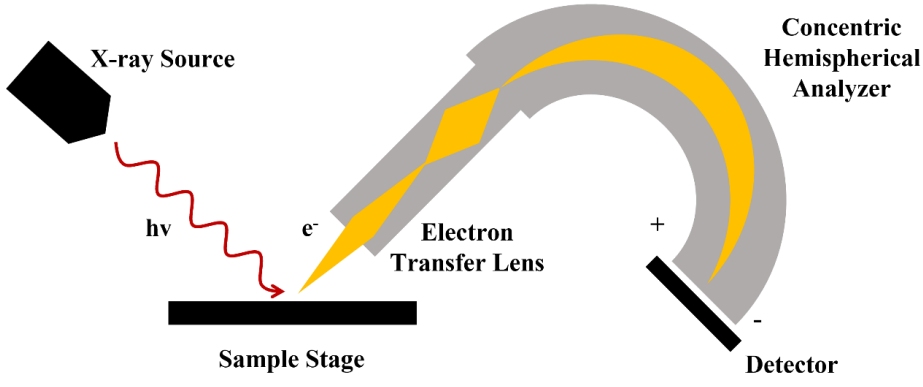

Figure 2.8. The schematic diagram of an XPS instrument.[171]

When primary X-rays interact with the sample, the X-ray energy transfers to a core level electron. If the photon energy is higher than the binding energy, which is the energy difference between the Fermi and the core energy levels, the core electrons are ejected from the atom.[171] The ejection process of a fluorine atom is shown in **Figure 2.9**. The kinetic energy of the electrons can be measured by the XPS instrument.

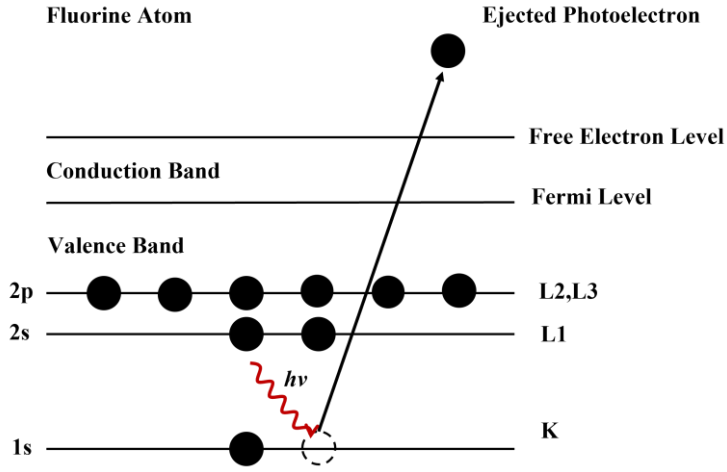

Figure 2.9. An example of the ejection process to generate a photoelectron.

The binding energy (BE) is equal to photon energy minus kinetic energy (E_k), as shown in Eq. 2.3.[172] However, the measured energy will shift due to X-ray bombardment within the spectrometer. The work function, Φ_{sp}, of the spectrometer is independent of electron binding energy and needs to be corrected by a defined peak to know the binding energy value, e.g., carbon 1s to 285.0 eV.[170] Finally, according to the conservation of energy required; the equation is shown in Eq. 2.4.[170]

$$BE = h\nu - E_k \qquad \text{Eq. 2.3}$$

$$BE = h\nu - \Phi_{sp} - E_k \qquad \text{Eq. 2.4}$$

XPS is a technique that can be used for both qualitative and quantitative analysis. Qualitatively, XPS spectra easily determines the elements present by observing major peaks.[172] The observed peaks are unique, which shows the binding energy level of emitted electrons in the sample.[172] Because the electron mean free path for the excited photoelectrons is below 3 nm, observed elements in the XPS spectra are located in the outermost 20 atomic layers in the sample.[173] Besides H and He, all elements can be identified with a reference book or computer database which contains energies for each expected element peak, peak shape, peak splitting, and chemical element shifts.[174] For quantitative analysis, determination of the relative concentrations of the different constituents is important, which can be estimated by peak area and peak height sensitivity factors.[175]

In this thesis, the XPS spectra of $TiCu_xO_2$ catalysts were collected by Andy George using a Thermo VG Scientific Multilab 2000 spectrometer. K_α X-rays of aluminum were used in this XPS system. High-resolution spectra were recorded with a pass energy of 30 eV and a step size of 0.1 eV. The spectra were fitted by CasaXPS software. The background used a nonlinear type (Shirley mode), and a Gaussian-Lorentzian line shape of GL (30). The binding energy of C1s (284.8 eV) was used for calibration.

2.4. Ultraviolet-visible Spectroscopy

Ultraviolet-visible (UV-vis) spectroscopy is a technique that quantifies light absorption of samples as a function of wavelength.[176] The instrument is mainly composed of a white light source, collimator, monochromator, sample holder, and detector.[177] The schematic diagram of the UV-vis spectrometer is presented in **Figure 2.10**.[177] The radiation

source with a given wavelength range (190 nm to 2300 nm) passes through a collimator to obtain a straight and parallel beam.[178] The collimated beam is split and selected into differentiated wavelengths or colours *via* a monochromator to irradiate the sample.[179] The light-transmitted intensity is measured by the detector.

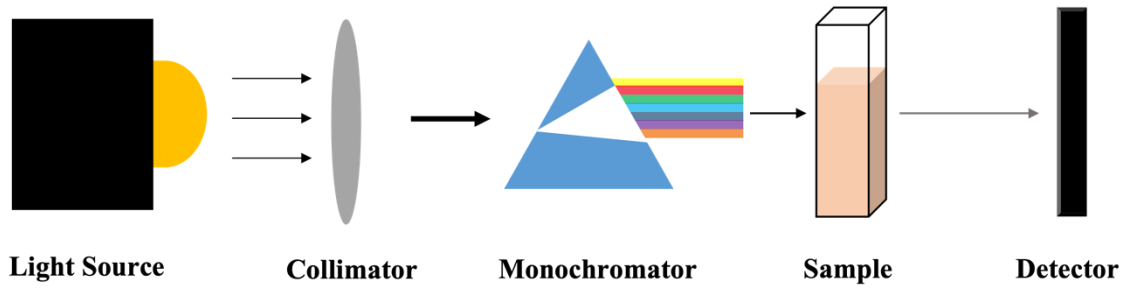

Figure 2.10. The main components of UV-vis spectrometer.

The absorbance (A) of the samples is related to transmittance (T) as given by Beer-Lambert's Law (Eq. 2.5). Beer-Lambert's law is useful for determining the concentration of the sample. Eq. 2.6 shows the absorbance directly proportional to the concentration of the absorbing sample and the path length of cuvettes.

$$A = -\log T = -\log I/I_0 \qquad \text{Eq. 2.5}$$

where I and I_0 are the intensities of the transmitted and incident light beams, respectively.

$$A = \varepsilon bc \qquad \text{Eq. 2.6}$$

where ε is the molar absorptivity (a constant, L mol^{-1} cm^{-1}), b is the path length, c is the concentration of the sample solution.

2.4.1. Diffuse Reflectance Spectroscopy

Diffuse reflection spectroscopy (DRS) is a subset of absorption spectroscopy.[178] The Bouguer-Lambert-Beer law describes the light absorbance of the sample that is not consumed by scattering and reflection processes.[180] In liquid dispersed systems, the light scattering losses are minimal because the particles are so tiny. However, the reflection losses at every phase boundary are excluded in practice by measuring versus a reference cuvette.[180] However, in the case of solid samples that scatter strongly or are not transparent the incident light is reflected diffusely, as shown in **Figure 2.11**.[181]

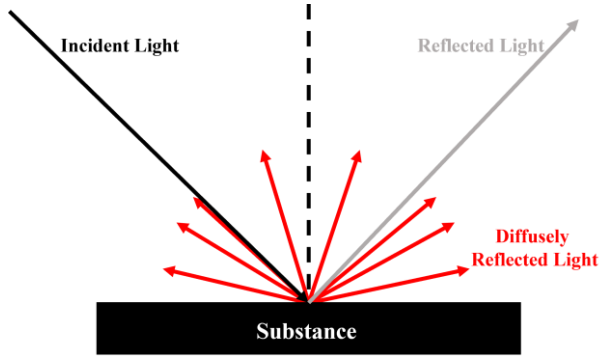

Figure 2.11. A schematic of reflected and diffused reflected light.

The reflecting signal is a function of the absorbing power of a substance, i.e., its color.[180] The complementary color to that observed by the eye is absorbed by the substance.[182] Surface scattering causes diffuse reflection that can be measured by diffuse reflectance spectroscopy, represented by Kubelka-Munk function $F(R_\infty)$, as shown in Eq. 2.7.[68]

$$F(R_\infty) = [(1- R_\infty)^2] / (2R_\infty) = k/s \quad \text{Eq. 2.7}$$

where R_∞ is Kubelka-Munk function that implies the thickness of substances approaches infinity within the scope of the theory. k is absorption coefficients and s is scattering coefficients.

In practice, the real intensity of diffusely reflected light form a substance must consider the impact of the background reflectance.[183] If the background has reflecting power equal to the substance, the observed spectrum does not include any properties of the substances. Deposited MgO and $BaSO_4$ are the best standards because of their easy obtainment under defined conditions.[184]

Diffusion reflectance spectra are obtained by a spectrometer. The whole system includes a broadband (either in UV, visible or near-infrared) light source, a PC-driven miniaturized spectrometer, and diffusion reflectance fiber probe, as shown in **Figure 2.12**.[182]

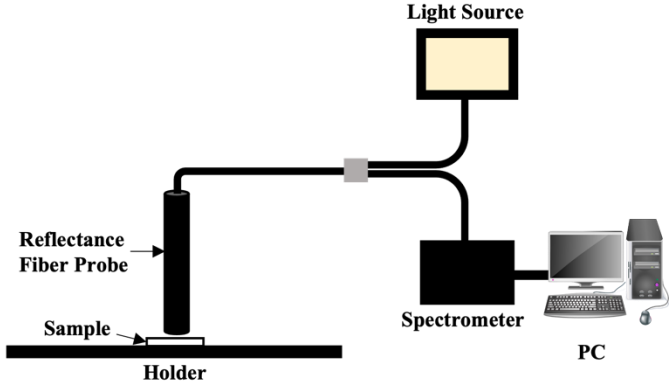

Figure 2.12. A schematic of a diffuse reflectance spectrometer.

Band Gap Calculation

The absorption properties of solid samples can be characterized by a diffuse reflectance spectrometer. The band gap can be calculated through analysis of the absorption edge.[180] The threshold of continuous optical absorption is represented by the quantum mechanical perturbation theory of electron-photon interaction.[185] For different interactions, along the sharp absorption edge, the energy of incident photons, and band gap of a semiconductor can be shown through Tauc plot, Eq. 2.8.[68]

$$(\alpha h\nu)^{n} = A(h\nu - E_g)^n \qquad \text{Eq. 2.8}$$

where E_g is the band gap (eV), h is the Planck's constant (J s), A is the absorption constant, ν is the light frequency (s^{-1}), and α is the absorption coefficient. The n-value depends on the interband transition mechanism. If the semiconductor has indirect band gap, n = ½; conversely, if the semiconductor has direct band gap, n = 2.[185]

In this thesis, the absorbance spectra of all $TiCu_xO_2$ catalysts were recorded with a UV/VIS/NIR spectrometer (SILVER-Nova, Lambda LS 30 with a homemade sample holder). The band gaps of the TiO_2-based materials were estimated from Tauc plots obtained from the absorbance spectra.

2.4.2. Microplate Reader

A microplate reader is a multimodal instrument that performs a variety of optical experiments, including absorbance, fluorescence, and luminescence measurements. In this thesis, the absorbance measurements are the primary mode to use; its principle is the same as the UV-vis spectrometer. Microplate reader experiments are performed in a microplate,

which is a transparent plastic plate composed of multiple wells. **Figure 2.13** shows the setup of a microplate. Microplate reader measurements are in seconds and can measure multiple samples simultaneously. Different from a traditional UV-vis spectrometer, the path of light is vertical through the well plates, then reaches the detector. The path length is determined by the volume of samples, so the volume in one experimental system should be consistent. In this thesis, the sample was collected into 96-well Corning UV-Plate, then the absorbance of RhB and the turbidity of *Escherichia coli (E. coli)* were measured by a BMG LABTECH Omega Microplate Reader.

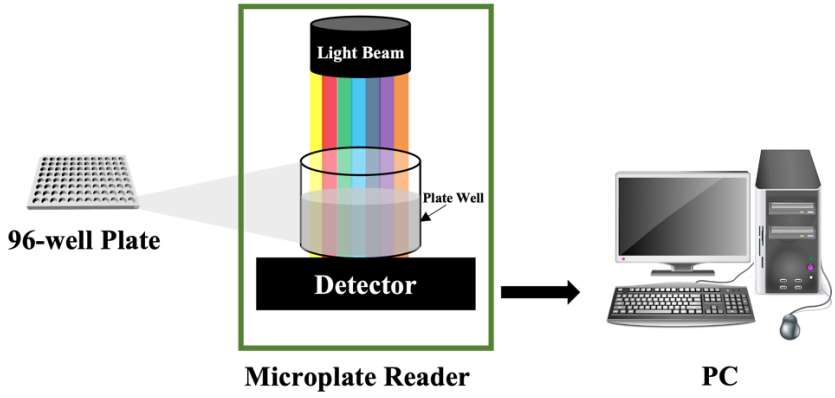

Figure 2.13. The schematic diagram of the microplate reader in absorbance mode.

CHAPTER 3. Synthesis of Copper-doped White and Black Titanium Dioxide Nanoparticles

3.1. Introduction

The morphology and structure of TiO_2 affect its light absorption, charge recombination and separation, chemical adsorption, ROS generation, and photocatalytic activity.[186] Recently, many studies have focused on developing synthetic methods to tailor desired structures.[62,75,187,188] Some approaches include sol-gel, micro-emulsions, precipitation, flame synthesis, solvothermal/hydrothermal, etc.[186] The sol-gel and solvothermal methods are the most commonly used.[189] However, there are disadvantages to the sol-gel method, including a fast hydrolysis rate, soft/hard template requirement, unstable substrate attachment, and non-uniform particle-size distribution, which limits TiO_2 modification.[189]

3.1.1. Solvothermal Method

Nanomaterials prepared using the solvothermal method are expected to have a larger surface area, smaller particle size, and greater stability than those obtained by sol-gel methods. The solvothermal method is a process in which the chemical reaction occurs in a solvent at a temperature above its boiling point.[190] When water is used as the solvent, the method is referred to as hydrothermal synthesis.[189] The reaction temperature and pressure typically range between 100 – 250 °C and 0.3 – 4.0 MPa, respectively.[191] This method is used when the required solubility cannot be reached in the solvent and/or when the reaction temperature below the boiling point of solvent is not sufficient to decompose the precursors.[192] The solvothermal method can be used for controlling the particle size,

morphology, and surface area by modifying variables such as pH, temperature, pressure, reaction time, solvent, etc.[191,193,194]

During the solvothermal process, the decomposition of the organic solvents or the reaction precursors can produce water in-situ that can participate in the hydrolysis reactions. This helps control the rate of hydrolysis compared to performing the reaction in water as the solvent. The metal precursors are usually alkoxides.[193] The organic media consists of solvent, oxidants or reductants, and structural templates.[189] In 1999, Kominami *et al*., reported a type of solvothermal processing under autoclave conditions to synthesize microcrystalline TiO_2 powders with sizes up to 10 nm in diameter.[195] In the synthesis, Ti^{4+} alkoxide precursors were hydrolyzed using water that was liberated homogeneously from alcohol condensation reaction.[195] Because TiO_2 has low solubility in organic solvents, the alcoholysis process helps form agglomerates resulting in nano-sized particles.[196] However, in this case, the TiO_2 precursors will graft plenty of hydroxyl groups from the alcohol, resulting in amorphous material.[197] The obtained TiO_2 precursors need to be calcinated for removing the organic template and forming crystalline phases.[194]

The most common Ti precursor and alcohol are Ti isopropoxide (TTIP) and isopropanol for anatase phase TiO_2 formation. The transformation from TTIP to TiO_2 NPs undergo three main reactions: alcoholysis (Eq. 3.1), hydrolysis (Eq. 3.2 and Eq. 3.3) of TTIP, and condensation (Eq. 3.4 and Eq. 3.5), which are the same as most solvothermal alcoholysis synthesis.[194]

Alcoholysis step:

$$2R–OH \rightarrow R–O–R + H_2O \qquad \text{Eq. 3.1}$$

Hydrolysis step:

$$Ti(OR)_4 + H_2O \rightarrow Ti(OR)_2(OH)_2 + ROH \quad \text{Eq. 3.2}$$

$$Ti(OR)_2(OH)_2 + H_2O \rightarrow Ti(OR)(OH)_3 + ROH \quad \text{Eq. 3.3}$$

Condensation steps:

$$Ti(OR)_2(OH)_2 \rightarrow TiO_2 + 2ROH \quad \text{Eq. 3.4}$$

$$Ti(OR)(OH)_3 \rightarrow TiO_2 + H_2O + ROH \quad \text{Eq. 3.5}$$

where R is C_3H_7.

In research on TTIP decomposition, some authors showed that the presence of isopropanol facilitates precursor transformation into metal oxide.[194] Takahashi *et al*. figured out that pure alkoxide was difficult to obtain from TTIP decomposition.[198] The water formation was happened after the dehydration of isopropanol then initiated the hydrolysis reaction of the TTIP. Thus, the first step in TiO_2 formation from Ti alkoxide was alcohol dehydration followed by hydrolysis reactions.

3.1.2. $NaBH_4$ Treatment

Hydrogenation treatment is a type of band engineering method to enhance the visible light absorption of TiO_2.[199] This treatment is usually carried out by a high temperature treatment under reducing atmosphere (i.e., pure H_2 and H_2/Argon).[200] Mao *et al*. first proposed the hydrogenation method in 2011.[103] Ti^{4+} in original TiO_2 crystals was reduced to Ti^{3+} under a H atmosphere which produced a disordered nanophase.[199] At the same time, H dopant was incorporated on the surface of TiO_2 inducing the generation of

surface defects such as OVs and Ti^{3+} defects.[106] This $bTiO_2$ had a narrow band gap (~1.54 eV) demonstrated high photocatalytic activities to degrade organic pollutants and water splitting.[100] However, this synthesis approach for generating new material was time consuming, which required heating in H_2 atmosphere for five days.[103] The mechanism for the formation of disordered surfaces was not understood. So, during the long annealing time, the crystalline size and photocatalytic activity were hard to control, limiting large-scale production for industrial applications.[202] In 2014, Sun *et al*. developed a new approach to the synthesis of $bTiO_2$ through thermal decomposition of $NaBH_4$, which was facile and easy to control.[115] They also proposed an explanation for the formation of disordered layers, enhancement of photocatalytic performance, appearance, and change of band energy.[115]

$NaBH_4$ has a high volumetric and gravimetric H capacity (115 kg of H_2 m^{-3}; 10.7 mass %),[203] and it can be released in controllable amount, i.e., the H_2 released amounts depend on experimental conditions, such as the reaction time, temperature, pressure, and heating rate.[204–206] Mixing $NaBH_4$ with TiO_2 can also improve the homogeneity of hydrogenation once H_2 is produced in-situ. During the thermal reaction, H_2 released from $NaBH_4$ can react with TiO_2 and give the photocatalyst a higher visible-light absorption capacity. The thermal decomposition follows the reaction (Eq. 3.6).[204]

$$NaBH_4 \rightarrow \sum(i)\ \text{solid (Na, B, H)} + \sum \text{gas (j) (B, H) isothermal} \qquad \text{Eq. 3.6}$$

where i is isothermal, j is exothermic.

During thermal hydrogenation reaction, two types of defects can be formed in TiO_2: surface defects and bulk defects.[115,207] The surface defects that occur on the surface

can trap electrons or holes to inhibit charge recombination and improve photocatalytic activity.[117] However, the bulk defects can easily trap the charge carriers in the interior of the particle and decrease the photocatalytic activity by preventing their participation in redox reactions.[102] Increasing the amount of surface defects is the key point to maintaining the high photocatalytic efficiency, which can be controlled by the treatment temperature.[115] It has been shown that 300 °C was the best reaction temperature for generating a specific concentration of surface defects.[117,208–212] The decomposition of $NaBH_4$ is an exothermic process; therefore, the calcination temperature must be kept low to protect the original morphology of TiO_2. Morphology and surface defects will be altered at a high treatment temperature, impacting the photocatalytic activity.[115,117] The sorption capacity of $NaBH_4$ is high, the solid residuals absorb on the TiO_2 lattice and need to be treated with hydrochloric acid (HCl).[210]

In this thesis, Cu-doped white and black TiO_2 catalysts were synthesized *via* the solvothermal method and $NaBH_4$ treatment for photocatalysis and disinfection applications.

3.2. Experimental Methods

3.2.1. Materials

Titanium isopropoxide (TTIP, 97%), cupric acetate hydrate ($Cu(OAc)_2$, 98%) sodium borohydride ($NaBH_4$, 99%) were purchased from Sigma-Aldrich. Isopropanol (99%), ethanol (90%), and hydrochloric acid (HCl, 37%) were purchased from Fisher Scientific. All reagents were of analytical grade and were used as received without further

purification. Nano-pure water was obtained from a Thermo Scientific Barnstead Ultrapure Water Purification System.

3.2.2. Synthesis of Cu-doped White TiO_2

$wTiCu_xO_2$ and undoped $wTiO_2$ NPs were prepared by the solvothermal method. 8.60 g of titanium isopropoxide (TTIP) as Ti precursor was dispersed into 20 mL of isopropanol. 54.44, 5.44, 0.544, 0.0544 mg of cupric acetate hydrate ($Cu(OAc)_2$) was separately dispersed in 9.5 mL isopropanol alcohol by stirring for 1 h at 400 rpm at room temperature. Then, required amounts of $Cu(OAc)_2$ solution (1 ppm, 100 ppm, 1000 ppm, and 10,000 ppm with respect to the final solution) were added to the TTIP solution with stirring for 1 h at 400 rpm. The ratio of parts per million (ppm) was described as the relative abundance of dissolved $Cu(OAc)_2$ in the total volume of final solutions. For example, 1 ppm Cu-doped white TiO_2 corresponded to 0.001 mg Cu solution in a 1 mL final solution. The ratio of Cu and the final solution volumes was kept constant. Then, the mixtures were sonicated for 1 h. During sonication, a small amount of nano-pure (0.5 mL) water was added to the mixtures. The final reaction volume was adjusted to 30 mL by adding additional isopropyl alcohol. The solution was then transferred into an autoclave lined with a Teflon vessel and kept at 185 °C for 24 h. After cooling, the precipitate from the reaction was rinsed with ethanol and distilled water for 3–4 times to remove unreacted residuals. Following the washing, the white powder was collected by centrifuging at 4700 rpm for 30 min and dried in an oven at 100 °C. This yields amorphous $wTiCu_xO_2$ NPs and to obtain crystalline product, the amorphous white powder was calcined at 500 °C in a muffle furnace at a ramp rate of 10 °C/min for 3 h.

3.2.3. Synthesis of Cu-doped Black TiO_2

$bTiCu_xO_2$ and undoped $bTiO_2$ NPs in this thesis were synthesized *via* $NaBH_4$ treatment of $wTiCu_xO_2$ and undoped $wTiO_2$ precursors. The reaction was performed using a programmable single-zone tube furnace under Argon flow, as shown in **Figure. 3.1**.

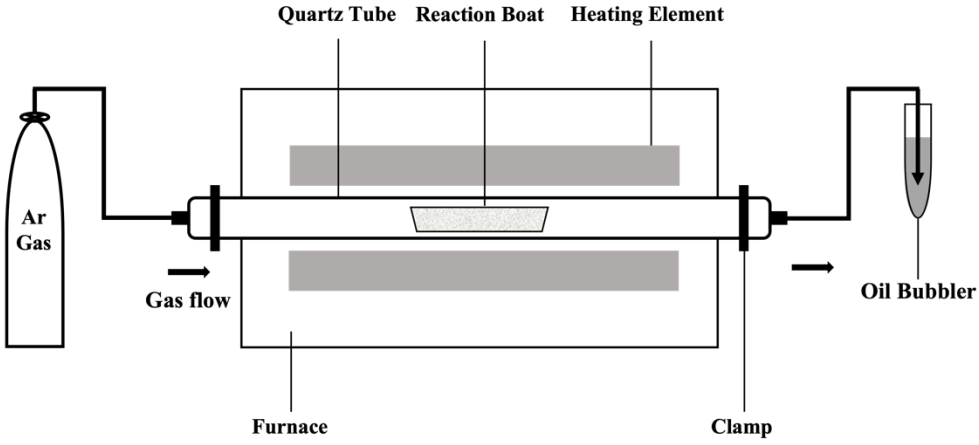

Figure 3.1. Tube furnace set up for $NaBH_4$ reduction reactions.

The reagents (1.00 g TiO_2 precursor and 0.375 g $NaBH_4$ solid powder) were thoroughly ground for 5 min in a mortar and pestle to obtain a homogenous mixture. Then, the mixture was transferred into an alumina reaction boat and was placed in a quartz furnace tube to withstand high temperature (300 °C). The ramp rate was 5 °C min^{-1} and was then held at the 300 °C for 60 min. After cooling to room temperature, $bTiO_2$ was obtained. The reaction product was treated with 1.0 M HCl for 6 h with stirring at 400 rpm to remove unreacted $NaBH_4$ and decomposition salts. The final product was collected by suction filtration and washed with 500 mL of distilled water, then dried overnight in an oven at 100 °C. **Figure 3.2** illustrates the process of $bTiCu_xO_2$ NPs formation.

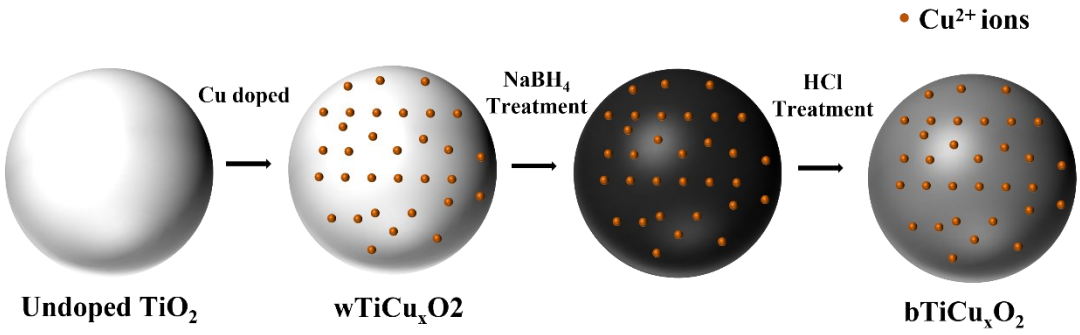

Figure 3.2. The process of $NaBH_4$ reduction to produce $bTiCu_xO_2$ NPs.

3.2.4. Materials Characterization

Powder XRD, SEM, TEM, HRTEM, XPS, and UV-vis analyses were performed on the reaction products as discussed in Chapter 2. Particle size analysis was performed on TEM images using the Image J software.

3.3. Results and Discussion

The powder XRD patterns of the undoped and $TiCu_xO_2$ NPs before annealing is shown in **Figure 3.3**. It can be found that most of the diffraction peaks of the NPs are ascribed to the anatase phase.

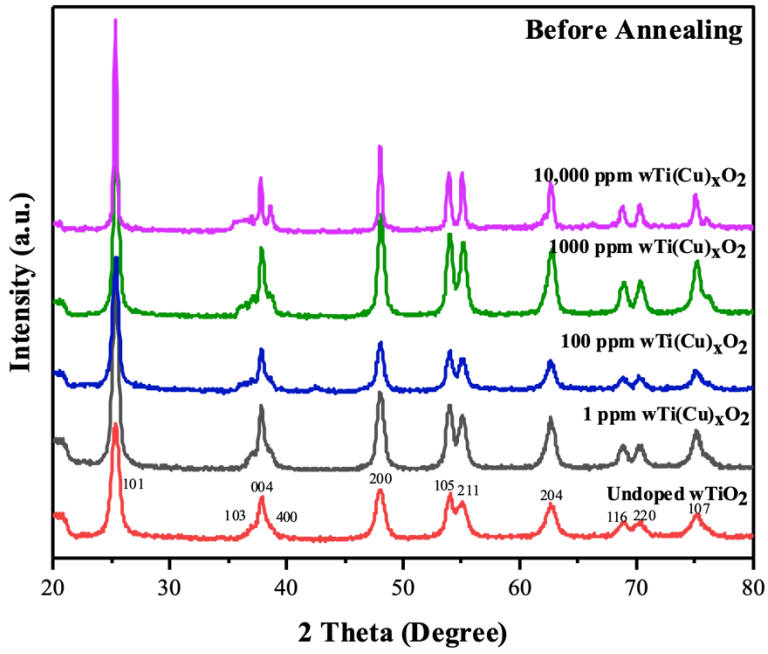

Figure 3.3. Powder XRD patterns of undoped $wTiO_2$ and $wTiCu_xO_2$ catalysts before annealing.

After annealing at 500 °C for 3 h, the anatase peaks is more obvious, as shown in **Figure 3.4**. The diffraction peaks located at 25.3°, 37.1°, 37.85°, 38.8°, 48.1°, 54.1°, 55.2°, 62.8°,69.3°, 70.4°, and 75.3° correspond to (101), (103), (004), (112), (200), (105), (211), (204), (215), (220), and (215) crystal planes, respectively. All the peaks are related to the anatase phase (JCPDS 21-1272) of TiO_2. Metallic Cu or Cu-compound phases were not observed in the XRD patterns, which indicates that the Cu ions were uniformly distributed within the NPs. At the concentrations investigated, incorporation of Cu did not significantly alter TiO_2 crystal structure as no shifts were observed in the diffraction peaks.

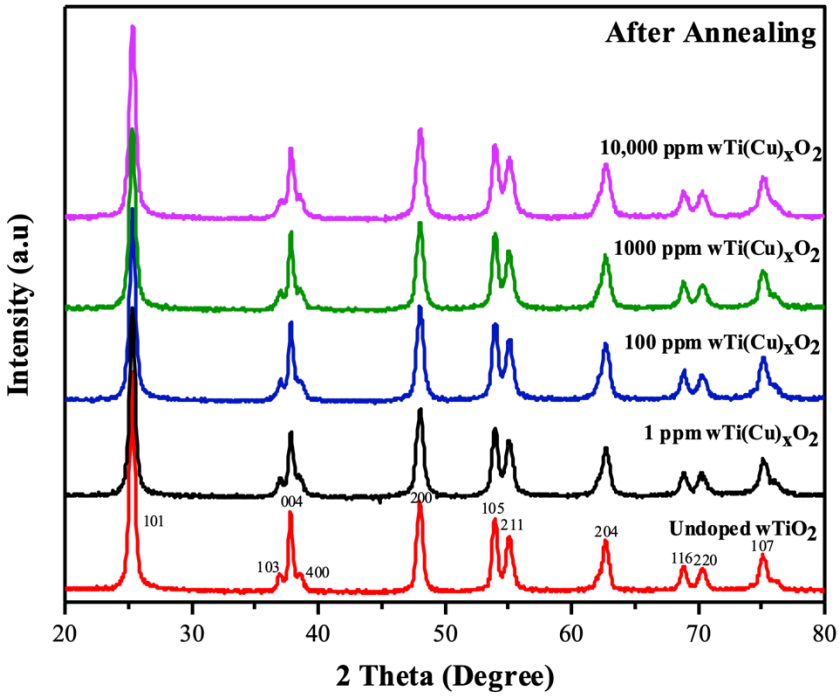

Figure 3.4. Powder XRD patterns of undoped $bTiO_2$ and $wTiCu_xO_2$ catalysts after annealing.

Hydrogenation also did not result in significant structural changes as the patterns remained identical to $wTiO_2$ in the powder XRD analysis (**Figure.3.5**).

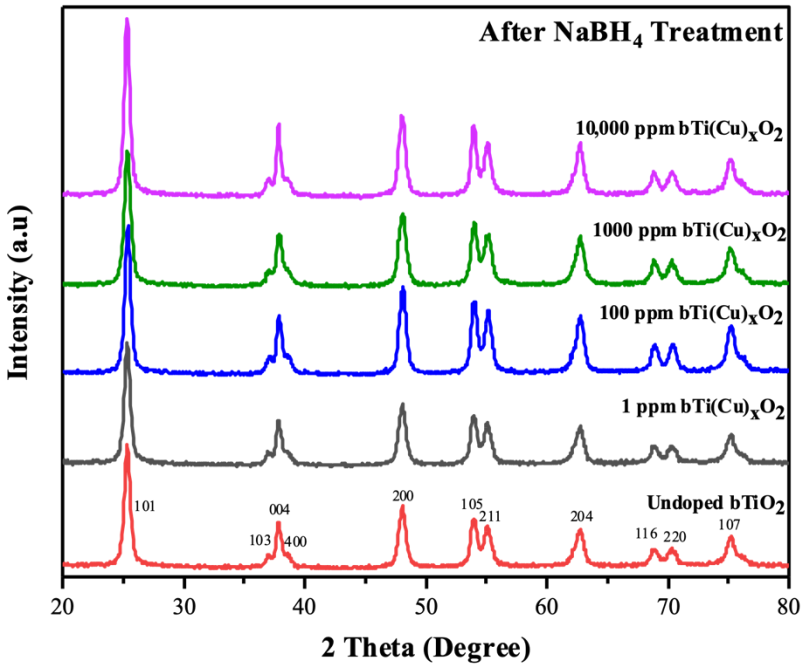

Figure 3.5. Powder XRD patterns of undoped $bTiO_2$ and $bTiCu_xO_2$ catalysts after $NaBH_4$ treatment.

The SEM images of undoped TiO_2 and $TiCu_xO_2$ NPs are shown in **Figure 3.6**. The resolution of the SEM was not high enough to determine the size of the NPs but were found to be aggregated and roughly spherical in shape. Significant charging was also observed likely due to low conductivity of TiO_2 samples which caused further blurriness in the images.

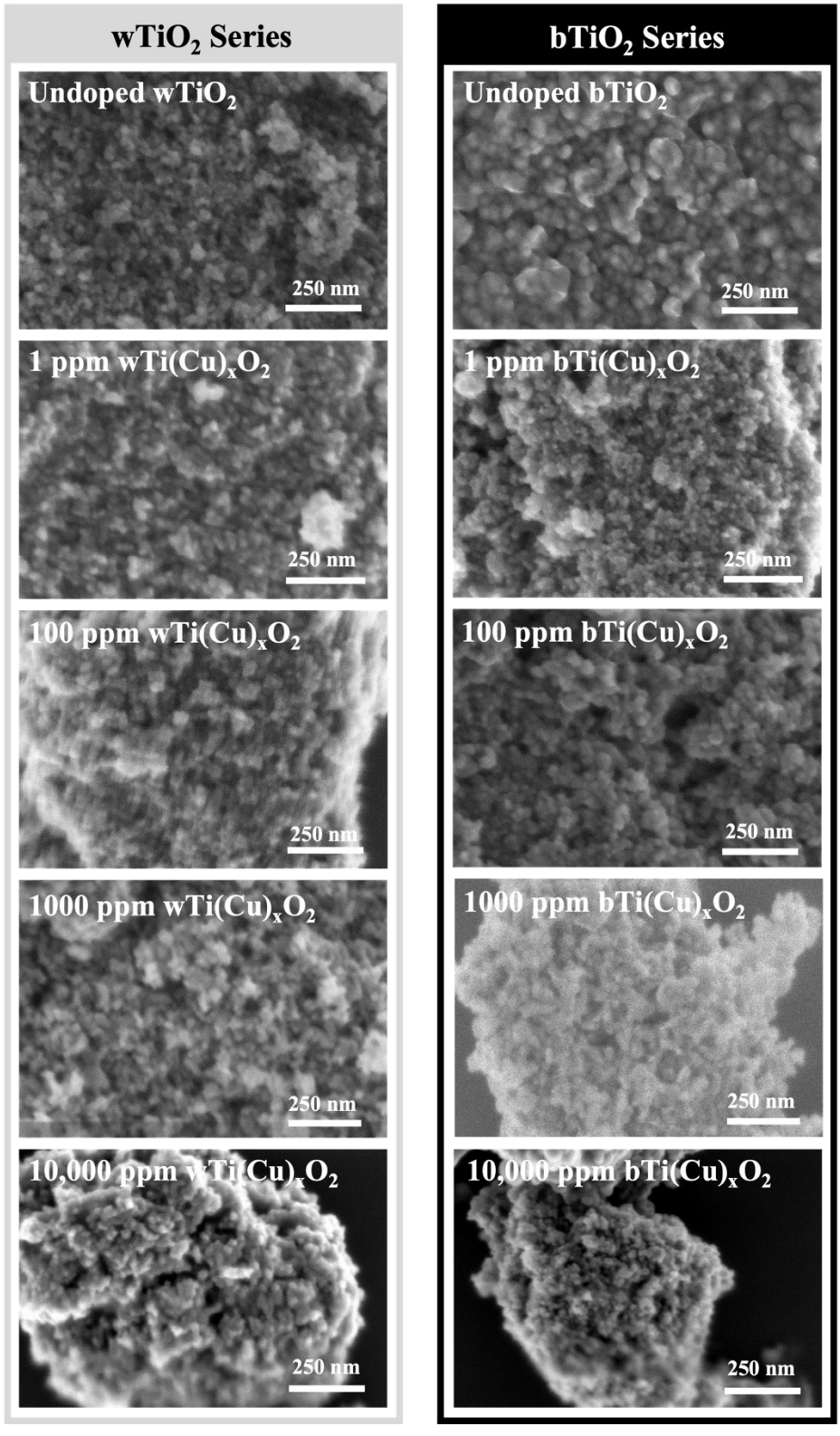

Figure 3.6. SEM images of undoped TiO_2 and $TiCu_xO_2$ samples.

TEM analysis was performed to further understand the morphology and size of TiO_2 NPs. The TEM image of $wTiO_2$ and $wTiCu_xO_2$ NPs revealed aggregates of polyhedron particles, as shown in **Figure 3.7**. The distribution of particle size was obtained by measuring the individual diameters of ~100 particles from the representative TEM images. The undoped $wTiO_2$ NPs had an average size of 18 nm. The average size for $wTiCu_xO_2$ NPs at 1 and 100 ppm where similar to undoped TiO_2 NPs but increased to 27 and 34 nm at Cu concentrations of 1000 and 10,000 ppm, respectively. The polydispersity index of the NPs that shows their size distribution increased from 0.038 to 0.072 nm with increasing Cu concentration. A slight increase in the average particle size was observed after the conversion of $wTiO_2$ to $bTiO_2$ as shown in **Figure 3.8**. The particles were also found be more elongated in shape. The undoped $bTiO_2$ and particles with 1 and 100 ppm Cu had an average size of 20 nm. The particles with 1000 and 10,000 ppm Cu had an average size of 30 and 39 nm, respectively. The increase in particle size is likely due to high temperature used in $bTiO_2$ synthesis that can lead to sintering.

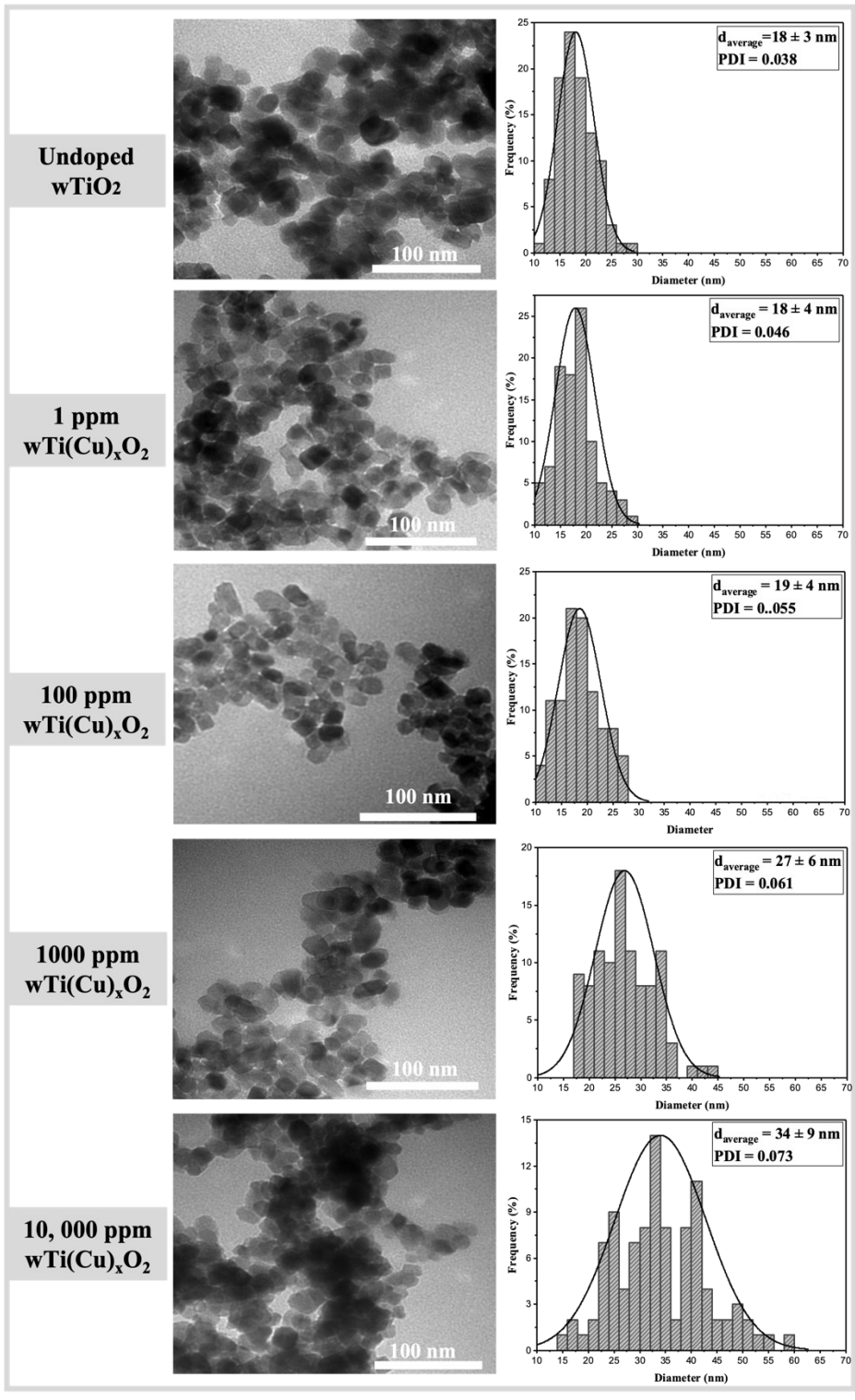

Figure 3.7. The TEM images and particle size distribution of undoped $wTiO_2$ and $wTiCu_xO_2$ NPs.

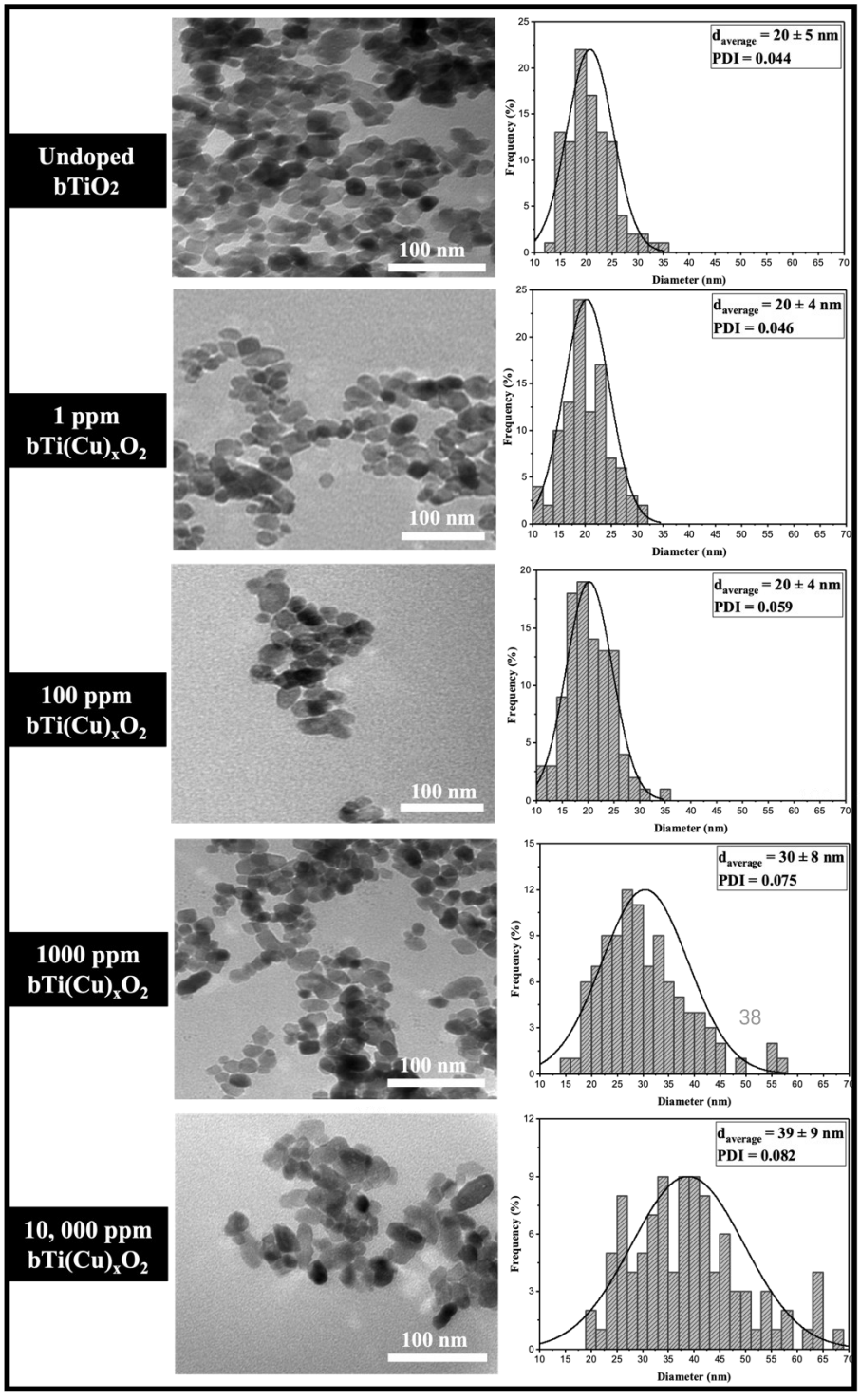

Figure 3.8. The TEM images and particle size distribution of undoped $bTiO_2$ and $bTiCu_xO_2$ NPs.

In order to understand the Cu distribution information of the samples (100 and 10,000 ppm $wTiCu_xO_2$ and $bTiCu_xO_2$), HAADF in STEM mode with the corresponding elemental mapping has been employed. The particles were dropcast onto a Ni grid to avoid contamination from Cu grid typically used in electron microscopy experiments. At 100 ppm Cu-doping, a uniform distribution of Cu was observed in both $wTiO_2$ and $bTiO_2$ indicating that Cu atoms are homogenously incorporated within the TiO_2 crystal structure. At 10,000 ppm, clusters of Cu regions throughout the particles were observed in $wTiO_2$. These clusters grew to create heterogeneously distributed 1– 4 nm CuO NPs within $bTiO_2$ sample. This indicates that with increasing concentration of Cu, the distribution becomes heterogeneous possibly forming CuO grains.[213] After the high temperature treatment for $bTiO_2$ formation, these domains grow to form nanoscale CuO grains. Based on the powder XRD results, these Cu regions are amorphous as no crystalline peaks corresponding to them were observed in the diffraction patterns. Interestingly, when Cu distribution is homogenous as seen in 100 ppm doped sample, the high temperature annealing does not result in formation of Cu rich regions and maintains uniform distribution.

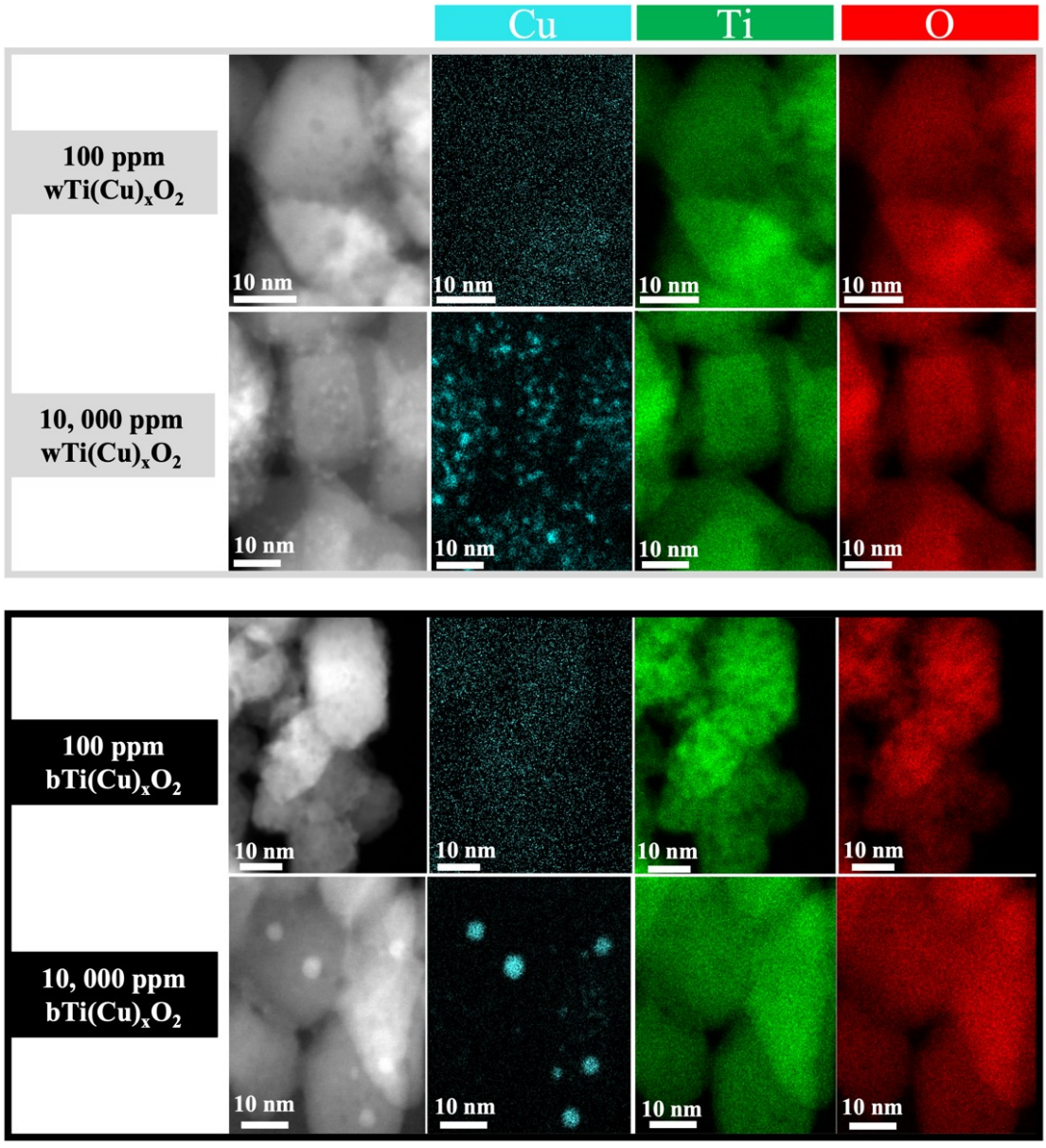

Figure 3.9. HAADF images and elemental maps of 100 and 10,000 ppm $wTiCu_xO_2$ and $bTiCu_xO_2$ NPs samples.

X-ray photoelectron spectroscopy (XPS) analysis was performed on the undoped TiO_2, $wTiCu_xO_2$ and $bTiCu_xO_2$ nanostructures to understand their surface chemistry. The high-resolution Ti 2p spectrum for different TiO_2 materials is shown in

Figure 3.10. The major components of the spectrum are Ti^{4+} $2p_{3/2}$ peak with maximum between 458.5 and 458.9 eV and Ti^{4+} $2p_{1/2}$ peak with maximum between the binding energies of 464.2 and 464.6 eV. With increasing amount of Cu doping in $wTiO_2$, an increase in Ti^{3+} species was also observed. The Ti^{3+} $2p_{3/2}$ and $2p_{1/2}$ peak maxima were at 457.2 and 462.4 eV, respectively. Since there is a difference in charge between Cu^{2+} and Ti^{4+} ions, doping of Cu generates OVs in the lattice of TiO_2 to maintain the charge neutrality.[213,214] With increasing amount of Cu, a corresponding increase in OVs and Ti^{3+} concentration in the crystal structure is expected. All the $bTiO_2$ samples except for the catalyst with 10,000 ppm Cu doping showed a higher amount of Ti^{3+} compared to its $wTiO_2$ counterpart. This is expected as $NaBH_4$ treatment results in the reduction of surface Ti^{4+} ions to Ti^{3+}. It is currently unclear why the concentration to Ti^{3+} decreases in 10,000 ppm Cu-doped catalyst. One hypothesis is that the Cu ions leach out of the NPs during the reduction process as evidenced by the fewer CuO regions in TiO_2 in the EDS map (**Figure 3.9**). Out diffusion of dopants from semiconductors during thermal annealing or post synthesis processing has been observed previously.[215,216]

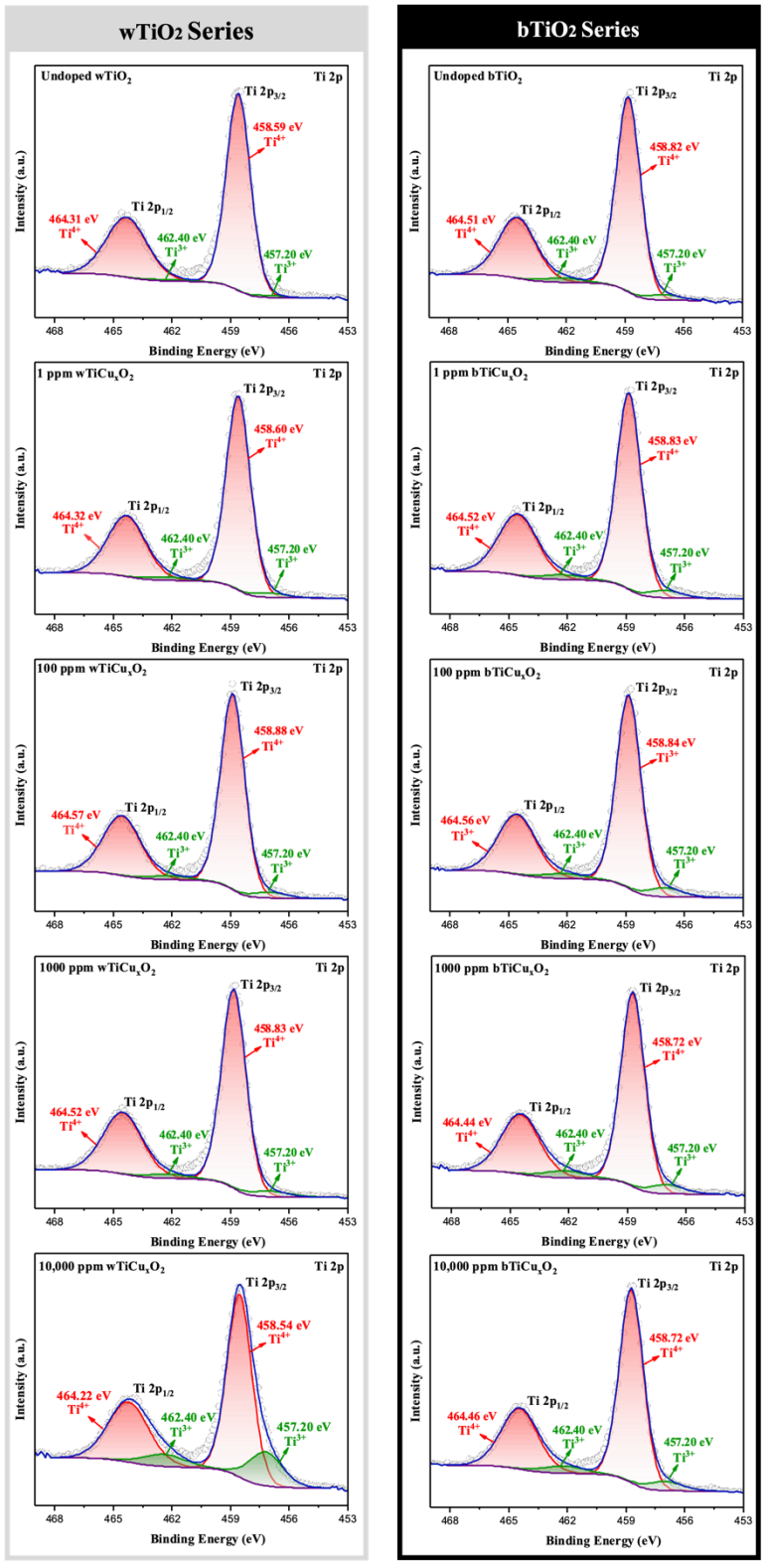

Figure 3.10. High-resolution XPS spectra of Ti 2p region for TiO_2 samples.

The high-resolution spectrum of Cu region was also obtained for these samples which is shown in **Figure 3.11**. For $wTiO_2$ samples, at 1 and 100 ppm, no significant Cu peak was observed. A low intensity peak was seen at 1000 ppm, but a proper signal was obtained at 10,000 ppm doping. For $bTiO_2$ samples, no significant Cu peak was observed further suggesting out diffusion of Cu ions during the reduction process.

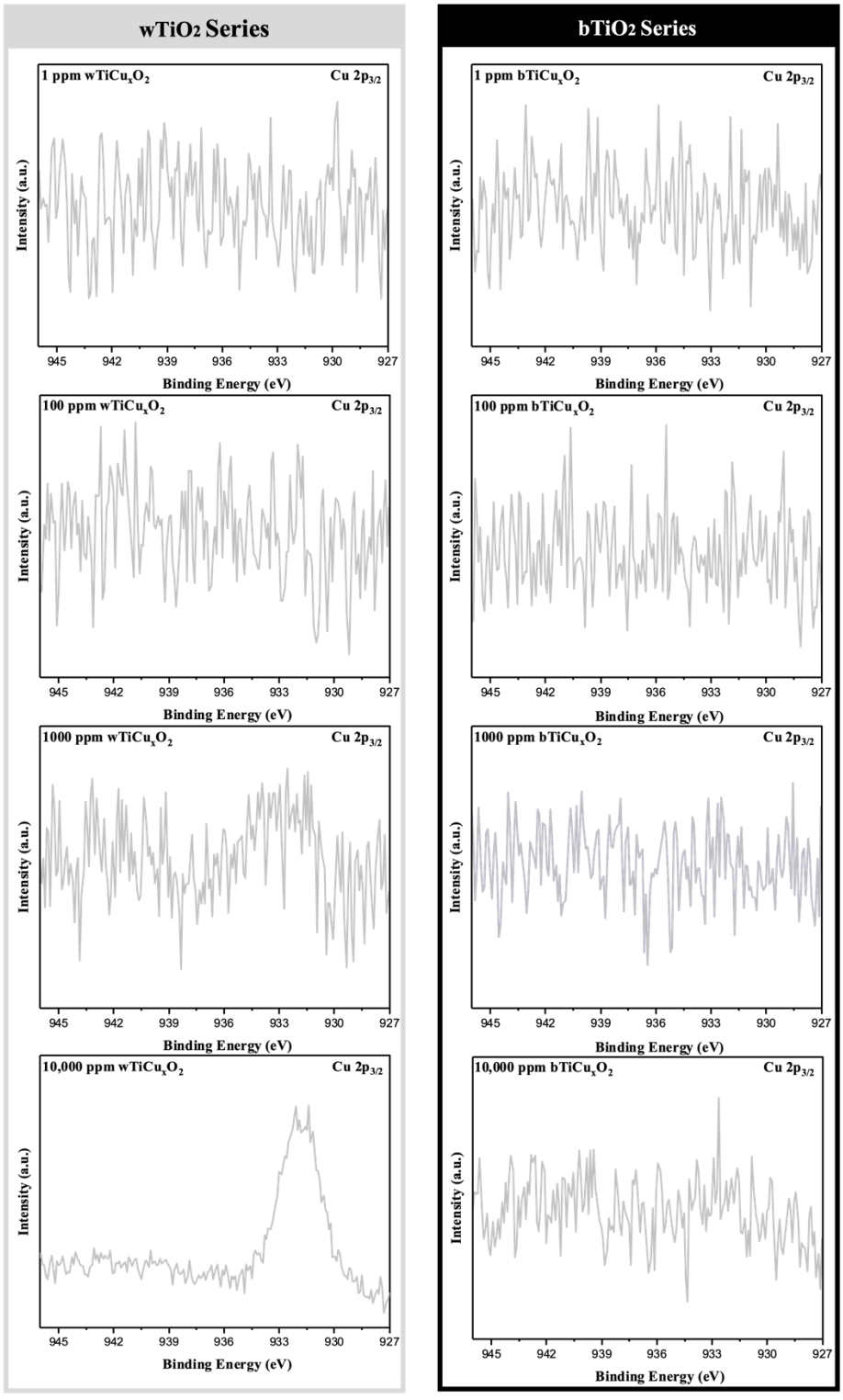

Figure 3.11. High-resolution XPS spectra of Cu 2p region for TiO_2 samples.

The optical properties of the TiO_2 catalysts were analyzed using diffuse reflectance spectroscopy recorded in absorbance mode as shown in **Figure 3.12** and **Figure 3.13**. The light absorption characteristics of the undoped TiO_2 and 1 ppm Cu containing TiO_2 catalysts were very similar to each other. At 100 ppm Cu-doping, a slight redshift in absorption was observed for $wTiO_2$. This is due to the introduction of mid-gap states from Cu^{2+} ions and OVs which lower the optical gap of the material. For the 1000 and 10,000 ppm Cu-doped samples, a broad absorption band between 400 and 700 nm was observed. This likely results from the amorphous CuO which has been shown to absorb in this region.[213,218] All of the $bTiO_2$ samples showed strong absorption in the visible region. This is predominantly due to the mid-gap states from the OVs in the reduced samples.[103]

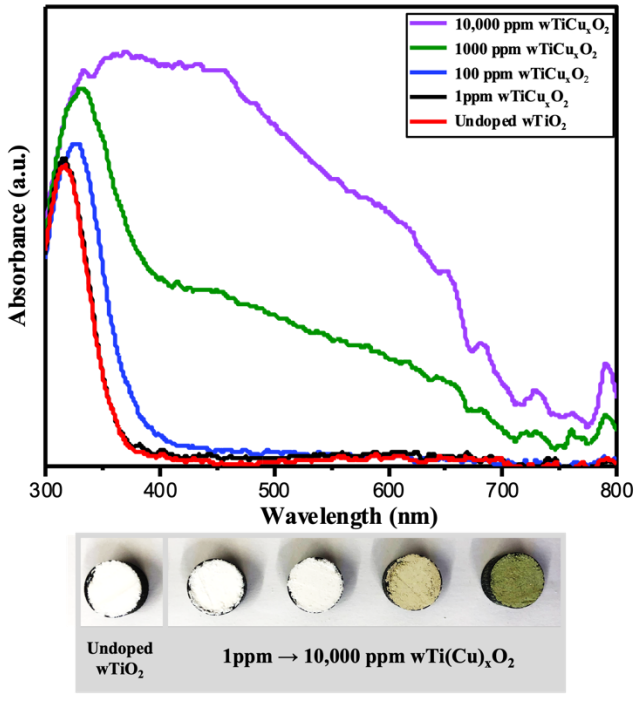

Figure 3.12. Absorbance spectra of undoped $wTiO_2$ and $wTiCu_xO_2$ samples.

All of the $bTiO_2$ samples showed strong absorption in the visible region. This is predominantly due to the mid-gap states from the OVs in the reduced samples.[103]

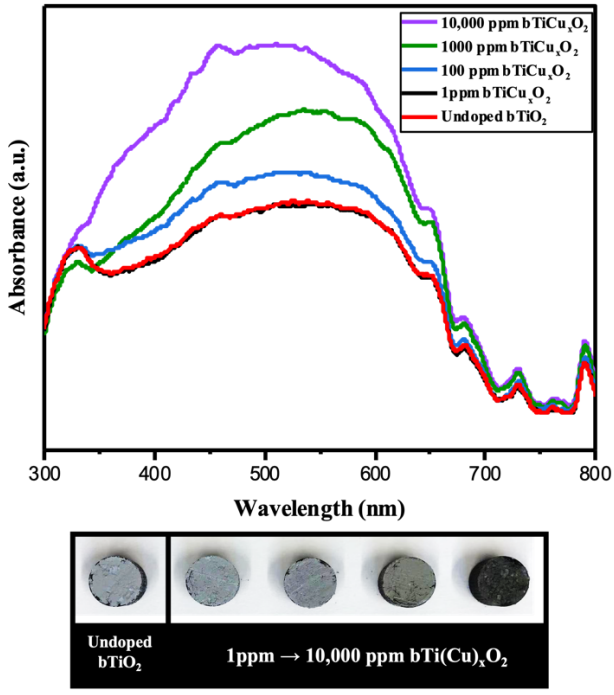

Figure 3.13. Absorbance spectra of undoped $bTiO_2$ and $bTiCu_xO_2$ samples.

The optical gaps of the catalysts were estimated using Tauc plots (**Figure 3.14**). For the $wTiO_2$ sample series, an optical gap of 3.22 eV was estimated for undoped TiO_2 and 1 ppm Cu-doped catalyst whereas the gap decreased to 3.0 eV for the 100 ppm Cu-doped sample. While a much smaller values of 2.37 and 1.41 eV was obtained for the 1000 and 10,000 ppm Cu-doped catalysts, it is important to highlight that the Tauc plot estimates for composite materials are inaccurate due to overlapping absorption from two different materials (i.e., TiO_2 and CuO in this case). The $bTiO_2$ samples had much lower optical gap compared to their unreduced counterparts. Undoped TiO_2 and 1 ppm $bTiCu_xO_2$ had an

optical gap of 1.50 eV whereas the 100, 1000, and 10,000 ppm Cu-doped sample gaps were 1.49, 1.47, and 1.43 eV, respectively. While these gaps are similar to each other, it is possible that some of the absorption at higher Cu-doping results from CuO similar to wTiO_2 samples. The extent of the CuO absorption might be lower in bTiO_2 due to out diffusion of Cu ions during the reduction process.

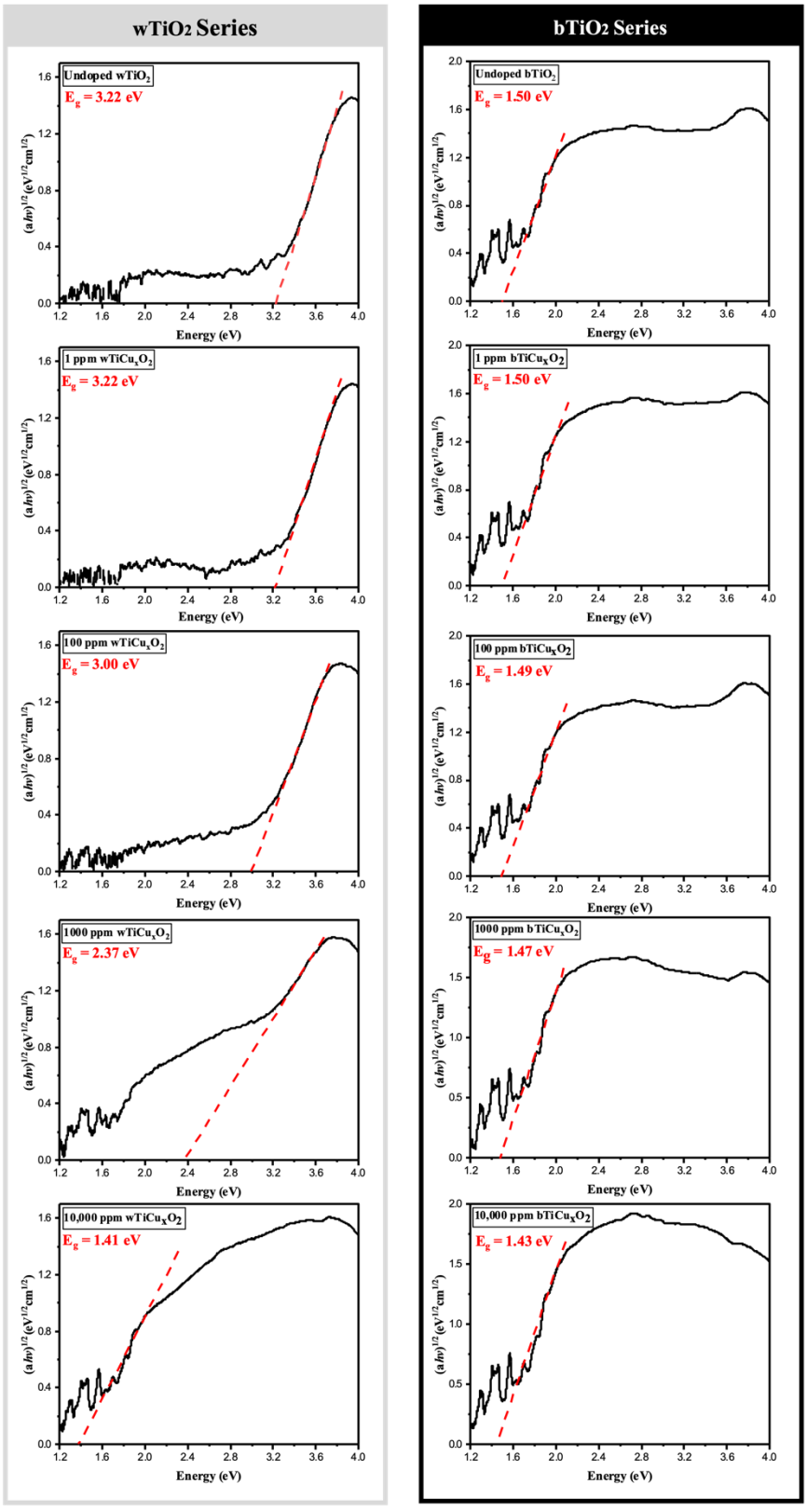

Figure 3.14. Tauc plots of undoped and $TiCu_xO_2$ samples.

3.4. Conclusion

Varying amounts of Cu-doped into TiO_2 catalysts were prepared using the solvothermal approach. These catalysts where further converted to hydrogenated TiO_2 *via* $NaBH_4$ treatment. The materials were characterized using powder XRD, SEM, TEM, XPS, EDS, and UV-vis spectrometer. Based on the characterization results discussed above, we hypothesize following structural features for different TiO_2 catalysts:

- The 1 ppm $TiCu_xO_2$ NPs either does not contain any Cu or very low amounts of dopant making it structurally quite similar to the undoped TiO_2 catalysts.

- The 100 ppm $TiCu_xO_2$ catalysts likely contain uniformly distributed Cu ions within the TiO_2 lattice, making it a true metal doped catalyst. The metal adds mid-gap states which redshifted the absorption edge and lowered the optical gap compared to the undoped samples.

- At Cu-doping concentrations of ≥1000 ppm, a composite material containing TiO_2/CuO or $TiCu_xO_2$/CuO is obtained. Instead of uniform distribution of Cu ions within the TiO_2 lattice, phase segregation occurs to form amorphous CuO domains within the TiO_2 NPs. This is reflected in the absorption profile which shows broad absorbance between 400 – 800 nm from CuO. During the reduction to form $bTiCu_xO_2$ NPs, out diffusion of Cu ions occurs to the surface of the NPs. During the HCl treatment, the Cu is likely etched away thus lowering the overall Cu content in the $bTiO_2$ samples as supported by the XPS results. The HAADF analysis (**Figure 3.15**) also showed pits in the 10,000 ppm $bTiCu_xO_2$ sample which likely forms from the removal of CuO domains that migrated to the surface.

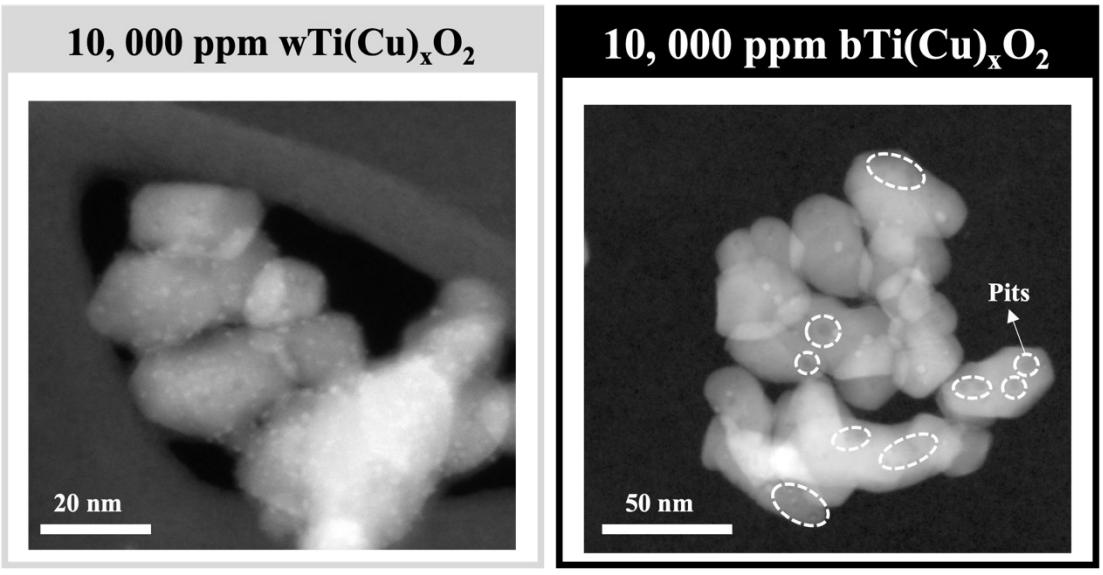

Figure 3.15. HAADF images of 10,000 ppm $wTiCu_xO_2$ and $bTiCu_xO_2$ NPs. The highlighted regions show the etch pits likely formed from the removal of CuO.

Further, EDS mapping also showed growth of CuO domains after the reduction reaction. The overall transformation of the structure is summarized in **Figure 3.16** below. The results in this chapter are important to understand the photocatalytic and antibacterial performance of these catalysts discussed in Chapters 4 and 5.

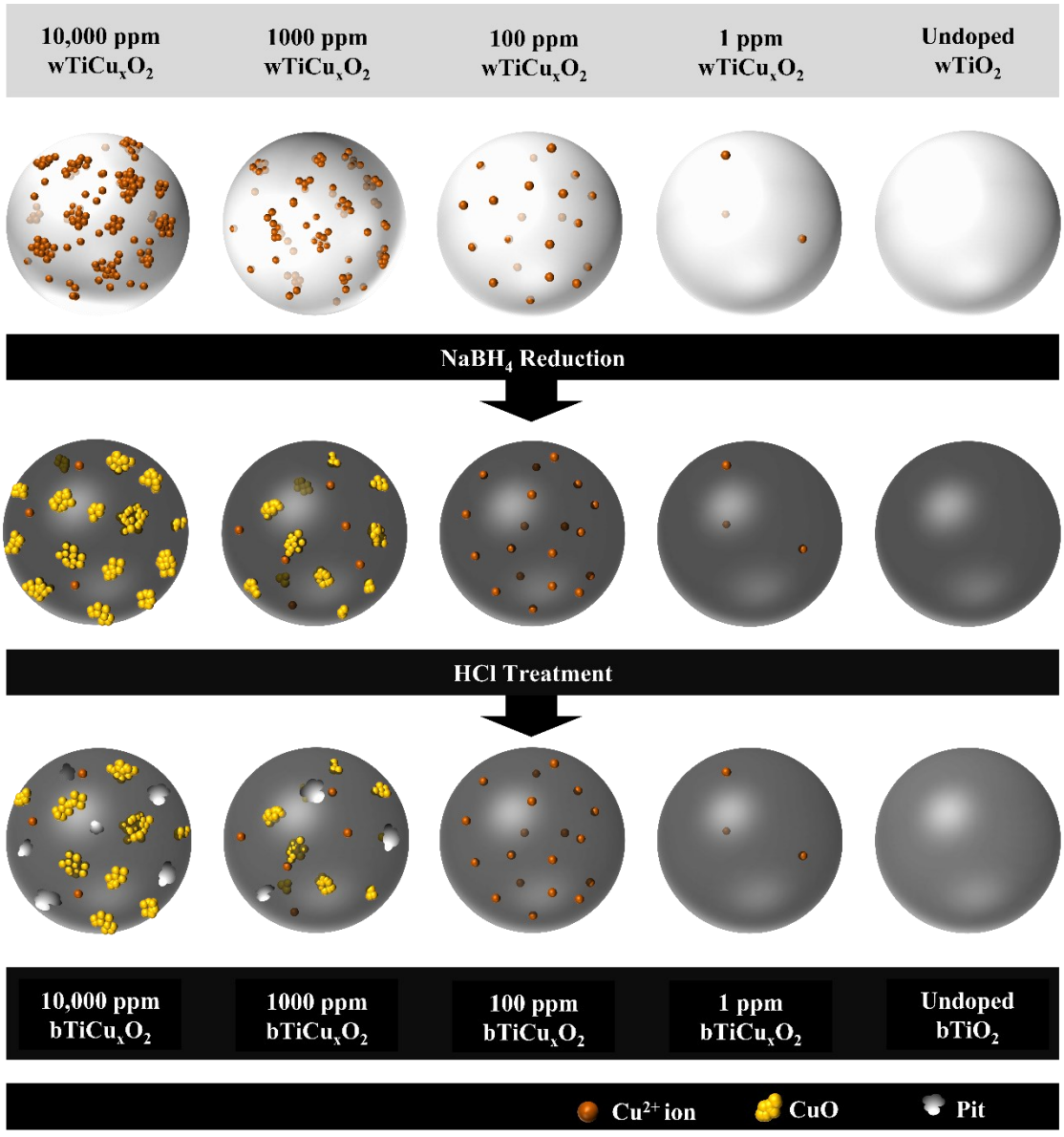

Figure 3.16. Schematic representation of structural transformation occurring in $TiCu_xO_2$ catalysts during the synthesis process.

CHAPTER 4. Photocatalytic Activity of Copper-doped Titanium Dioxide and Dye Degradation Mechanism

4.1. Introduction

As discussed in Chapter 3, various Cu-doped $wTiO_2$ and $bTiO_2$ were synthesized for photocatalytic dye degradation. The metal doping and hydrogenation are expected to (1) enhance the visible-light absorption and (2) reduce recombination of charge carriers on the interface which together can enhance the photocatalytic activity. In this chapter, the photocatalytic Rhodamine B (RhB) dye degradation using all the different TiO_2 NPs is discussed. In addition, a possible degradation mechanism and the type and amount of ROS was also explored and discussed here. Scavenger experiments investigated the key species that impact dye degradation reaction. The stability of the catalysts was investigated by a recycling experiment with five cycles under the same reaction condition.

4.1.1. Rhodamine B

Rhodamine B (RhB) is a type of coloured organic dye which is highly water-soluble and commonly used in the fabric manufacturing industries, as water tracers, fluorescent probes, in food packages, etc.[219] The molecular weight of RhB is 479.02 g mol^{-1} and has an absorption maximum at ~554 nm.[220] The IUPAC name of RhB is known as N-[9-(ortho-carboxyphenyl)-6-(diethylamino)-3H-xanthen-3-yli-dene] diethyl ammonium chloride),[219] which is a derivative of xanthene.[221] The dye is carcinogenic and poses a health threat to humans and wildlife by contaminating aquatic organisms or systems.[222] The conventional water treatment techniques such as sedimentation, filtration, and aeration can remove some RhB dye by phase transformation from the water, but the

dye cannot be effectively degraded.[222] If the dye is not completely removed, the residuals and by-products are toxic and can easily cause secondary contamination.[223] These troubles offer an opportunity for scientists who can find more excellent technologies for enhancing the quality of the water treatment before the dye enters the aquatic environment.

4.1.2. The Photocatalytic Mechanism for Dye Degradation

Photocatalytic degradation is an efficient tool that utilizes solar energy and a semiconductor photocatalyst to decompose both atmospheric and aquatic organic contaminants.[224] When a photocatalyst is illuminated with light of appropriate energy, excited electron-hole pairs are formed that migrate to participate in redox reactions on the surface of the catalyst. The final products generated after photocatalytic organic molecule degradation are water and carbon dioxide.[225–227] The degradation mechanisms can be classified into two categories: direct reaction (photolysis and photosensitization process) and indirect reaction (photoexcitation, water ionosorption, and oxygen ionosorption).[228]

Direct Reaction of Dye Photodegradation

RhB dye is a small molecule and can be easily adsorbed into the surface structure of the photocatalytic semiconductor by a physical process,[229] including intermolecular and dispersion forces.[230] When RhB dye is adsorbed into the photocatalyst, is acts as a sensitizer and allows the catalyst to absorb light in the visible range and make the degradation process possible under visible wavelength ($\lambda > 400$ nm) excitation.[231]

$$h\nu + \text{Dye} \rightarrow \text{Dye}_{ads}^{*} \qquad \text{Eq. 4.1}$$

$$\text{Dye}_{ads}^{*} + \text{semiconductor} \rightarrow \text{Dye}_{ads}^{\bullet +} + \text{semiconductor}^{-} \qquad \text{Eq. 4.2}$$

where ads stands for adsorbed dye.

As shown in Eq. 4.1 and Eq. 4.2, during visible light irradiation, the RhB dye is excited and injects an electron into the semiconductor resulting in an oxidized cation ($Dye^{\bullet+}$).[232] The cation may further react with surrounding molecules such as water to form other reactive species resulting in further degradation. The rate of degradation by dye photosensitization is typically slower compared to ROS and the process is summarized in **Figure 4.1**.[231,232]

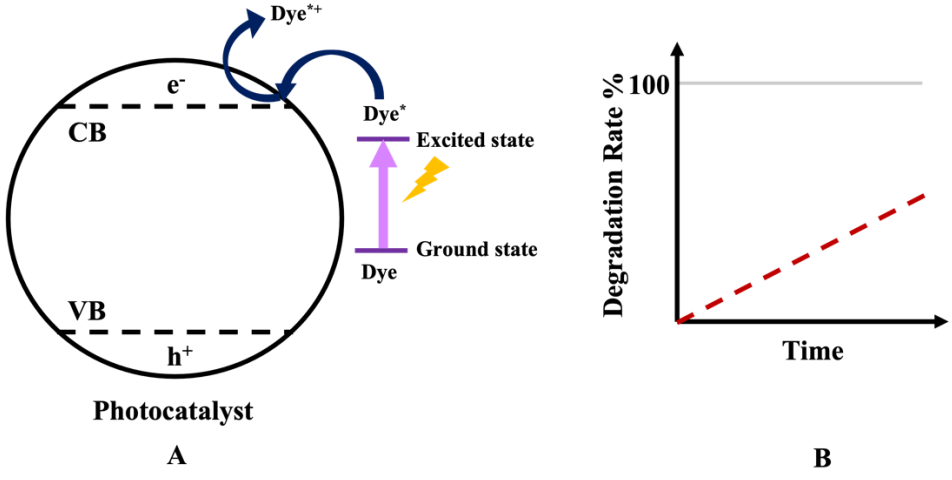

Figure 4.1. Dye photosensitization (electron-transfer) process: (A) adsorbed RhB* injects an electron into the CB of the semiconductor, and RhB dye is converted to the reactive cation $RhB^{\bullet+}$ and (B) RhB dye degradation rate *via* photosensitization process.[231]

The Indirect Degradation Mechanism of RhB Dye via Photocatalytic Reactions

Photoexcitation

When a photocatalyst absorbs light of energy higher than its optical gap, electrons and holes are generated. These electron and holes can then be directly transferred

to the dye molecules adsorbed onto the catalyst surface and cause dye degradation as presented by the Eq. 4.3 and Eq. 4.4.[233]

$$\text{Dye} + h^{+}_{VB} \rightarrow \text{oxidation products} \quad \text{Eq. 4.3}$$

$$\text{Dye} + e^{-}_{CB} \rightarrow \text{reduction products} \quad \text{Eq. 4.4}$$

Water Ionosorption

In this process, the holes at VB react with surrounding water to produce •OH (Eq.4.5).[234] The •OH generated on the surface of the semiconductor are strongly oxidizing species that is highly active in decomposing RhB dye (Eq. 4.6).[235] The extent of degradation relies on the stability level and concentration of •OH species.[236]

$$h^{+}_{VB} + H_2O_{ads} \rightarrow H_{ads}^{+} + {\bullet}OH_{ads}\ (+1.99\ \text{V vs. NHE}) \quad \text{Eq. 4.5}$$

$$\text{Dye} + {\bullet}OH_{ads} \rightarrow CO_2 + H_2O \quad \text{Eq. 4.6}$$

Oxygen Ionosorption

The electrons in the CB can react with surrounding oxygen to generate superoxide ions ($O_2^{\bullet-}$) (Eq. 4.7).[237] The $O_2^{\bullet-}$can take part in the further reaction with holes to generate singlet oxygen ($^1O_2$) (Eq. 4.8).[238] $O_2^{\bullet-}$ and $^1O_2$ are active ROS for improving RhB dye degradation (Eq. 4.9).[231] It is argued that $O_2^{\bullet-}$ and $^1O_2$ are not the direct ROS to degrade RhB and in actuality these radicals are protonated in water to form •OH species that participate in RhB dye degradation.[228,234,235,239,240]

$$e^{-}_{CB} + O_{2ads} \rightarrow O_2^{\bullet-}\ (-0.18\ \text{V vs. NHE}) \quad \text{Eq. 4.7}$$

$$O_2^{\bullet-} + h^{+}_{VB} \rightarrow {}^1O_2 \quad \text{Eq. 4.8}$$

$$Dye + {}^{1}O_2 + O_2^{\bullet-} + \bullet OH \rightarrow CO_2 + H_2O \qquad \text{Eq. 4.9}$$

Therefore, the photocatalytic dye degradation depends on, 1) amount of light absorption by the catalysts, 2) the concentration and rate of electron-hole generation, 3) electron-hole pair recombination, and 4) the adsorption of RhB dye, oxygen, and water molecules on the surface of the photocatalyst. Increasing the lifetime of ROS have a positive effect on dye decomposition. The overall photocatalytic dye degradation process is presented in **Figure. 4.2**. More than one ROS species can be responsible for the reaction which will show a synergistic response.[241]

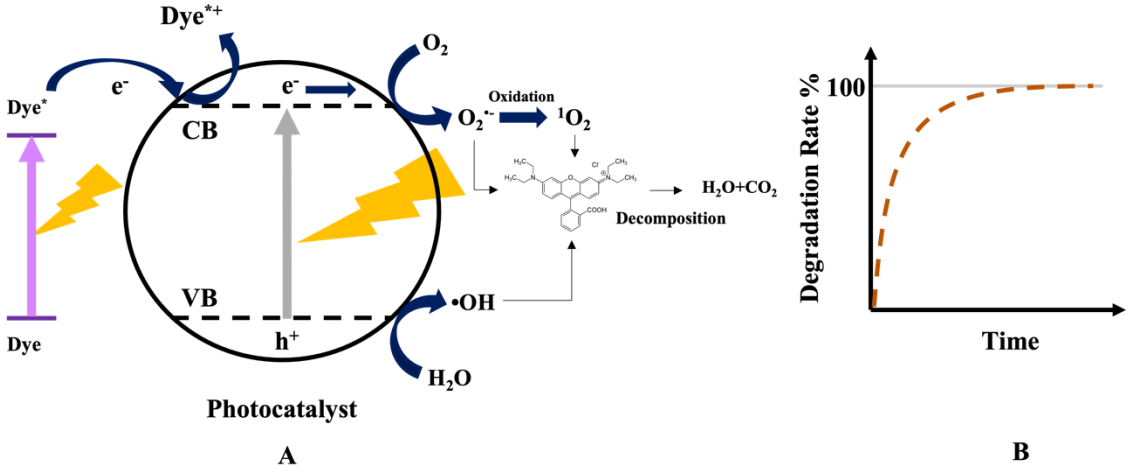

Figure 4.2. (A) photocatalytic degradation reactions of dyes and (B) its mimetic degradation rate.

4.2. Experimental Methods

4. 2.1. Materials

Rhodamine B (RhB, 95%), 1,4-benziquinone (BQ), sodium azide (NaN_3, 99.5%), ammonium oxalate monohydrate (AO, 99.5%), potassium bromate ($KBrO_3$, 99.8%) were purchased from Sigma Aldrich. Methanol (95%) was purchased from VWR International Ltd. All reagents were used as received without further purification. Nano-pure water was obtained from a Thermo Scientific Barnstead Ultrapure Water Purification System.

4..2.2. Material Synthesis

All of nanomaterials were prepared as discussed in section 3.2

4. 2.3. Materials Characterization

Powder XRD, SEM, TEM, HRTEM, XPS, and UV-vis were performed as Chapter 2 discussed as in Chapter 3.

4.2.4. Experimental Method

Photocatalytic Degradation Experiment

The degradation of RhB aqueous solution was monitored to evaluate the photocatalytic performance of different samples. The mixture included RhB (0.005 mg/mL, 20 mL) and TiO_2 catalyst (20 mg) were irradiated with a 1000 W LED lamp equipped with a UV cut-off filter （$\lambda > 400$nm). The light intensity was 100 mW cm^{-2} for simulating one

sun, which was measured by PM100USB Power detector with standard photodiode sensor. The mixture was stirred at 400 rpm for 30 min in a dark environment to reach the adsorption equilibrium. An initial concentration of RhB was measured before the adsorption process, which was used to identify the dye adsorption ability of the catalyst. The total irradiation time was 2 hours, and the experiments were performed at room temperature. 0.4 mL of the reaction mixture was taken at regular intervals of 20 minutes, and the supernatant was collected by centrifuging at 3900 rpm for 10 min. The absorbance of supernatants was analyzed by the absorbance program of FLUOstar Omega Microplate Reader. Unless stated otherwise, all RhB dye absorbance measurements were performed in a 96-well plate. The concentration of RhB dye was calculated using a standard curve (Eq. 4.10)

$$A = 0.1543C–0.000013 \ (R^2 = 0.9994) \qquad \text{Eq. 4.10}$$

where A was the absorbance of suspension and C was the concentration of RhB dye in mg/mL.

The final removal efficiency of the photocatalyst was calculated as follows (Eq. 4.11):

$$C=C_t/C_0 \qquad \text{Eq. 4.11}$$

where C_0 is the initial concentration of RhB, and C_t is the concentration of RhB at different irradiation times.

The kinetics of the photodegradation processes was described by a pseudo-first-order kinetic model as follows (Eq. 4.12):

$$\ln(C_0/C) = kt \qquad \text{Eq. 4.12}$$

where k is the rate constant, and t is the irradiation time.

All photodegradation tests were repeated in triplicate to identify the reproducibility and accuracy of the results, which were found to be within acceptable limits (<1%). Blank groups were performed in the absence of the catalysts under light irradiation. The schematic of the experiment setup is shown in **Figure. 4.3**.

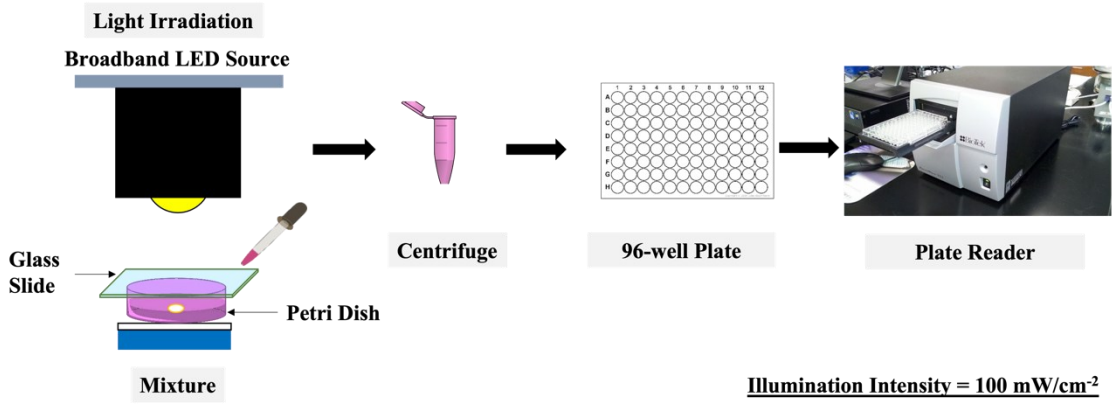

Figure 4.3. The schematic representation of the experimental setup for photocatalytic degradation experiments using $TiCu_xO_2$ NPs.

Mechanism Studies

In addition to screening the different photocatalysts, a series of tests were performed to investigate the mechanism pathway driving the photocatalysis. This was performed by adding scavenger agents that extract certain reactive species from the solution. The scavenger tests were conducted under the same experimental condition as mentioned above. If the RhB dye removal efficiency of photocatalysts decreases considerably with specific scavengers, it would be considered that this is associated with

the removal of ROS responsible for the photodegradation of RhB. The amounts of different scavenger reagents used in these studies are tabulated below.

Table 4.1. Amounts of different scavengers added to the photocatalysis reactions to trap specific ROS.

Scavenger	Amounts	Reactive Species Trapped
Methanol	200 mM	•OH
AO	10 mM	Hole
BQ	0.1 mM	$O_2^{\bullet-}$
NaN_3	200 mM	$^1O_2$
$KBrO_3$	5 mM	Electron

Reusability Experiment

To investigate the reusability of 100 ppm $bTiCu_xO_2$ NPs, the NPs were carefully collected after completing the first degradation measurements, and it was separated by centrifugation (4000 rpm for 8 min). It was subsequently washed with ethanol and water until the supernatant had no absorption from previous dye solution. It was then dried in a convection oven for the second experiment in fresh rhodamine B solution. These steps were repeated for each cycle and the catalyst was tested for five cycles.

Solar Light-induced Rhodamine Degradation

To investigate the photocatalytic activity of 100 ppm $bTiCu_xO_2$ NPs under natural solar light, the degradation experiments were carried out in a Petri dish between 11:00 and 15:00 on November 25th (winter season) at 46.1° North and 60.1° W (Cape

Breton, Nova Scotia, Canada). The solar light intensity was between 10 and 16 mW cm^{-2} as measured using a PM100USB Power plus Energy Sensor. Except for the irradiation time and intensity, another experimental condition was the same as mentioned above.

4.3. Result and Discussion

4.3.1. The Photocatalytic Performance of Various TiO_2 NPs for Dye Degradation.

The photocatalytic performance of all $TiCu_xO_2$ NPs catalysts was assessed by the degradation of RhB dye. For the comparison study, the photocatalytic performance of undoped TiO_2 catalysts was also performed under the same experimental conditions. A controlled study in the absence of a catalyst suggested that RhB dye was stable under visible light (**Figure 4.4** and **4.5**, khaki plot). All the synthesized catalysts underwent 30 min of adsorption equilibrium process in a dark environment. A very small reduction in concentration was observed in the presence of all catalysts due to adsorption on process.

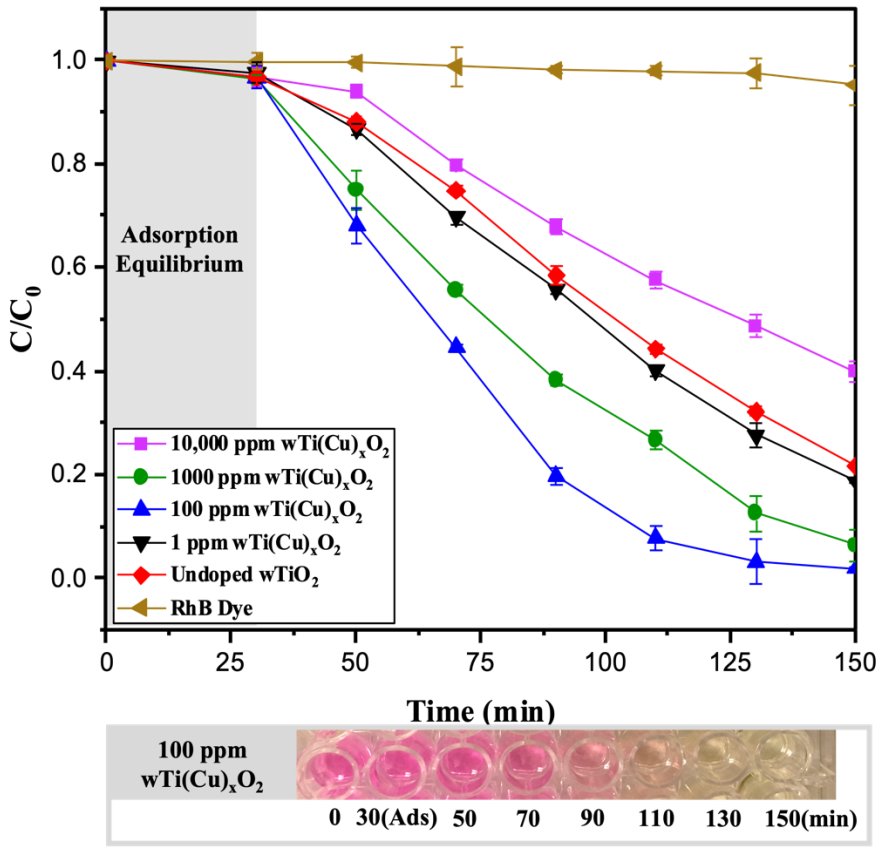

Figure 4.4. Photocatalytic degradation performance of $wTiCu_xO_2$ NPs.

Among the non-hydrogenated TiO_2 catalysts (**Figure 4.4**), 100 ppm $wTiCu_xO_2$ catalyst showed the highest activity with most of the RhB degraded by 80 min of illumination (blue plot). This is followed by 1000 ppm $wTiCu_xO_2$ catalyst (green plot). The undoped $wTiO_2$ (red plot) and 1 ppm $wTiCu_xO_2$ catalyst (black plot) had very similar photocatalytic activity. This is expected as the composition and structure analysis discussed in Chapter 3, showed these materials to be quite similar to each other. Surprisingly, 10,000 ppm $wTiCu_xO_2$ catalyst showed the lowest photocatalytic activity (purple plot). These observations suggest that it is important to have a uniform distribution

of Cu ions in the NPs for high photocatalytic activity. Electron microscopy showed this to be true to 100 ppm $wTiCu_xO_2$ sample. As the Cu dopant concentration increases, CuO grains start to form. Despite high light absorption by 1000 and 10,000 ppm $wTiCu_xO_2$ samples, these showed lower activity. It is possible that the CuO grains themselves absorb light and the carriers generated in this material recombine at the CuO/TiO_2 interface and do not make it to the catalyst surface.[242] The hybrid morphology of TiO_2/CuO is detrimental for photocatalytic dye degradation experiments and very high Cu concentration led to performances lower than undoped TiO_2 samples.

For the hydrogenated TiO_2 catalysts (**Figure 4.5**), 100 ppm $bTiCu_xO_2$ catalyst still showed the highest activity (blue plot). In fact, it had better activity compared to its non-hydrogenated form with 99% of the RhB degraded by 60 min of illumination. This is likely due to the higher light absorption and Ti^{3+} defects in $bTiCu_xO_2$ catalyst. Similar to the non-hydrogenated catalysts, undoped $bTiO_2$ catalyst (red plot) and 1 ppm $bTiCu_xO_2$ catalyst (black plot) had similar activities due to similar structure and composition. The 1000 ppm $bTiCu_xO_2$ catalyst performed worse then the undoped samples (red plot). This is likely due to the loss of Cu ions during the hydrogenation step. For the hydrogenated sample, 10,000 ppm $bTiCu_xO_2$ catalyst (purple plot) had the lowest activity, though it performed better than its $wTiCu_xO_2$ counterpart. The improved activity could be due to introduction of Ti^{3+} defect sites on the surface.

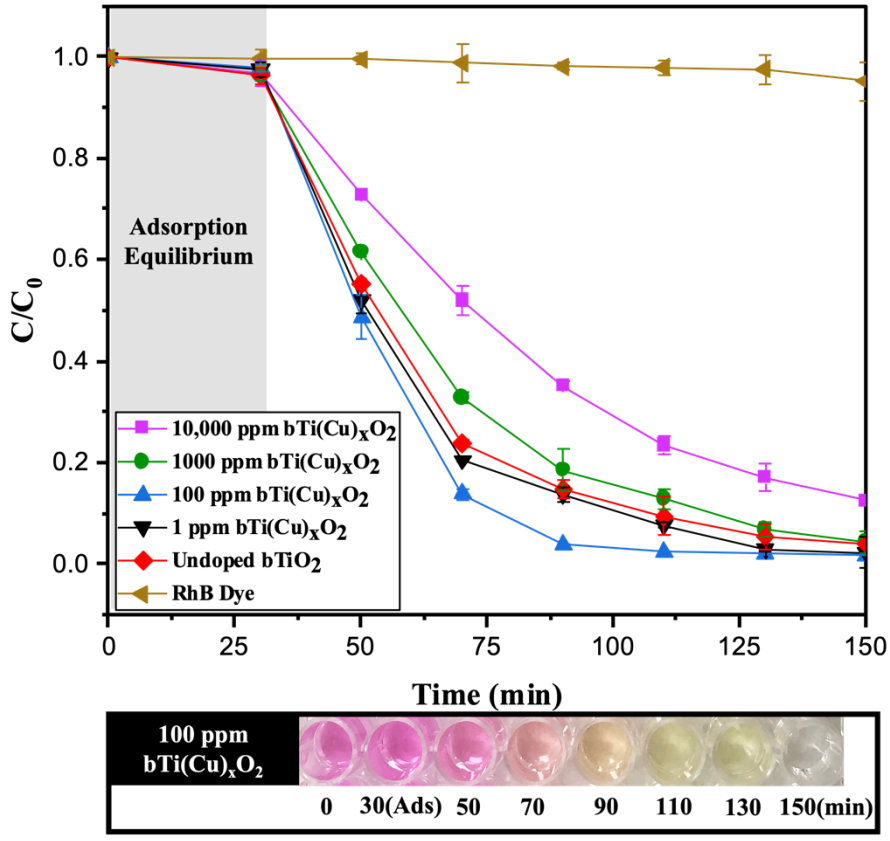

Figure 4.5. Photocatalytic degradation performance of $bTiCu_xO_2$ NPs.

Figure 4.6 shows the pseudo-first-order kinetic plots for the photocatalytic degradation of RhB. Both the 100 ppm $wTiCu_xO_2$ and $bTiCu_xO_2$ catalysts had 2-3 times higher rate than the 10,000 ppm $wTiCu_xO_2$ catalyst. These results clearly illustrate that a lower and uniform Cu dopant is better for visible-light-driven photocatalyst for the degradation of coloured dye pollutants.

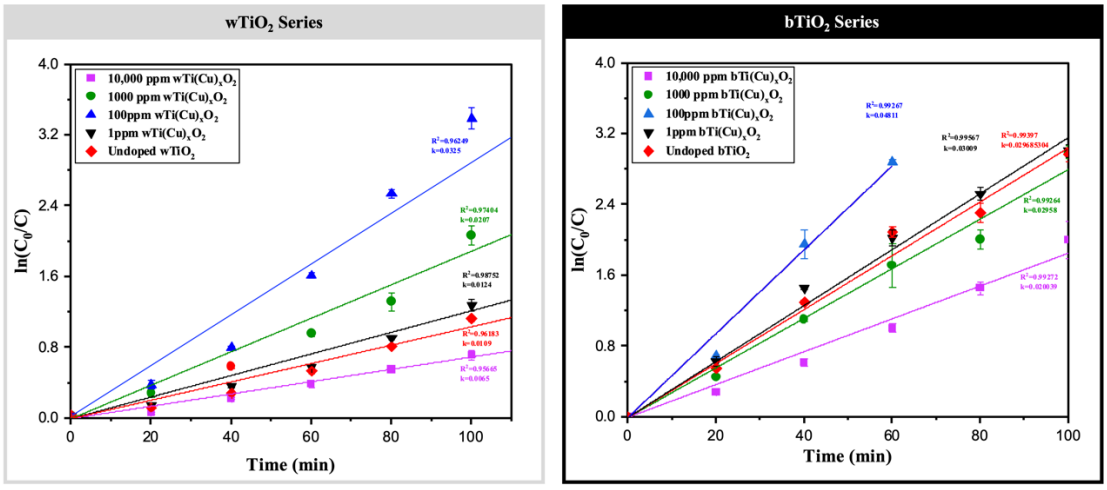

Figure 4.6. The photodegradation kinetics of $wTiCu_xO_2$ and $bTiCu_xO_2$ NPs.

The ability to recycle these catalysts was evaluated using the 100 ppm $bTiCu_xO_2$ catalysts. The activity of this catalysts over five cycles are presented in **Figure 4.7.** The activity of 100 ppm $bTiCu_xO_2$ catalyst was constant up to 95% of its original activity after five successive photodegradation experiments. A slight decrease in the photodegradation performance during the recycling experiment likely results from the catalyst loss from the washing and centrifuge process.

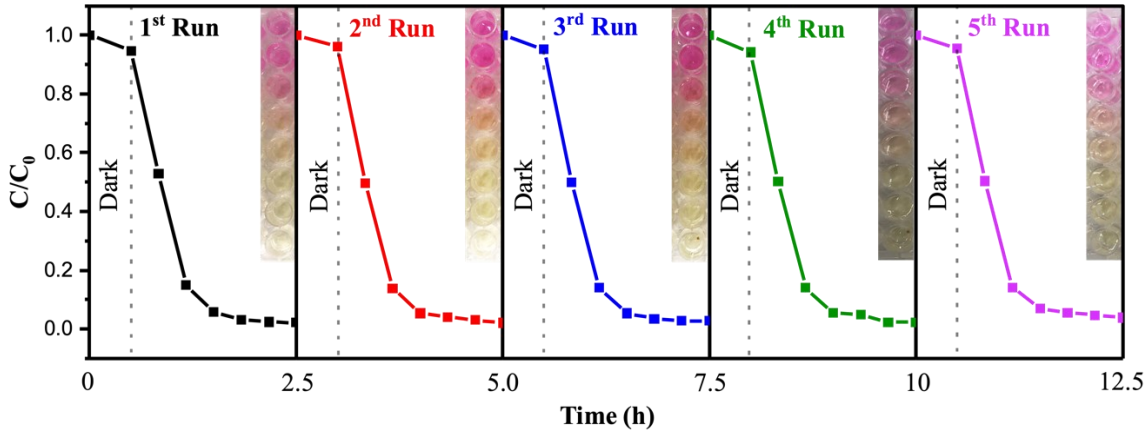

Figure 4.7. Recyclability of the 100 ppm bTiCu$_x$O$_2$ catalyst for degradation of RhB dye.

The catalysts were analysed after the recyclability experiments to evaluate any morphological and structural changes. The TEM analysis (**Figure 4.8**) of the initial and reused 100 ppm bTiCu$_x$O$_2$ catalyst showed no change in their morphological.

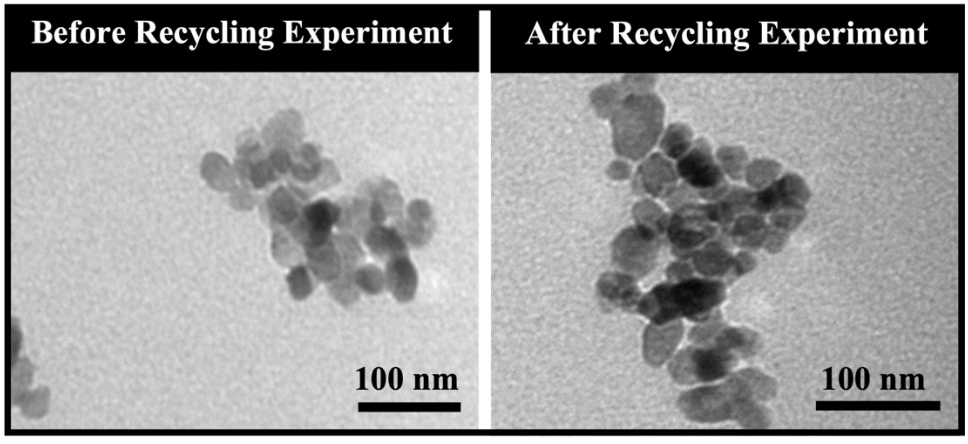

Figure 4.8. TEM images of 100 ppm bTiCu$_x$O$_2$ catalyst before and after the recycling experiment.

The powder XRD patterns (**Figure 4.9**) of 100 ppm $bTiCu_xO_2$ catalyst also did not change before and after the recycling experiment which confirms its structural stability. Thus, the synthesized 100 ppm $bTiCu_xO_2$ catalyst not only has high photocatalytic activity but also high stability.

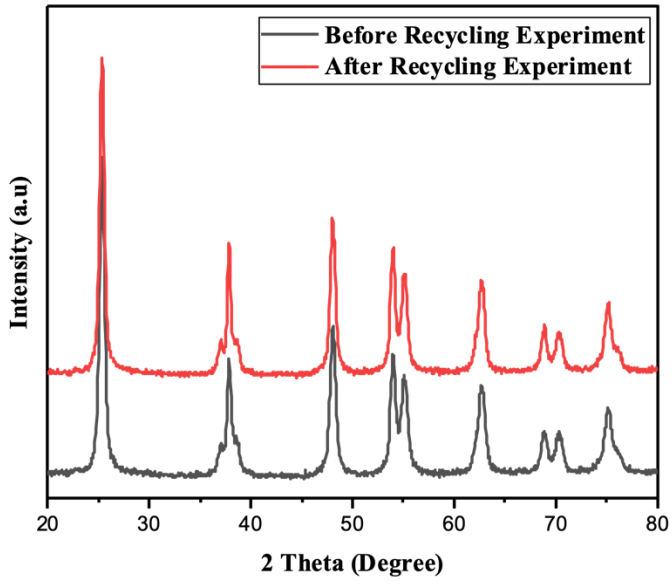

Figure 4.9. The powder XRD patterns of initial and reused 100 ppm $bTiCu_xO_2$ catalyst.

While good photocatalytic activity was observed with simulated light in the lab, it is important to demonstrate the utilization of these materials in natural sunlight. The dye by itself did not show any appreciable dye degradation under natural sunlight in 4 h. The 100 ppm $bTiCu_xO_2$ catalyst showed ~100% degradation after 4 h in natural sunlight (**Figure 4.10**). This is slower compared to the simulated light used in the lab; however, this is due to the difference in light intensity. The simulated light had an intensity of 100 mW cm^{-2} whereas natural sunlight intensity varied between 10-16 mW cm^{-2}. Despite the

slower rates, this shows the promise of utilization of sunlight to drive dye degradation using these catalysts. The illumination intensity can be enhanced by using lens to concentrate the light.

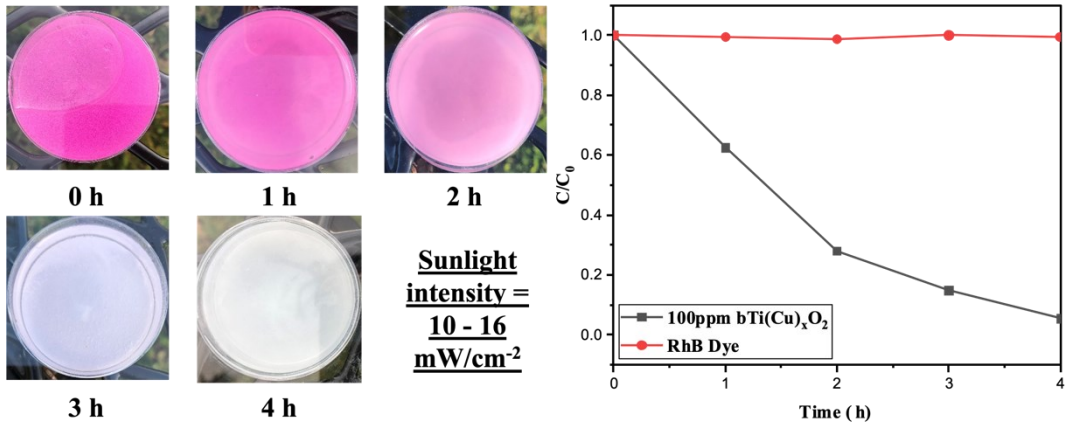

Figure 4.10 Degradation of RhB dye with 100 ppm $bTiCu_xO_2$ catalyst and RhB dye in the presence of sunlight irradiation.

4.3.2 Photocatalytic Mechanism of Dye Degradation

To understand the mechanism of photocatalytic degradation, scavenger tests were conducted for probing the most critical reactive species involved in the photodegradation process. The mechanistic investigations were performed using the 100 ppm $wTiCu_xO_2$ and $bTiCu_xO_2$ catalysts under visible-light irradiation. Different scavengers such as methanol, BQ, AO, $KBrO_3$, and NaN_3 were introduced into the reaction system for trapping •OH, hole, $O_2^{\bullet-}$, electron, and $^1O_2$, respectively.

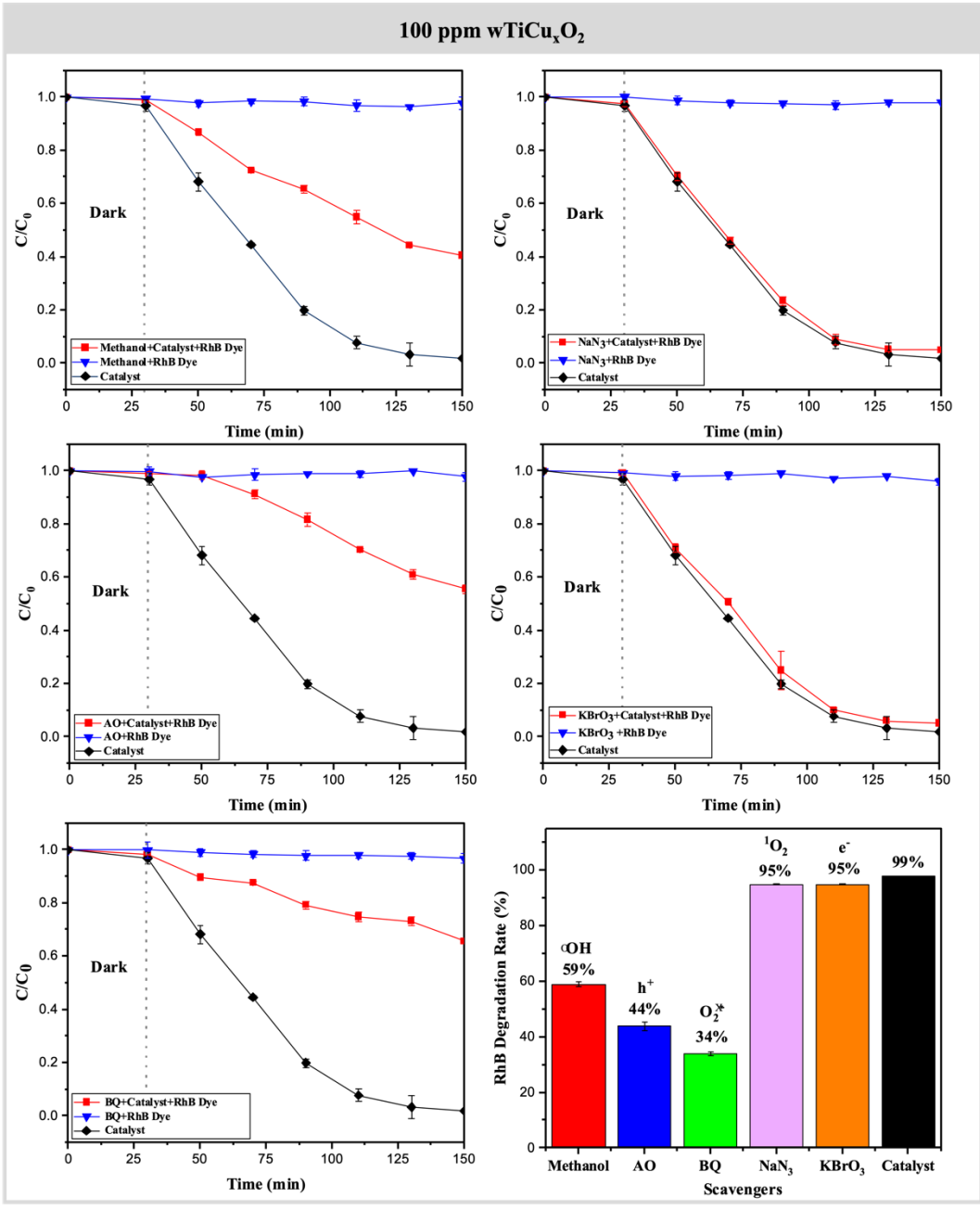

Figure 4.11. The photocatalytic activity of 100 ppm wTiCu$_x$O$_2$ catalysts in the presence of methanol, AO, BQ, NaN_3, and $KBrO_3$.

As shown in **Figure 4.11**, the photodegradation efficiency of RhB with wTiCu$_x$O$_2$ catalyst decreased the most in the presence of $O_2^{\cdot-}$ scavengers (BQ) and hole scavengers (AO). This indicates that these are the dominant species involved in the

degradation. Decrease in photocatalytic activity was also observed with methanol, indicating that •OH species also contribute to RhB dye photodegradation reactions but to a lesser extent than $O_2^{\bullet-}$ and holes. In the presence of $KBrO_3$ and NaN_3, no change in photodegradation performance was observed, indicating that electrons and $^1O_2$ were not crucial species to degrade RhB. The surface Cu ions can accept an electron from the CB of TiO_2 and assist in the formation of $O_2^{\bullet-}$ species which degrades RhB dye (**Figure 4.12**).[197,198] The holes left in the VB of TiO_2 participate in the formation •OH species which can decompose dye. Since 100 ppm Cu-doped sample has higher distribution of isolated Cu ion species that can act as electron acceptors, it likely has enhanced photocatalytic activity.

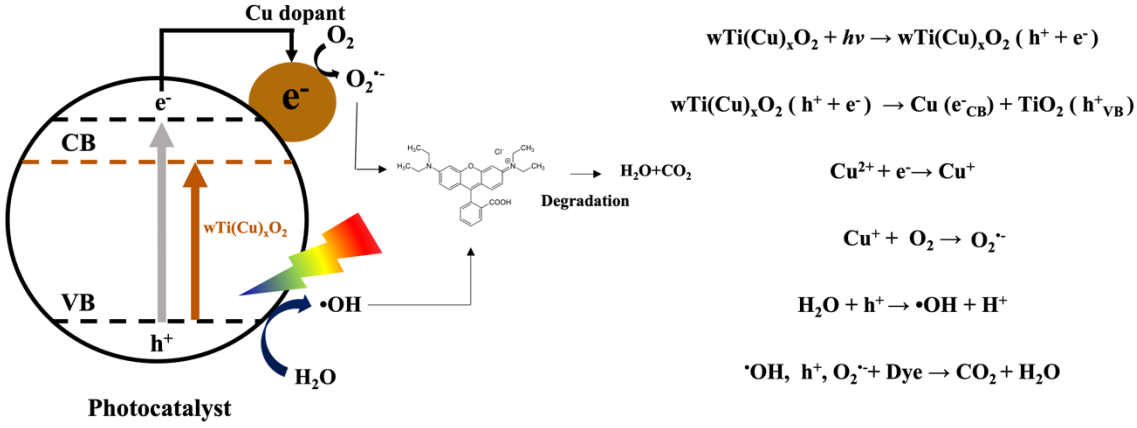

Figure 4.12. The schematic representation of photocatalytic mechanism of RhB dye degradation.

Similar to $wTiCu_xO_2$ catalyst, mechanistic investigations were also performed using 100 ppm $bTiCu_xO_2$ catalyst and the results are shown in **Figure 4.13**. Similar to the

$wTiCu_xO_2$ catalyst, no significant decrease in catalytic activity was observed in the presence of $KBrO_3$ and NaN_3 for the hydrogenated catalyst. However, surprisingly no significant change to degradation was observed in the presence of methanol (•OH scavengers). Further, small suppression of degradation was observed BQ ($O_2^{\bullet-}$ scavenger) and AO (hole scavengers). These results indicate that the ROS generation is not the major degradation pathway in $bTiCu_xO_2$ catalyst, and the mechanism differs from $wTiCu_xO_2$ catalyst. XPS spectra showed that a higher concentration of Ti^{3+} and OVs are present in 100 ppm $bTiCu_xO_2$ catalyst compared to the non-hydrogenated counterpart. Ti^{3+} and OVs are critical surface defects for facilitating the adsorption of the dye molecules. The dominant degradation mechanism is likely from the direct transfer of charge carriers to surface adsorbed dye molecules.

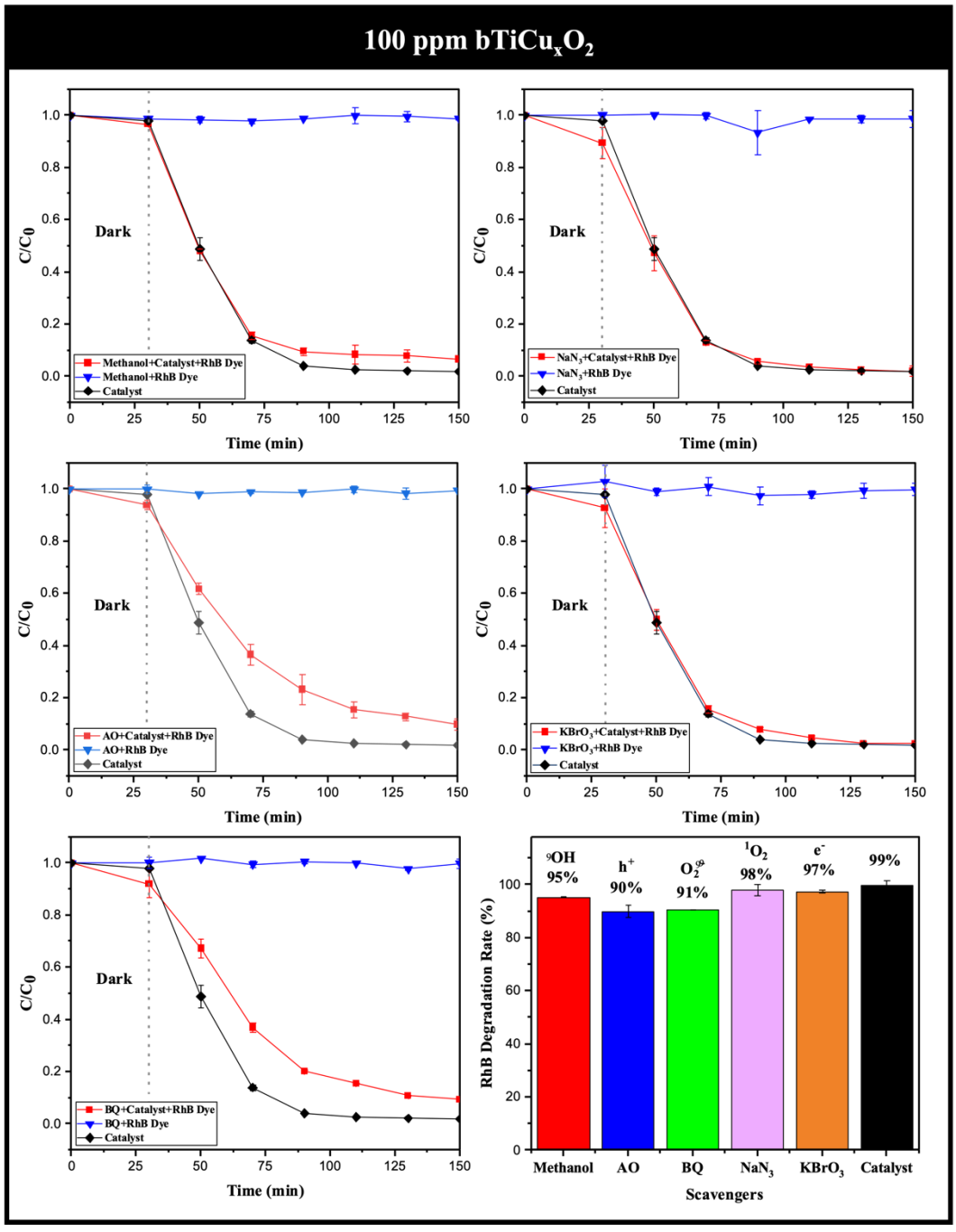

Figure 4.13. The photocatalytic activity of 100 ppm bTiCu$_x$O$_2$ catalysts in the presence of methanol, AO, BQ, NaN_3, and $KBrO_3$.

4.4. Conclusion

In summary, the catalysts screening showed that 100 ppm $wTiCu_xO_2$ and $bTiCu_xO_2$ catalysts were the best performing among all the TiO_2 materials. Despite high light absorption, 1000 and 10,000 ppm $wTiCu_xO_2$ samples had poor activity. This indicates that high light absorption is not the dominant factor in enhancing photocatalytic activity in these materials. It is also important to have more uniform atomic distribution of Cu ions within the TiO_2 particle. ROS species $O_2^{\bullet-}$ and •OH and holes were found to be significant for dye degradation in $wTiCu_xO_2$ catalysts. However, for $bTiCu_xO_2$ catalyst, the surface defects were found to facilitate the adsorption of dye onto the catalysts and direct transfer of carries to the dye molecules from the catalyst results in degradation. The catalysts were found to be stable over multiple cycles and showed degradation in natural sunlight.

CHAPTER 5. Antibacterial Properties of Copper-doped Titanium Dioxide Catalysts

5.1. Introduction

In addition to degradation of organic molecules such as dyes discussed in Chapter 4, TiO_2 NPs are also capable of inactivating pathogenic microorganisms such as bacteria and viruses. This can be achieved through multiple pathways in involving charge carriers (electron and holes) and/or ROS species, similar to the dye degradation. However, the lifetime of the ROS is short and requires its continuous formation during photocatalytic reaction for maintaining optimum antibacterial efficiency.[243] Inhibition of electron-hole recombination and improvement of water and O_2 adsorption ability on the TiO_2 surface is the most common method for increasing the yield of ROS and the antimicrobial activity.[244–247] Studies have been published previously that have pointed out that Cu based compounds have a superior antibacterial performance.[248–253] In this chapter, the antibacterial performance of undoped TiO_2 and $TiCu_xO_2$ NPs using *E. coli* was explored.

5.1.1. Factors modify in Antibacterial Efficiency

E. coli are the main species in the fecal coliform group, which is a very harmful pathogens, and its presence is usually considered an effective probe of water fecal contamination.[254,255] The antibacterial interaction process is very complex between TiO_2 photocatalyst and tested microbes which involves factors such as direct contact, bacteria oxidative stress, and ROS attack are crucially important for understanding the mechanism of antibacterial activity of photocatalyst. [256,257]

A Direct Contact Process for Bringing Antibacterial Species to Cell Structure

E. coli are gram-negative bacteria which are increasingly becoming pathogen of concern due to their drug resistance.[258] *E. coli* consist of an outer cell membrane, an inner membrane, chromosomal DNA, and plasmid.[259] The outer layer of the cell membrane can be the initial site of reaction with the TiO_2 photocatalyst. The cell membrane of gram-negative bacteria has two lipid membranes with an intermediate peptidoglycan layer with the outer membrane rich in negatively charged lipopolysaccharides (LPS).[260]

LPS located on the outside of the cell wall are mainly responsible for protecting the cell from chemical attacks.[259] This layer is made of fatty acids and is very sensitive to ROS driven lipid peroxidation reactions that can disrupt this layer (**Figure 5.1 (1)**).[261] Furthermore, the LPS layer allows cations and anions through porins to the periplasm.[262] Na^+ and K^+ pass through the porins to maintain cell osmotic pressure at the rate 10^5 ions per channel per second,[262] which can introduce ROS in the cell structure at the same time (**Figure 5.1 (2)**).[260] For enhancing the electron-hole separation, TiO_2 is usually modified by metal or metal compounds. Metal ions with a positive charge can leach from the photocatalyst and easily attach to the LPS layer by electrostatic force and travel through porins resulting in cell disruption (**Figure 5.1 (3)**).[256] The rupture process of the phospholipid layer depends on the morphology and surface roughness of the nanomaterials. During the extrusion and friction process, this bilayer suffers from an opposing force from nanomaterials and causes it to destroy the bilayer mechanically.[263] The shape of nanorod and nanofibers with a tiny size can be helpful in breaking.[264] Furthermore, the pore size of the peptidoglycan layer is 2 nm, which can allow ROS species to pass.[265] After ROS penetrates the cell membrane by different pathways, the active species move forward to damage DNA and plasmid.

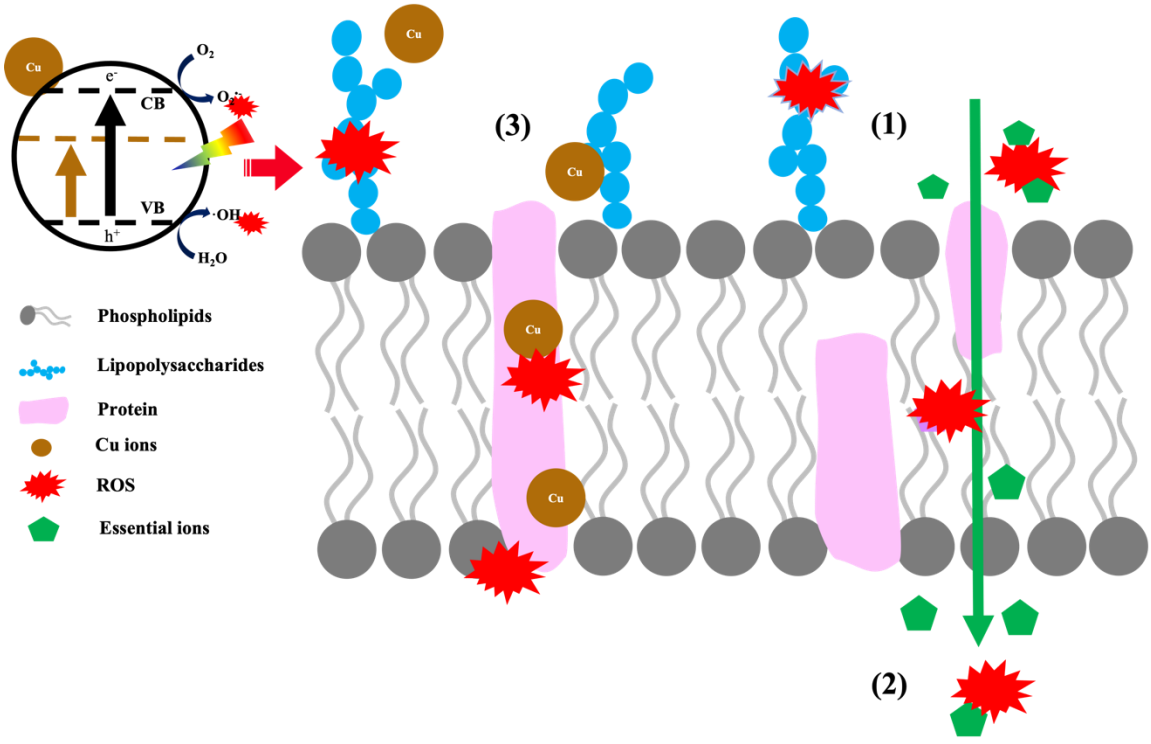

Figure 5.1. Cell membrane structural composition and proposed mechanism in the gram-negative bacteria including, (1) reaction of ROS with LPS, (2) transport of ROS into the cell during Na^+ and K^+ ion conduction, and (3) metal ions such as Cu ions passing through porins.

Oxidative Stress Response in E. coli

ROS are critical components implicated in oxidative disruption of protein, DNA, and lipid molecules of *E. coli*.[259] It is also formed in a wide range of biochemical and physiological processes.[266] Aerobic bacteria intake molecular oxygen for maintaining normal respiration or oxidizing the nutrients to obtain energy.[266,267] During this process, the cell produces ROS such as hydrogen peroxide (H_2O_2), •OH and $O_2^{\bullet-}$ that are by-products of oxygen.[267] When a cell endures from an external stimulus such as high light intensity.[267–269] UV or ionizing radiation, it causes oxidative stress that increases the

concentration of ROS to a concentration higher than what a living cell can defend.[270] Visible light in the blue region (400 and 480 nm) can also cause oxidative stress in *E. coli*.[271]

The Production of ROS from Photocatalytic Disinfection Process on E. coli

The photocatalytic disinfection efficiency of TiO_2 mainly depends on the amount of ROS generation.[272] The electrons and holes generated after the photoexcitation process can react with oxygen and water molecules to generate a subset of free radicals that are derived from molecular oxygen.[273] Bacteria have protective proteins to counter ROS damage.[274] However, with ROS accumulation, the bacterial will undergo cell death due to continuously ROS stimulated biochemical reactions.[275–280] Many studies have reported that TiO_2 photocatalysts can form ROS, including •OH, $O_2^{\bullet-}$ and $^1O_2$ during the UV irradiation process.[281] The ROS generation process and the equation are similar to the photodegradation process in Chapter 4, section 4.1.2. These types of ROS can cause dye degradation and also oxidative stress to *E. coli* cells.[282]

•OH is a strong oxidant and most detrimental to pathogens.[273] This active species generated in the VB can attack almost all the parts of bacteria, including cell membrane, ribosomes and DNA, by bonding and reacting with the lipid, protein, of some essential ions from these structures.[283,284] However, •OH has the shortest lifetime of approximately 10^{-9} seconds and diffusion length (can only diffuse in the cell near the species within five molecular diameters (~ 0.5 μm).[285,286] This disinfection by •OH may be limited by mass transfer through the cell wall or cell membrane.[287] Compared to •OH, $O_2^{\bullet-}$ have a relatively longer lifetime of approximately 10^{-6} seconds.[283,288] Due to $O_2^{\bullet-}$ having a

negative charge, they will be rejected by the LPS on the outside of the cell, thus preventing direct damage to inner cell structures. $O_2^{\bullet-}$ is not a stable radical and can further oxidize with holes or •OH to generate $^1O_2$.[289,290] $^1O_2$ radicals can oxidate membrane or lipid, resulting in damage to the membrane structure.[289,291] Because *E. coli* have no corresponding antioxidation enzymes for $^1O_2$, the cell is more sensitive and selective for $^1O_2$ damage.[292] Another advantage is that $^1O_2$ has a longer lifetime of 3–5 μs and a longer diffusion pathlength of 1 μm.[272]

5.2. Experimental Methods

Escherichia coli, O157:H7 strains (E. *coli*), Luria Bertani (LB) broth, Tryptic soy (TS) agar, sodium chloride (NaCl, 99%), ethylenediaminetetraacetic acid (EDTA), copper chloride ($CuCl_2$, 98%), hydrogen peroxide solution (30%), dimethyl sulfoxide (DMSO), 3,3',5,5'-tetramethylbenzidine (TMB), 2-(N-Morpholino), ethanesulfonic acid, and 4-morpholineethanesulfonic acid (MES) monohydrate were purchased from Sigma Aldrich. 0.5 Polymer McFarland Standard was purchased from Thermo Fisher Scientific. Ethanol (90%) and hydrochloric acid (HCl, 37%) solutions were purchased from Fisher Scientific. All reagents were used as received without further purification. Nano-pure water was obtained from a Thermo Scientific Barnstead Ultrapure Water Purification System.

5.2.1. Material Synthesis

All $TiCu_xO_2$ nanomaterials were prepared as discussed in section 3.2

5.2.2. Photocatalytic Antibacterial Experiment

E. coli strains were maintained with a weekly subculture on TS agar medium. Before the antibacterial experiment, *E. coli* were aerobically incubated at 37 ± 0.1 °C for 24 h in the LB broth. *E. coli* from the overnight culture were harvested by centrifugation at 3500 rpm for 5 min. The *E. coli* was then resuspended in saline solution (0.85%, pH=7) and again centrifuged at 3500 rpm for 5 min to obtain pure strains. Finally, *E. coli* was resuspended in saline solution. The turbidity of *E. coli* cell suspension was measured at 600 nm using a FLUOstar Omega Microplate Reader and adjusted to an optical density of OD600=0.1, which corresponded to approximately 8×10^7 colony-forming units per millilitre (CFU/mL).

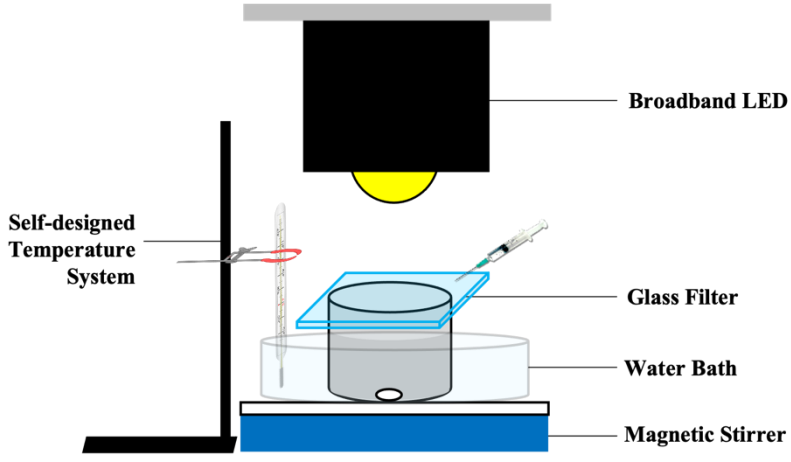

Figure 5.2. The schematic diagram of the photocatalytic antibacterial experimental set up.

The schematic diagram of the antibacterial experiment reactor is shown in **Figure 5.2**. A 200 mL Pyrex® crystallizing dish was used as the reaction vessel. First, 197.5 mL of sterilized saline (0.85%, pH=7) was added to the beaker. Then, 200 mg of the

catalyst and 2.5 mL of the *E. coli* solution were added to the crystallizing dish successively. The final concentration of the catalyst and microorganisms were 1 mg/mL and $1x10^6$ CFU /mL, respectively. The mixture was placed on a magnetic stirrer to keep the catalyst well dispersed during the experiment. The total irradiation time was 3 h. The mixture was irradiated with a 1000W LED lamp equipped with a UV cut-off filter ($\lambda > 400nm$). The light intensity was 100 mW cm^{-2} and measured by a PM100USB Power Detector with Standard Photodiode Sensors. The whole system was performed in Purifier Logic+ Class II, Type A2 biosafety cabinets. The experiments were performed at room temperature and neutral pH. The solution temperature was measured by a self-designed temperature system, which maintained it between 25 and 28 °C during whole experiment. After the crystallizing dish was placed on the magnetic stirrer and the LED was switched on, the sample solution (30 uL) was collected at 20 min intervals and spread uniformly on the TS agar plate. Finally, the plates were incubated at 37 °C for 24 h. The antibacterial efficiency was evaluated by counting the *E. coli* colonies on the plate. The existence of bacteria was calculated using Chick's model:

$$E = \log N_0 - \log N_t = -\log (N_t / N_0) \qquad \text{Eq. 5.1}$$

where E is the antibacterial efficiency, t is the irradiation time, N_0 represents the initial number of colonies, and N_t represents the number of *E. coli* in each time interval.

Each experiment was conducted in triplicates to obtain the mean and standard error. All the samples were treated for microorganism assay. All equipment was sterilized in autoclaved at 121 °C for 30 min before testing.

5.2.3. The Effect of Cu Species on Photocatalytic Antibacterial Performance

2 mM EDTA was added to the photocatalytic antibacterial system to inhibit Cu redox activity. This test was conducted under the same antibacterial experimental condition as mentioned above. If the antibacterial efficiency of photocatalysts were decreased considerably with this chelating agent, it would be considered that Cu species was mainly responsible for the antibacterial activity.

5.2.4. Detection of Cu ions Leaching in the Aquatic Condition by Colorimetric Assay

$CuCl_2$ standard solutions with different concentrations (10, 5, 2.5, 1.25, 0.625, 0.313, and 0.165 uM) were added to the MES buffer (10 mM, pH = 5.5). After incubating for 10 min, TMB (500 uM), NaCl (100 mM) and H_2O_2 (100 mM) were added to it. The TMB catalysts in the presence of Cl^- and H_2O_2 produce blue oxidized products. The absorbance of the blue products at 652 nm was monitored after 30 min using FLUOstar Omega Microplate Reader. To relate the level of Cu ions in the NaCl-TMB-H_2O_2 system to the absorbance of the blue oxidized products, a calibration curve of Cu ions concentration vs absorbance was elaborated. The standard curve presented a linear regression equation (Eq. 5.2) and a coefficient of determination (R^2) of 0.9955.

$$A = 0.2563C+0.1912 \qquad \text{Eq. 5.2}$$

where A is the absorbance of blue products and C is the concentration of Cu ions in 1 mg/mL.

Cu ions in 10,000 ppm $wTiCu_xO_2$ NPs were measured using the standard addition method. The prepared NPs (200 mg) were dispersed in nanopure water (200 mL)

and sonicated for 30 min. The NPs were filtered through a 0.45 uM Teflon filter before analysis. The prepared Cu ions solution was added to the NaCl-TMB-H_2O_2 system. The absorbance of the blue products at 652 nm was monitored after 30 min using FLUOstar Omega Microplate Reader. The concentration of Cu ions was measured by the above calibration curve. All experiments were performed at room temperature in triplicate.

5.2.5. The Antibacterial Effects of Cu Species in Matrix and Surface of TiO_2

The excess and unstable amount of copper species in 10,000 ppm w$TiCu_xO_2$ NPs was removed by HCl treatment. After calcination, 10,000 ppm Cu-doped w$TiCu_xO_2$ catalyst (1000 mg) was added to an aqueous HCl solution (200 mL, 1 M) and stirred at 400 rpm for 10 h at room temperature. After the treatment, the stable Cu species in TiO_2 matrix remained while the unstable species were removed. The final NPs were collected by suction filtration and washed with 500 mL of distilled water, then dried overnight in an oven at 100 °C.

5.2.6. Materials Characterization

Powder XRD, SEM, TEM, HRTEM, XPS, and UV-vis were performed as discussed as in Chapters 2 and 3.

5.3. Result and Discussion

The effect of Cu doping on the antibacterial activity against *E. coli* was studied using both wTiO_2 and bTiO_2 NPs under visible light and dark conditions. Under the dark conditions (**Figure 5.3**), no antibacterial activity was observed for any of the TiO_2 NPs indicating the antibacterial activity only occured under illumination.

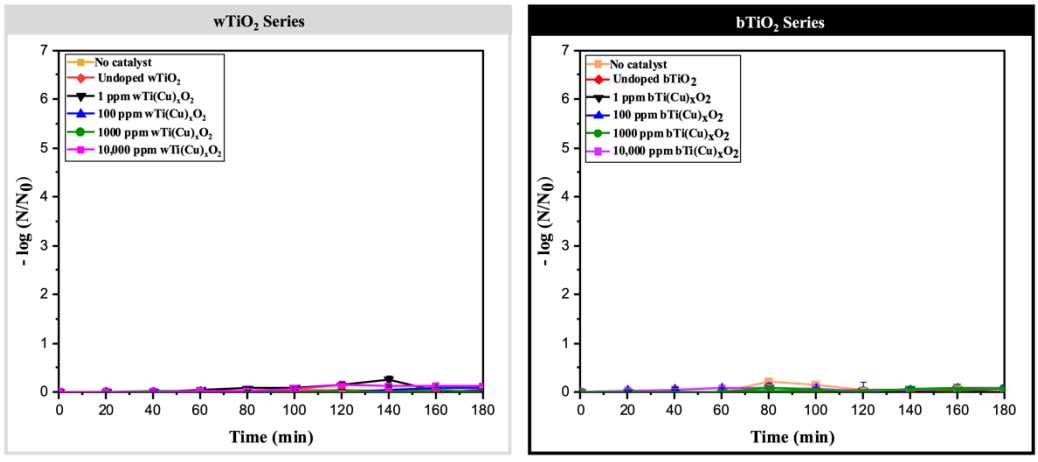

Figure 5.3. Antibacterial performance of white and black TiO_2 catalysts in the dark with varying Cu doping concentration.

Figure 5.4 shows antibacterial properties of the TiO_2 catalysts under illumination. Undoped $wTiO_2$ and 1 ppm $wTiCu_xO_2$ NPs showed minimum antibacterial activity. This is likely due to low visible light absorption, increased charge recombination, or low concentration of ROS production or combination of these. Increasing the Cu concentration, showed higher disinfection under light irradiation. The 1000 ppm $wTiCu_xO_2$ catalyst exhibited a 1.24-log reduction of viable bacteria after 180 min under visible light irradiation. However, the 100 ppm $wTiCu_xO_2$ NPs had a higher activity with 2.75 log reduction of bacteria despite lower Cu amounts. As shown in the RhB dye degradation experiments, this catalyst generated ROS species which likely cause oxidative stress in bacteria. It is possible for 1000 ppm sample to have a lower ROS concentration but enough Cu ions to observe some antibacterial activity. Among all the catalysts, the 10,000 ppm $wTiCu_xO_2$ catalyst showed the highest antibacterial activity despite its low

photocatalytic dye degradation performance. After 60 min irradiation, the *E. coli* can be removed 99.99% using the 10,000 ppm $wTiCu_xO_2$ catalyst. Another thing to note is the decrease in survivability of microorganisms without any photocatalyst. This likely occurs due to the high light intensity resulting in the increased amount of ROS from *E. coli* to a level over the cell defence capacity. The inhibition of *E. coli* was almost zero under irradiation with undoped $wTiO_2$ and 1 ppm $TiCu_xO_2$ catalysts because the NPs can adsorb on the *E. coli* surface and minimize the direct light absorbed by the microorganisms.

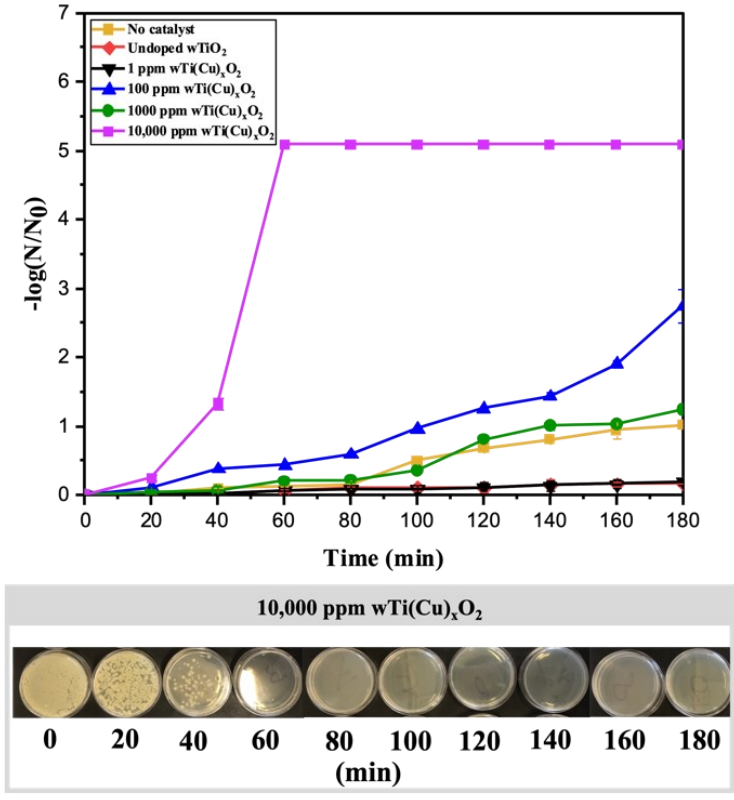

Figure 5.4. Antibacterial performance of undoped $wTiO_2$ and $wTiCu_xO_2$ catalysts under illumination with varying Cu doping concentration.

Figure 5.5 shows the antibacterial performance of all black catalysts. These catalysts did not show any significant antibacterial activity despite the high RhB degradation capacity seen in Chapter 4. The low disinfection activity can be ascribed to the low ROS amount generated during the photocatalytic process demonstrated with scavenger experiments and loss of Cu ions during the hydrogenation as discussed in Chapters 3 and 4. The photocatalytic dye degradation efficiency of black catalysts mainly depended on the active sites composed of Ti^{3+} defects and OVs that allowed the adsorption of dye and were not associated with ROS.[293] Bacterial cells do not have the proper anchoring groups to bind to these defects.

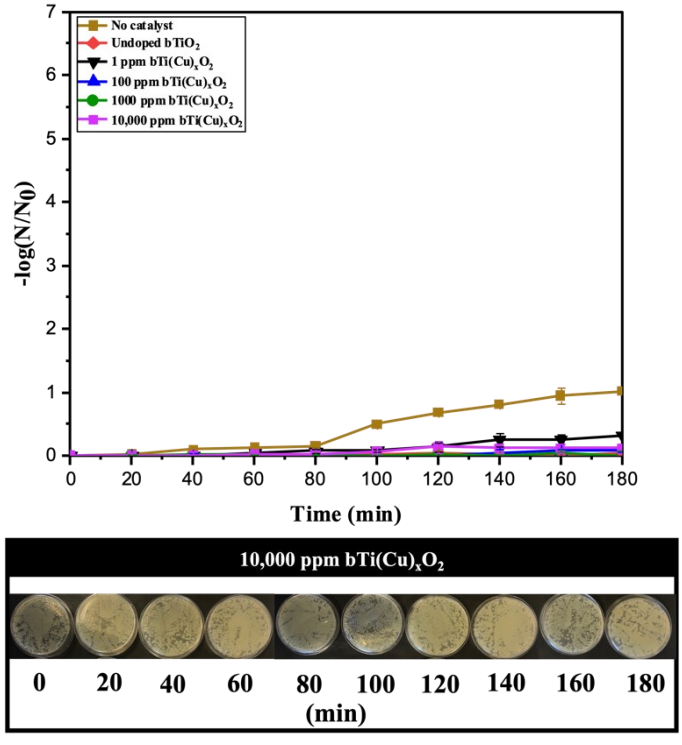

Figure 5.5. Antibacterial performance of undoped $bTiO_2$ and $bTiCu_xO_2$ catalysts under illumination with varying Cu doping concentration.

As the dye degradation experiments already demonstrated poor activity for 10,000 ppm wTiCu$_x$O$_2$ catalyst, ROS is not likely the dominant mechanism for the antibacterial activity. However, the high concentration of Cu ions can either leach out of the NPs and into the cell leading to bacterial cell death or participate in secondary reactions that can have deleterious effect on cells. To test the role of Cu ions, chelating agent was added to the reaction where it can bind to the metal ions and prevent it from participating in the antimicrobial reactions. EDTA is a type of metal chelator that can efficiently chelate Cu^{2+} ions on the surface of TiO_2 NPs.[294] The different Cu species have various capacities for the inhibition of *E. coli*. EDTA chelator is an indicator to identify which Cu species is responsible for antibacterial performance. As shown in **Figure 5.6**, adding EDTA significantly altered the antibacterial performance, essentially rendering the catalyst ineffective. This suggests that the Cu^{2+} ions are responsible for the high antibacterial activity observed in 10,000 ppm wTiCu$_x$O$_2$ NPs.

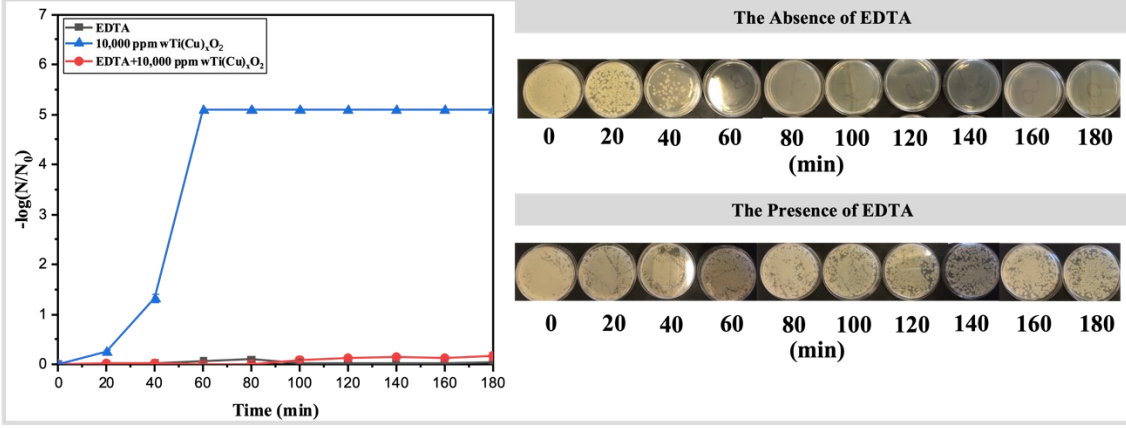

Figure 5.6. The antibacterial performance of 10,000 ppm Cu wTiCu$_x$O$_2$ NPs in the presence and absence of EDTA.

Since the 10,000 ppm wTiCu$_x$O$_2$ catalyst cannot inactivate *E. coli* in a dark environment, it was inferred that Cu^{2+} is not the direct species leading to cell death. *E. coli* is an aerobic bacteria and ROS, including H_2O_2, is released as metabolites through autoxidation of redox enzymes[295] under irradiation.[296,297] The Cu^{2+} ions and H_2O_2 can undergo Fenton-like reactions to generate •OOH (Eq. 5.3).[298] •OOH is also a type of ROS which can damage bacterial cell or further react with surrounding O_2 to form H_2O_2 (Eq. 5.4).[299] In addition, TiO_2 can be excited under irradiation to form election-hole pairs (Eq. 5.5).[80,300] The electrons can react with Cu^{2+} to form Cu^+ (Eq. 5.6), which also can be toxic species to bacteria cells or further react with excess H_2O_2 to form Cu^{2+} and highly active •OH (Eq. 5.7).[299]

$$Cu^{2+} + H_2O_2 \rightarrow Cu^+ + \bullet OOH + H^+ \quad \text{(Eq. 5.3)}$$

$$2\ \bullet OOH \rightarrow H_2O_2 + O_2 \quad \text{(Eq. 5.4)}$$

$$\text{Cu-}TiO_2 + h\nu \rightarrow e^-_{CB} + h^+_{VB} \quad \text{(Eq. 5.5)}$$

$$Cu^{2+} + e^- \rightarrow Cu^+ \quad \text{(Eq. 5.6)}$$

$$Cu^+ + H_2O_2 \rightarrow Cu^{2+} + \bullet OH + OH^- \quad \text{(Eq. 5.7)}$$

Therefore, two factors can probably cause the enhancement of photocatalytic antibacterial reactions. One is the leaching of Cu ions from the NPs and reacting with H_2O_2 produced from oxidative stress to form more ROS and toxic Cu^+ ions (Eq. 5.3 and 5.4). Another is due to the photocatalytic activity of TiO_2 in combination with Cu ions to form ROS and Cu^+ ions (Eq. 5.5 and 5.6). The role of free Cu^{2+} ions was investigated using the supernatant of 10,000 ppm wTiCu$_x$O$_2$ NPs and a Cu^{2+} salt solution. As shown in **Figure**

5.7, the supernatant of 10,000 ppm wTiCu$_x$O$_2$ catalyst showed lower antibacterial performance compared to the original sample. The concentration of Cu^{2+} ions in the supernatant was determined to be around 3.7 uM as determined by the colorimetric assay in the TMB-H_2O_2-NaCl system. $CuCl_2$ solution with a concentration of 10,000 mg/L, corresponding to Cu synthesis concentration in 10,000 ppm wTiCu$_x$O$_2$ NPs was added to the reaction. The rate of antibacterial activity is lower than 10,000 ppm wTiCu$_x$O$_2$ NPs but higher than the supernatants of 10,000 ppm wTiCu$_x$O$_2$ NPs. It should be noted that the final concentration of Cu ions in the wTiCu$_x$O$_2$ NPs is likely lower than 10,000 ppm. So, despite the high concentration of $CuCl_2$ solution, its activity is lower. This indicates that the antibacterial activity is caused by a synergetic effect between H_2O_2 formation by cell oxidative stress under a high-intensity light and the photocatalytic capacity of 10,000 ppm wTiCu$_x$O$_2$ NPs not merely due to Cu^{2+} ions leaching from NPs.[255]

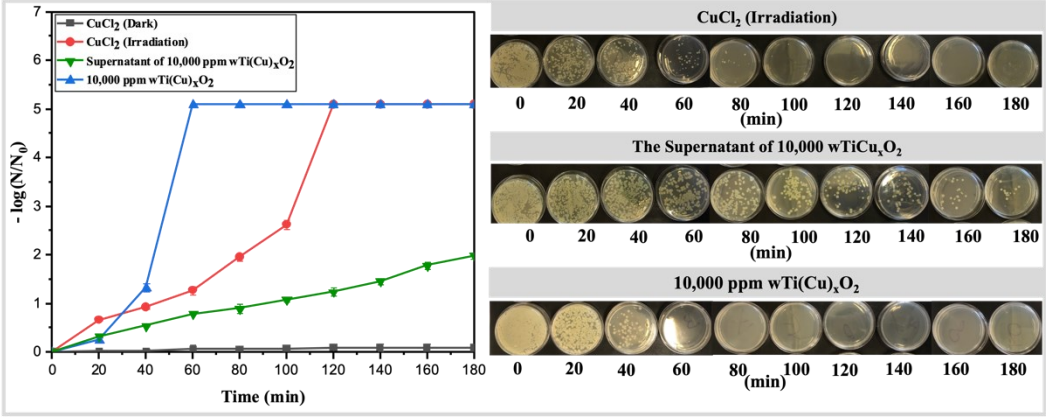

Figure 5.7. The antibacterial performance in the presence of supernatant of 10,000 ppm wTiCu$_x$O$_2$ NPs, pure $CuCl_2$ solution, and 10,000 ppm wTiCu$_x$O$_2$ NPs.

To investigate the role of Cu present inside the particle, the photocatalytic antibacterial activity of HCl treated 10,000 ppm $wTiCu_xO_2$ NPs was investigated. As presented in **Figure 5.8**, the HCl-treated catalyst showed a lower antibacterial performance, and 99.99% *E. coli* removed by the HCl-treated catalyst took longer than 20 mins. The HCl treatment likely removes surface CuO that participate in Fenton like reactions thus slowing the rate. However, the CuO present inside the NPs still play a critical role antibacterial efficiency.

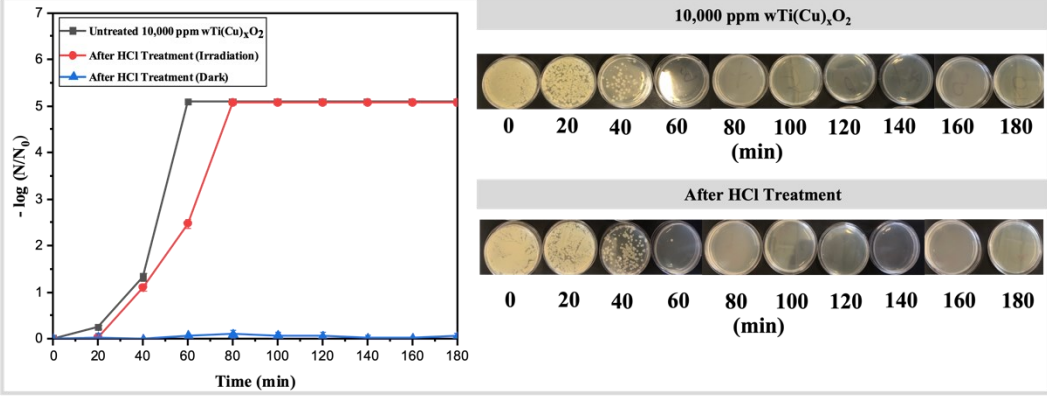

Figure 5.8. The antibacterial effect of 10,000 ppm $wTiCu_xO_2$ NPs before and after HCl treatment.

Typically, it is accepted that the TiO_2 photocatalysts under light irradiation of a suitable wavelength can generate electron-hole pairs causing redox reactions resulting in the inactivation of harmful microbes. However, in this study, $wTiCu_xO_2$ catalyst exhibited a more complex disinfection process. The antibacterial mechanism basically depends on the concentration of Cu in TiO_2. Firstly, with 100 ppm, $wTiCu_xO_2$, the enhancement of

antibacterial activity is due to ROS formation. In Chapter 4, the type of ROS generated from 100 ppm $wTiCu_xO_2$ NPs *via* scavenger test in RhB dye system were •OH and $O_2^{\bullet-}$. These ROS could disrupt proteins and lipids in the cell membrane and cell DNA resulting in cell apoptosis in *E. coli*. However, the photocatalytic antibacterial performance of 1000 ppm $wTiCu_xO_2$ catalyst was not obvious. It likely forms lower amounts of ROS (as evidenced from lower RhB dye degradation activity) that do not exceed the level of antioxidant defences of the bacteria. In addition, it could also have inefficient Cu^{2+} ions on the surface to promote Fenton-like reactions. The combination of these factors leads to lower antimicrobial activity.

The high concentration of Cu doping in TiO_2 played a crucial role in photocatalytic disinfection. During irradiation, 10,000 ppm $wTiCu_xO_2$ catalyst reacts with H_2O_2 from *E. coli* cell to form ROS such as •OOH and •OH by Fenton-like reactions resulting in cell apoptosis. An excellent antibacterial performance was caused by the synergistic action of new ROS, free Cu ions, and matrix Cu species. The possible antibacterial process is summarized in **Figure 5.9**.

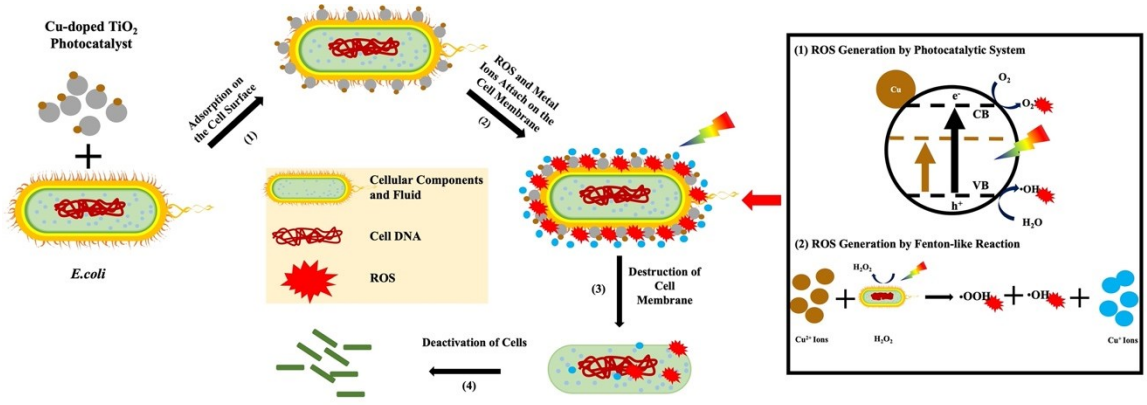

Figure 5.8 The possible mechanism of photocatalytic antibacterial activity

Figure 5.9. The possible mechanism of photocatalytic antibacterial activity with $wTiCu_xO_2$ NPs.

5.4. Conclusion

In summary, the antibacterial activity of white and black TiO_2 doped with Cu was explored. The $bTiCu_xO_2$ catalysts did not exhibit any disinfection performance due to inadequate ROS generation during the photocatalytic process. For $wTiCu_xO_2$ catalysts, the highest activity was observed for 10,000 ppm $wTiCu_xO_2$ NPs. Mechanistic studies were performed to understand the microbial growth inhibition pathways. It was determined that the combination of light, free Cu^{2+} ions, and ROS lead to synergistic antimicrobial activity.

CHAPTER 6. Conclusions and Future Work

6.1. Conclusions

This thesis focused on the synthesis and photocatalytic application of $TiCu_xO_2$ nanostructures. The solvothermal method was used to make undoped and 1, 100, 1000, and 10,000 ppm $wTiCu_xO_2$ NPs. These concentrations of Cu were added to the synthesis mixture in hope that they get completely incorporated within TiO_2. However, the exact concentration of Cu in these NPs needs to be determined in the future. This synthetic method yielded anatase phase $wTiO_2$ with particle sizes ranging between 18 to 34 nm. The undoped and 1 ppm Cu-doped samples were found to be very similar to each other in size, composition, crystallinity, and optical properties. The 100 ppm $wTiCu_xO_2$ catalyst showed uniform distribution of Cu ions within the TiO_2 lattice based on HR-TEM, elemental mapping, and optical properties. The 1000 and 10,000 ppm $TiCu_xO_2$ NPs exhibited phase segregation that resulted in $yCuO/TiCu_{x-y}O_2$ hybrid composite. Due to the formation of CuO grains, these had much higher absorption in the visible region.

The various $wTiO_2$ NPs were converted to hydrogenated $bTiO_2$ samples by reacting them with $NaBH_4$ at high temperatures. The hydride salt decomposes in-situ to form H_2 that reacts with TiO_2 and converts surface Ti^{4+} ions to Ti^{3+} and forms high concentration of OVs. A slight increase in particle size was observed post $NaBH_4$ treatment which could be due to sintering. The optical properties showed absorption in the visible region for all the samples. However, the magnitude of this absorption varied with Cu doping. Similar to the white series, undoped $bTiO_2$ and 1 ppm $bTiCu_xO_2$ samples had very similar properties. Elemental mapping showed that the uniform distribution of Cu ions was

retained post hydrogenation in the 100 ppm $bTiCu_xO_2$ NPs. Both 1000 and 10,000 ppm $bTiCu_xO_2$ samples showed loss of surface Cu as determined from XPS studies. It is hypothesized that the surface Cu ions undergo out diffusion during the thermal treatment and are washed away during the HCl wash. Further, the elemental mapping analysis performed on 10,000 ppm $bTiCu_xO_2$ catalyst showed that the CuO grains underwent growth and formed fewer but larger CuO grains.

The photocatalytic degradation of RhB was explored with all the synthesized catalysts. Among the non-hydrogenated samples, 100 ppm $wTiCu_xO_2$ catalyst performed the best. Experiments performed with various scavengers showed that degradation occurred due to ROS formation. The dominant ROS species responsible for RhB degradation were found to be •OH, $O_2^{\bullet-}$ and holes . Among the hydrogenated series, 100 ppm $bTiCu_xO_2$ catalyst was found to be the best performing. The degradation mechanism was different for this sample, and it was found that ROS did not play a significant role. It was hypothesized that the OVs and Ti^{3+} ions provided binding sites for RhB and the degradation occurs through direct transfer of electron and holes to the dye molecule.

Photocatalytic antibacterial activity against *E. coli* was also explored with all the synthesized catalysts. The undoped $bTiO_2$ and all the $bTiCu_xO_2$ catalysts showed poor antibacterial activity. Among the non-hydrogenated samples, 10,000 ppm $wTiCu_xO_2$ catalyst had the best antibacterial activity. The activity was found to be due to synergistic effects of leached Cu^{2+} ions, oxidative stress, and ROS formation by the catalyst.

6.2. Future Work

6.2.1. Further Understanding of the Mechanism of Photocatalytic and Antibacterial Activity

Further studies can be conducted to confirm the degradation mechanism of 100 ppm b$TiCu_xO_2$ catalyst. Organic molecules that bind strongly to the defect states would have higher degradation rates compared to the weakly coordinated ones. Future studies exploring different organic substrates with varying adsorption abilities can help confirm this mechanism. It should also focus on understanding the properties of these surface defects, including the adsorption capacity, density, concentration, and charge trapping. In Chapter 5, the antibacterial experiment found that 10,000 ppm w$TiCu_xO_2$ catalyst had the best inhibition of *E. coli* growth. The doping concentration of catalyst in the experiment was 10 mg/mL. The high dosage of catalyst will pose a difficulty for recycling and sedimentation. The excessive free Cu ions released to the water system will pose a threat to the aquatic environment and be hard to remove.[301] Therefore, in the future, the antibacterial experiment could be repeated with different catalyst dosages to point out the minimum inhibition concentration, which will be important to optimize the reaction condition.

The EDTA experiment determined the Cu species possibly is crucial to kill the *E. coli*, but EDTA also can be a hole scavenger.[302] It is difficult to identify which one is the most important species to impact *E. coli* growth, between ROS and Cu species, or the antibacterial efficiency relies on synergistic effects *via* these two species. Future work aims at finding out the type of ROS to identify which is the most toxic species to *E. coli*. In addition, measuring the concentration of H_2O_2 from bacteria respiratory action will also

be a good point to understand the photocatalytic activity of high Cu content on TiO_2 surface.

6.2.2. Enhancement of Photocatalytic Antibacterial Activity

The photocatalytic disinfection kinetic has been studied for model bacteria *E. coli* and also provided some insight into photocatalytic antibacterial mechanism in Chapter 5. As mentioned above, the precise mechanism was still debatable, but the role of produced ROS and Cu toxicity is an essential step for microbial disinfection. The lifetime of ROS is short. If the NPs are not very close and adhere to the bacteria surface, it is hard to achieve cell inactivation *via* disruption of the LPS layer, cytoplasmic membrane and phospholipid layer in the outer cell membrane resulting in decreasing antibacterial efficiency. The adsorption capacity of NPs should be considered and detected for understanding the entry pathway of NPs into the bacterial cell in the future. Many studies figured out the NPs adhesion on the bacteria depend on non-specific and reversible physical adhesion. The adhesion mainly depends on the surface physical properties of NPs, including surface hydrophobicity, surface charge, surface charge potential, roughness, surface area, pore structure and particle size.[303] Therefore, the photocatalytic activity can be tailored by altering textural properties. Future work also aims to synthesizing fiber-like materials based on $wTiCu_xO_2$ and $bTiCu_xO_2$ catalysts. A larger surface area can increase the light absorption, surface photoredox reaction, bacteria adhesion, and disruption of the cell wall structure. In addition, compared to NPs structures, fiber-like materials are easier to recycle and sediment, which significantly promotes the industrial application for long-term wastewater treatment.[304]

REFERENCES

(1) Afroz, R.; Masud, M. M.; Akhtar, R.; Duasa, J. B. Water Pollution: Challenges and Future Direction for Water Resource Management Policies in Malaysia. *Environment and Urbanization ASIA* **2014**, *5* (1), 63–81.

(2) Abo, M.; Rashid, H.; Zulfikar, S.; Bhutto, A. Urbanization and Its Effects on Water Resources: An Exploratory Analysis. *content.iospress.com* **2018**.

(3) Mouele, E. S. M.; Tijani, J. O.; Fatoba, O. O.; Petrik, L. F. Degradation of Organic Pollutants and Microorganisms from Wastewater Using Different Dielectric Barrier Discharge Configurations—a Critical Review. *Environmental Science and Pollution Research* **2015**, *22* (23), 18345–18362.

(4) Rashmi, I.; Roy, T.; Kartika, K. S.; Pal, R.; Coumar, V.; Kala, S.; Shinoji, K. C. Organic and Inorganic Fertilizer Contaminants in Agriculture: Impact on Soil and Water Resources. *Contaminants in Agriculture: Sources, Impacts and Management* **2020**, 3–41.

(5) Hunter, P. R.; MacDonald, A. M.; Carter, R. C. Water Supply and Health. *PLoS Med* **2010**, *7* (11), e1000361.

(6) M González-Eguino - Renewable and sustainable energy; 2015, undefined. Energy Poverty: An Overview. *Elsevier* **2015**, 377–385.

(7) Zularisam, A. W.; Ismail, A. F.; Salim, R. Behaviours of Natural Organic Matter in Membrane Filtration for Surface Water Treatment — a Review. *Desalination* **2006**, *194* (1–3), 211–231.

(8) Ali, I.; Gupta, V. K. Advances in Water Treatment by Adsorption Technology. *Nature Protocols 2007 1:6* **2007**, *1* (6), 2661–2667.

(9) Strathmann, H. Chapter 6 Ion-Exchange Membrane Processes in Water Treatment. *Sustainability Science and Engineering* **2010**, *2* (C), 141–199.

(10) Robinson, T.; McMullan, G.; Marchant, R.; Nigam, P. Remediation of Dyes in Textile Effluent: A Critical Review on Current Treatment Technologies with a Proposed Alternative. *Bioresour Technol,* **2001**, *77* (3), 247–255.

(11) Wei, Y.; van Houten, R. T.; Borger, A. R.; Eikelboom, D. H.; Fan, Y. Minimization of Excess Sludge Production for Biological Wastewater Treatment. *Water Res* **2003**, *37* (18), 4453–4467.

(12) Garrido-Cardenas, J. A.; Esteban-García, B.; Agüera, A.; Sánchez-Pérez, J. A.; Manzano-Agugliaro, F. Wastewater Treatment by Advanced Oxidation Process and

Their Worldwide Research Trends. *International Journal of Environmental Research and Public Health,* **2019**, *17* (1), 170.

(13) Saravanan, A.; Senthil Kumar, P.; Jeevanantham, S.; Karishma, S.; Tajsabreen, B.; Yaashikaa, P. R.; Reshma, B. Effective Water/Wastewater Treatment Methodologies for Toxic Pollutants Removal: Processes and Applications towards Sustainable Development. *Chemosphere* **2021**, *280*, 130595.

(14) Mahamuni, N. N., & Adewuyi, Y. G. Advanced oxidation processes (AOPs) involving ultrasound for wastewater treatment: a review with emphasis on cost estimation. *Ultrasonics sonochemistry*, **2010**. *17*(6), 990-1003.

(15) Munter, R. Advanced oxidation processes–status and prospects. *Proc. Estonian Acad. Sci. Chem*. **2001**, *50*(2), 59-80.

(16) Wang, J. L.; Le, &; Xu, J.; Xu, L. J.; Wang, J. L.; Xu, L. J. Advanced Oxidation Processes for Wastewater Treatment: Formation of Hydroxyl Radical and Application. **2011**, *42* (3), 251–325.

(17) Litter, M. I. Introduction to Photochemical Advanced Oxidation Processes for Water Treatment. *Environmental Photochemistry Part II* **2005**, 325–366.

(18) Liu, Y.; He, X.; Duan, X.; Fu, Y.; Fatta-Kassinos, D.; Dionysiou, D. D. Significant Role of UV and Carbonate Radical on the Degradation of Oxytetracycline in UV-AOPs: Kinetics and Mechanism. *Water Res.* **2016**, *95*, 195–204.

(19) Acero, J. L.; von Gunten, U. Characterization of Oxidation Processes: Ozonation and the AOP O_3/H_2O_2. *J Am Water Works Assoc.* **2001**, *93* (10), 90–100.

(20) Poblete, R.; Oller, I.; Maldonado, M. I.; Cortes, E. Improved Landfill Leachate Quality Using Ozone, UV Solar Radiation, Hydrogen Peroxide, Persulfate and Adsorption Processes. *J Environ Manage* **2019**, *232*, 45–51.

(21) Ali, H.; Gulzar, O.; Karanth, K. V.; Hassan, M. A.; Zeeshan, M. Experimental Analysis of Portable Optical Solar Water Heater. *Lecture Notes in Mechanical Engineering* **2021**, 925–937.

(22) Comninellis, C.; Kapalka, A.; Malato, S.; Parsons, S. A.; Poulios, I.; Mantzavinos, D. Advanced Oxidation Processes for Water Treatment: Advances and Trends for R&D. *Journal of Chemical Technology & Biotechnology* **2008**, *83* (6), 769–776.

(23) Du, H.; Xie, Y.; Wang, J. Microplastic Degradation Methods and Corresponding Degradation Mechanism: Research Status and Future Perspectives. *J Hazard Mater.* **2021**, *418*, 126377.

(24) Singh, J.; Kumar, V.; Kim, K. H.; Rawat, M. Biogenic Synthesis of Copper Oxide Nanoparticles Using Plant Extract and Its Prodigious Potential for Photocatalytic Degradation of Dyes. *Environ Res* **2019**, *177*, 108569.

(25) Borišev, I.; Borišev, M.; Jović, D.; Župunski, M.; Arsenov, D.; Pajević, S.; Djordjevic, A. Nanotechnology and Remediation of Agrochemicals. *Agrochemicals Detection, Treatment and Remediation* **2020**, 487–533.

(26) Yan, H.; Wang, X.; Yao, M.; Yao, X. Band Structure Design of Semiconductors for Enhanced Photocatalytic Activity: The Case of TiO_2. *Progress in Natural Science: Materials International* **2013**, *23* (4), 402–407.

(27) Smith, A. M.; Nie, S. Semiconductor Nanocrystals: Structure, Properties, and Band Gap Engineering. *Acc Chem Res.* **2010**, *43* (2), 190–200.

(28) Pattanaik, P.; Sahoo, M. K. TiO_2 Photocatalysis: Progress from Fundamentals to Modification Technology. *New pub: Balaban* **2014**, *52* (34–36), 6567–6590.

(29) Tang, J.; Durrant, J. R.; Klug, D. R. Mechanism of Photocatalytic Water Splitting in TiO_2. Reaction of Water with Photoholes, Importance of Charge Carrier Dynamics, and Evidence for Four-Hole Chemistry. *J Am Chem Soc* **2008**, *130* (42), 13885–13891.

(30) Fujishima, A.; Honda, K. Electrochemical Photolysis of Water at a Semiconductor Electrode. *Nature 1972 238:5358* **1972**, *238* (5358), 37–38.

(31) Frank, S. N.; Bard, A. J. Heterogeneous Photocatalytic Oxidation of Cyanide Ion in Aqueous Solutions at TiO_2 Powder. *J Am Chem Soc* **1977**, *99* (1), 303–304.

(32) Samat, M. H.; Ali, A. M. M.; Taib, M. F. M.; Hassan, O. H.; Yahya, M. Z. A. Hubbard U Calculations on Optical Properties of 3d Transition Metal Oxide TiO_2. *Results Phys* **2016**, *6*, 891–896.

(33) Chiarello, G. L.; di Paola, A.; Palmisano, L.; Selli, E. Effect of Titanium Dioxide Crystalline Structure on the Photocatalytic Production of Hydrogen. *Photochemical & Photobiological Sciences 2011 10:3* **2020**, *10* (3), 355–360.

(34) Mo, S. di; Ching, W. Y. Electronic and Optical Properties of Three Phases of Titanium Dioxide: Rutile, Anatase, and Brookite. *Phys Rev B* **1995**, *51* (19), 13023.

(35) Hanaor, D. A. H.; Sorrell, C. C. Review of the Anatase to Rutile Phase Transformation. *Journal of Materials Science 2010 46:4* **2010**, *46* (4), 855–874.

(36) Gupta, S. M.; Tripathi, M. A Review of TiO_2 Nanoparticles. *Chinese Science Bulletin 2011 56:16* **2011**, *56* (16), 1639–1657.

(37) Diebold, U. The Surface Science of Titanium Dioxide. *Surf Sci Rep* **2003**, *48* (5–8), 53–229.

(38) Zerjav, G.; Zizek, K.; Zavasnik, J.; Pintar, A. Brookite vs. Rutile vs. Anatase: What`s behind Their Various Photocatalytic Activities? *J Environ Chem Eng* **2022**, *10* (3), 107722.

(39) Carp, O.; Huisman, C. L.; Reller, A. Photoinduced Reactivity of Titanium Dioxide. *Progress in Solid State Chemistry* **2004**, *32* (1–2), 33–177.

(40) Fujishima, A.; Zhang, X.; Tryk, D. A. TiO_2 Photocatalysis and Related Surface Phenomena. *Surf Sci Rep* **2008**, *63* (12), 515–582.

(41) Smith, S. J.; Stevens, R.; Liu, S.; Li, G.; Navrotsky, A.; Boerio-Goates, J.; Woodfield, B. F. Heat Capacities and Thermodynamic Functions of TiO_2 Anatase and Rutile: Analysis of Phase Stability. *Am Miner* **2009**, *94* (2–3), 236.

(42) Hanaor, D. A. H.; Sorrell, C. C. Review of the Anatase to Rutile Phase Transformation. *Journal of Materials Science 2010 46:4* **2010**, *46* (4), 855–874.

(43) Katal, R.; Masudy-Panah, S.; Tanhaei, M.; Farahani, M. H. D. A.; Jiangyong, H. A Review on the Synthesis of the Various Types of Anatase TiO_2 Facets and Their Applications for Photocatalysis. *Chemical Engineering Journal* **2020**, *384*, 123384.

(44) Kim, W.; Tachikawa, T.; Moon, G.; Majima, T.; Choi, W. Molecular-Level Understanding of the Photocatalytic Activity Difference between Anatase and Rutile Nanoparticles. *Angewandte Chemie* **2014**, *126* (51), 14260–14265.

(45) Choi, Y.; Umebayashi, T.; Yoshikawa, M. Fabrication and Characterization of C-Doped Anatase TiO_2 Photocatalysts. *J Mater Sci* **2004**, *39* (5), 1837–1839.

(46) De Angelis, F.; di Valentin, C.; Fantacci, S.; Vittadini, A.; Selloni, A. Theoretical Studies on Anatase and Less Common TiO_2 Phases: Bulk, Surfaces, and Nanomaterials. **2014**.

(47) Luttrell, T.; Halpegamage, S.; Tao, J.; Kramer, A.; Sutter, E.; Batzill, M. Why Is Anatase a Better Photocatalyst than Rutile? - Model Studies on Epitaxial TiO_2 Films. *Scientific Reports 2014 4:1* **2014**, *4* (1), 1–8.

(48) Wu, W.; Jiang, C.; Roy, V. A. L. Recent Progress in Magnetic Iron Oxide–Semiconductor Composite Nanomaterials as Promising Photocatalysts. *Nanoscale* **2014**, *7* (1), 38–58.

(49) Wang, S.; Yun, J. H.; Luo, B.; Butburee, T.; Peerakiatkhajohn, P.; Thaweesak, S.; Xiao, M.; Wang, L. Recent Progress on Visible Light Responsive Heterojunctions for Photocatalytic Applications. *J Mater Sci Technol* **2017**, *33* (1), 1–22.

(50) Hu, K.; Lei, E.; Zhao, D.; Li, Y.; Zhao, W.; Rong, H. Characteristics and Performance of Rutile/Anatase/Brookite TiO_2 and TiO_2 –$Ti_2O_3(H_2O)_2(C_2O_4)\cdot H_2O$ Multiphase Mixed Crystal for the Catalytic Degradation of Emerging Contaminants. *CrystEngComm* **2020**, *22* (6), 1086–1095.

(51) Wen, Y.; Feng, M.; Zhang, P.; Zhou, H.-C.; Sharma, V. K.; Ma, X. Metal Organic Frameworks (MOFs) as Photocatalysts for the Degradation of Agricultural Pollutants in Water. *ACS ES&T Engineering* **2021**, *1* (5), 804–826.

(52) Lazzeri, M., Vittadini, A., & Selloni, A.. Structure and energetics of stoichiometric TiO_2 anatase surfaces. *Physical Review B*, **2001** *63*(15), 155409.

(53) Pan, J.; Liu, G.; Lu, G. Q.; Cheng, H. M. On the True Photoreactivity Order of {001}, {010}, and {101} Facets of Anatase TiO_2 Crystals. *Angewandte Chemie International Edition* **2011**, *50* (9), 2133–2137.

(54) Diebold, U. The Surface Science of Titanium Dioxide. *Surf Sci Rep* **2003**, *48* (5–8), 53–229.

(55) Deligiannakis, Y. Nanomaterials for Environmental Solar Energy Technologies: Applications & Limitations. *KONA Powder and Particle Journal* **2018**, *35* (35), 14–31.

(56) Zhang, J.; Zhou, P.; Liu, J.; Yu, J. New Understanding of the Difference of Photocatalytic Activity among Anatase, Rutile and Brookite TiO_2. *Physical Chemistry Chemical Physics* **2014**, *16* (38), 20382–20386.

(57) Moser, J. E. Slow Recombination Unveiled. *Nature Materials 2017 16:1* **2016**, *16* (1), 4–6.

(58) Schneider, J.; Matsuoka, M.; Takeuchi, M.; Zhang, J.; Horiuchi, Y.; Anpo, M.; Bahnemann, D. W. Understanding TiO_2 photocatalysis: Mechanisms and Materials. *Chem Rev* **2014**, *114* (19), 9919–9986.

(59) Kandiel, T. A.; Dillert, R.; Robben, L.; Bahnemann, D. W. Photonic Efficiency and Mechanism of Photocatalytic Molecular Hydrogen Production over Platinized Titanium Dioxide from Aqueous Methanol Solutions. *Catal Today* **2011**, *161* (1), 196–201.

(60) Basavarajappa, P. S.; Patil, S. B.; Ganganagappa, N.; Reddy, K. R.; Raghu, A. v.; Reddy, C. V. Recent Progress in Metal-Doped TiO_2, Non-Metal Doped/Codoped TiO_2 and TiO_2 Nanostructured Hybrids for Enhanced Photocatalysis. *Int J Hydrogen Energy* **2020**, *45* (13), 7764–7778.

(61) Yu, J.; Lei, J.; Wang, L.; Zhang, J.; Liu, Y. TiO_2 Inverse Opal Photonic Crystals: Synthesis, Modification, and Applications - A Review. *J Alloys Compd* **2018**, *769*, 740–757.

(62) Mittal, A.; Mari, B.; Sharma, S.; Kumari, V.; Maken, S.; Kumari, K.; Kumar, N. Non-Metal Modified TiO_2: A Step towards Visible Light Photocatalysis. *Journal of Materials Science: Materials in Electronics* **2019**, *30* (4), 3186–3207.

(63) Rehman, S.; Ullah, R.; Butt, A. M.; Gohar, N. D. Strategies of Making TiO_2 and ZnO Visible Light Active. *J Hazard Mater* **2009**, *170* (2–3), 560–569.

(64) Zhang, H.; Chen, G.; Li, Y.; Teng, Y. Electronic Structure and Photocatalytic Properties of Copper-Doped $CaTiO_3$. *Int J Hydrogen Energy* **2010**, *35* (7), 2713–2716.

(65) Liao, C.; Li, Y.; Tjong, S. C. Visible-Light Active Titanium Dioxide Nanomaterials with Bactericidal Properties. *Nanomaterials 2020, Vol. 10, Page 124* **2020**, *10* (1), 124.

(66) Palacios, P.; Sánchez, K.; Conesa, J. C.; Wahnón, P. First Principles Calculation of Isolated Intermediate Bands Formation in a Transition Metal-Doped Chalcopyrite-Type Semiconductor. *physica status solidi (a)* **2006**, *203* (6), 1395–1401.

(67) Yan, Y.; Yu, Y.; Cao, C.; Huang, S.; Yang, Y.; Yang, X.; Cao, Y. Enhanced Photocatalytic Activity of TiO_2-Cu/C with Regulation and Matching of Energy Levels by Carbon and Copper for Photoreduction of CO_2 into CH_4. *CrystEngComm* **2016**, *18* (16), 2956–2964.

(68) Mishra, V.; Warshi, M. K.; Sati, A.; Kumar, A.; Mishra, V.; Sagdeo, A.; Kumar, R.; Sagdeo, P. R. Diffuse Reflectance Spectroscopy: An Effective Tool to Probe the Defect States in Wide Band Gap Semiconducting Materials. *Mater Sci Semicond Process* **2018**, *86*, 151–156.

(69) Geoffroy, G. L., & Gladfelter, W. L.. The designed synthesis of tridecacarbonyldihydridoirondirutheniumosmium and tridecacarbonyldihydridoironrutheniumdiosmium. The first examples of clusters comprised of three different transition metals. *Journal of the American Chemical Society*, **1977**, *99*(1), 304-306

(70) Khan, M. R.; Chuan, T. W.; Yousuf, A.; Chowdhury, M. N. K.; Cheng, C. K. Schottky Barrier and Surface Plasmonic Resonance Phenomena towards the Photocatalytic Reaction: Study of Their Mechanisms to Enhance Photocatalytic Activity. *Catal Sci Technol* **2015**, *5* (5), 2522–2531.

(71) Chakrapani, V. Semiconductor Junctions, Solid-Solid Junctions. *Encyclopedia of Applied Electrochemistry* **2014**, 1882–1893.

(72) Iliev, V.; Tomova, D.; Bilyarska, L.; Eliyas, A.; Petrov, L. Photocatalytic Properties of TiO_2 Modified with Platinum and Silver Nanoparticles in the Degradation of Oxalic Acid in Aqueous Solution. *Appl Catal B* **2006**, *63* (3–4), 266–271.

(73) Rahulan, K. M.; Ganesan, S.; Aruna, P. Synthesis and Optical Limiting Studies of Au-Doped TiO_2 Nanoparticles. *Advances in Natural Sciences: Nanoscience and Nanotechnology* **2011**, *2* (2).

(74) Khairy, M.; Zakaria, W. Effect of Metal-Doping of TiO_2 Nanoparticles on Their Photocatalytic Activities toward Removal of Organic Dyes. *Egyptian Journal of Petroleum* **2014**, *23* (4), 419–426.

(75) Zhang, J.; Fu, D.; Wang, S.; Hao, R.; Xie, Y. Photocatalytic Removal of Chromium (VI) and Sulfite Using Transition Metal (Cu, Fe, Zn) Doped TiO_2 Driven by Visible Light: Feasibility, Mechanism and Kinetics. *Journal of Industrial and Engineering Chemistry* **2019**, *80*, 23–32.

(76) Paola, A. di; Ikeda, S.; Marcì, G.; Ohtani, B.; Palmisano, L. Transition Metal Doped TiO_2: Physical Properties and Photocatalytic Behaviour. *INTERNATIONAL JOURNAL OF PHOTOENERGY* **2001**, *3*.

(77) Liu, B.; Chen, H. M.; Liu, C.; Andrews, S. C.; Hahn, C.; Yang, P. Large-Scale Synthesis of Transition-Metal-Doped TiO_2 Nanowires with Controllable Overpotential. *J Am Chem Soc* **2013**, *135* (27), 9995–9998.

(78) Daghrir, R.; Drogui, P.; Robert, D. Modified TiO_2 for Environmental Photocatalytic Applications: A Review. *Ind Eng Chem Res* **2013**, *52* (10), 3581–3599.

(79) Bhattacharyya, K.; Mane, G. P.; Rane, V.; Tripathi, A. K.; Tyagi, A. K. Selective CO2Photoreduction with Cu-Doped TiO_2 Photocatalyst: Delineating the Crucial Role of Cu-Oxidation State and Oxygen Vacancies. *Journal of Physical Chemistry C* **2021**, *125*.

(80) Wu, B.; Huang, R.; Sahu, M.; Feng, X.; Biswas, P.; Tang, Y. J. Bacterial Responses to Cu-Doped TiO_2 Nanoparticles. *Science of The Total Environment* **2010**, *408* (7), 1755–1758.

(81) Karunakaran, C., Abiramasundari, G., Gomathisankar, P., Manikandan, G., & Anandi, V. Cu-doped TiO_2 nanoparticles for photocatalytic disinfection of bacteria under visible light. *Journal of colloid and interface science*, **2010**. *352*(1), 68-74.

(82) Colón, G.; Maicu, M.; Hidalgo, M. C.; Navío, J. A. Cu-Doped TiO_2 Systems with Improved Photocatalytic Activity. *Appl Catal B* **2006**, *67* (1–2), 41–51.

(83) Liu, Q. M.; Zhou, D. B.; Yamamoto, Y.; Ichino, R.; Okido, M. Preparation of Cu Nanoparticles with $NaBH_4$ by Aqueous Reduction Method. *Transactions of Nonferrous Metals Society of China* **2012**, *22* (1), 117–123.

(84) Xin, B.; Wang, P.; Ding, D.; Liu, J.; Ren, Z.; Fu, H. Effect of Surface Species on Cu-TiO_2 Photocatalytic Activity. *Appl Surf Sci* **2008**, *254* (9), 2569–2574.

(85) Di Paola, A.; Ikeda, S.; Marcì, G.; Ohtani, B.; Palmisano, L. Transition Metal Doped TiO_2: Physical Properties and Photocatalytic Behaviour. *International Journal of Photoenergy* **2002**, *3* (4), 171–176.

(86) Rauf, M. A.; Meetani, M. A.; Hisaindee, S. An Overview on the Photocatalytic Degradation of Azo Dyes in the Presence of TiO_2 Doped with Selective Transition Metals. *Desalination* **2011**, *276* (1–3), 13–27.

(87) Wu, W.; Zhao, W.; Wu, Y.; Zhou, C.; Li, L.; Liu, Z.; Dong, J.; Zhou, K. Antibacterial Behaviors of Cu_2O Particles with Controllable Morphologies in Acrylic Coatings. *Appl Surf Sci* **2019**, *465*, 279–287.

(88) Wang, Y.; Deng, S.; Liu, B.; Jin, Y. Mechanistic Understanding on the Role of Cu Species over the CuO_x/TiO_2 Catalyst for CO_2 Photoreduction. *ACS Omega* **2020**, *5* (29), 18050–18063.

(89) Pongwan, P.; Wetchakun, K.; Phanichphant, S.; Wetchakun, N. Enhancement of Visible-Light Photocatalytic Activity of Cu-Doped TiO_2 Nanoparticles. *Research on Chemical Intermediates* **2016**, *42* (4), 2815–2830.

(90) Jiang, D.; Otitoju, T. A.; Ouyang, Y.; Shoparwe, N. F.; Wang, S.; Zhang, A.; Li, S. A Review on Metal Ions Modified TiO_2 for Photocatalytic Degradation of Organic Pollutants. *Catalysts 2021, Vol. 11, Page 1039* **2021**, *11* (9), 1039.

(91) Sudrajat, H.; Nguyen, T. K. Key Factors Controlling the Durability of a Cu-Doped TiO_2 Photocatalyst. *Optik (Stuttg)* **2020**, *217*, 164914.

(92) Endo-Kimura, M.; Janczarek, M.; Bielan, Z.; Zhang, D.; Wang, K.; Markowska-Szczupak, A.; Kowalska, E. Photocatalytic and Antimicrobial Properties of Ag_2O/TiO_2 Heterojunction. *ChemEngineering 2019, Vol. 3, Page 3* **2019**, *3* (1), 3.

(93) Halim, C. E.; Amal, R.; Beydoun, D.; Scott, J. A.; Low, G. Implications of the Structure of Cementitious Wastes Containing Pb(II), Cd(II), As(V), and Cr(VI) on the Leaching of Metals. *Cem Concr Res* **2004**, *34* (7), 1093–1102.

(94) Hua, L.; Yin, Z.; Cao, S. Recent Advances in Synthesis and Applications of Carbon-Doped TiO_2 Nanomaterials. *Catalysts 2020, Vol. 10, Page 1431* **2020**, *10* (12), 1431.

(95) Wong, M. S.; Hsu, S. W.; Rao, K. K.; Kumar, C. P. Influence of Crystallinity and Carbon Content on Visible Light Photocatalysis of Carbon Doped Titania Thin Films. *J Mol Catal A Chem* **2008**, *279* (1), 20–26.

(96) Wang, H., & Lewis, J. P. Effects of dopant states on photoactivity in Carbon-doped TiO_2. *Journal of Physics: Condensed Matter*, **2005**, *17*(21), L209.

(97) Asahi, R.; Morikawa, T.; Ohwaki, T.; Aoki, K.; Taga, Y. Visible-Light Photocatalysis in Nitrogen-Doped Titanium Oxides. *Science (1979)* **2001**, *293* (5528), 269–271.

(98) Ananpattarachai, J.; Seraphin, S.; Kajitvichyanukul, P. Formation of Hydroxyl Radicals and Kinetic Study of 2-Chlorophenol Photocatalytic Oxidation Using C-Doped TiO_2, N-Doped TiO_2, and C,N Co-Doped TiO_2 under Visible Light. *Environmental Science and Pollution Research* **2016**, *23* (4), 3884–3896.

(99) Li, G.; Zou, B.; Feng, S.; Shi, H.; Liao, K.; Wang, Y.; Wang, W.; Zhang, G. Synthesis of N-Doped TiO_2 with Good Photocatalytic Property. *Physica B Condens Matter* **2020**, *588*.

(100) Liu, L.; Yu, P. Y.; Chen, X.; Mao, S. S.; Shen, D. Z. Hydrogenation and Disorder in Engineered Black TiO_2. *Phys Rev Lett* **2013**, *111* (6), 065505.

(101) Tian, M.; Mahjouri-Samani, M.; Eres, G.; Sachan, R.; Yoon, M.; Chisholm, M. F.; Wang, K.; Puretzky, A. A.; Rouleau, C. M.; Geohegan, D. B.; Duscher, G. Structure and Formation Mechanism of Black TiO_2 Nanoparticles. *ACS Nano* **2015**, *9* (10), 10482–10488.

(102) Zhang, K.; Park, J. H. Surface Localization of Defects in Black TiO_2: Enhancing Photoactivity or Reactivity. *Journal of Physical Chemistry Letters* **2017**, *8* (1), 199–207.

(103) Chen, X.; Liu, L.; Yu, P. Y.; Mao, S. S. Increasing Solar Absorption for Photocatalysis with Black Hydrogenated Titanium Dioxide Nanocrystals. *Science (1979)* **2011**, *331* (6018), 746–750.

(104) Yan, X.; Li, Y.; Xia, T. Black Titanium Dioxide Nanomaterials in Photocatalysis. *International Journal of Photoenergy* **2017**, *2017*.

(105) Ullattil, S. G.; Narendranath, S. B.; Pillai, S. C.; Periyat, P. Black TiO_2 Nanomaterials: A Review of Recent Advances. *Chemical Engineering Journal* **2018**, *343*, 708–736.

(106) Liu, N.; Schneider, C.; Freitag, D.; Hartmann, M.; Venkatesan, U.; Müller, J.; Spiecker, E.; Schmuki, P. Black TiO_2 Nanotubes: Cocatalyst-Free Open-Circuit Hydrogen Generation. *Nano Lett* **2014**, *14* (6), 3309–3313.

(107) Chatzitakis, A.; Sartori, S. Recent Advances in the Use of Black TiO_2 for Production of Hydrogen and Other Solar Fuels. *ChemPhysChem* **2019**, *20* (10), 1272–1281.

(108) Shyichuk, A.; Zych, E. Oxygen Vacancy, Oxygen Vacancy−Vacancy Pairs, and Frenkel Defects in Cubic Lutetium Oxide. *J. Phys. Chem. C* **2020**, *124*, 14945–14962.

(109) Song, H.; Li, C.; Lou, Z.; Ye, Z.; Zhu, L. Effective Formation of Oxygen Vacancies in Black TiO_2 Nanostructures with Efficient Solar-Driven Water Splitting. *ACS Sustain Chem Eng* **2017**, *5* (10), 8982–8987.

(110) Li, W.; Liu, S.; Wang, S.; Guo, Q.; Guo, J. The Roles of Reduced Ti Cations and Oxygen Vacancies in Water Adsorption and Dissociation on $SrTiO_3$ (110). *J. Phys. Chem. C* **2014**, *118*, 24.

(111) Xu, M.; Chen, Y.; Qin, J.; Feng, Y.; Li, W.; Chen, W.; Zhu, J.; Li, H.; Bian, Z. Unveiling the Role of Defects on Oxygen Activation and Photodegradation of Organic Pollutants. *Environ Sci Technol* **2018**, *52* (23), 13879–13886.

(112) Henderson, M. A.; Epling, W. S.; Peden, C. H. F.; Perkins, C. L. Insights into Photoexcited Electron Scavenging Processes on TiO_2 Obtained from Studies of the Reaction of O_2 with OH Groups Adsorbed at Electronic Defects on TiO_2 (110). *Journal of Physical Chemistry B* **2003**, *107* (2), 534–545.

(113) Cheng, J.; Vandevondele, J.; Sprik, M. Identifying Trapped Electronic Holes at the Aqueous TiO_2 Interface. *Journal of Physical Chemistry C* **2014**, *118* (10), 5437–5444.

(114) Zhuang, J.; Weng, S.; Dai, W.; Liu, P.; Liu, Q. Effects of Interface Defects on Charge Transfer and Photoinduced Properties of TiO_2 Bilayer Films. *Journal of Physical Chemistry C* **2012**, *116* (48), 25354–25361.

(115) Tan, H.; Zhao, Z.; Niu, M.; Mao, C.; Cao, D.; Cheng, D.; Feng, P.; Sun, Z. A Facile and Versatile Method for Preparation of Colored TiO_2 with Enhanced Solar-Driven Photocatalytic Activity. *Nanoscale* **2014**, *6* (17), 10216–10223.

(116) Naldoni, A.; Allieta, M.; Santangelo, S.; Marelli, M.; Fabbri, F.; Cappelli, S.; Bianchi, C. L.; Psaro, R.; Dal Santo, V. Effect of Nature and Location of Defects on Band gap Narrowing in Black TiO_2 Nanoparticles. *J Am Chem Soc* **2012**, *134* (18), 7600–7603.

(117) Ariyanti, D.; Mills, L.; Dong, J.; Yao, Y.; Gao, W. $NaBH_4$ Modified TiO_2: Defect Site Enhancement Related to Its Photocatalytic Activity. *Mater Chem Phys* **2017**, *199*, 571–576.

(118) Hilgendorff, M.; Sundström, V. Dynamics of Electron Injection and Recombination of Dye-Sensitized TiO_2 Particles. *Journal of Physical Chemistry B* **1998**, *102* (51), 10505–10514.

(119) Andrade, J., Fernández-González, V., López-Mahía, P., & Muniategui, S. A low-cost system to simulate environmental microplastic weathering. *Marine Pollution Bulletin*, **2019,** *149*, 110663.

(120) Liang, Y.; Ma, H.; Zhang, W.; Cui, Z.; Fu, P.; Liu, M.; Qiao, X.; Pang, X. Size Effect of Semiconductor Quantum Dots as Photocatalysts for PET-RAFT Polymerization. *Polym Chem* **2020**, *11* (31), 4961–4967.

(121) Zhu, Q.; Peng, Y.; Lin, L.; Fan, C. M.; Gao, G. Q.; Wang, R. X.; Xu, A. W. Stable Blue TiO_{2-x} Nanoparticles for Efficient Visible Light Photocatalysts. *J Mater Chem A Mater* **2014**, *2* (12), 4429–4437.

(122) Henderson, M. A.; Epling, W. S.; Peden, C. H. F.; Perkins, C. L. Insights into Photoexcited Electron Scavenging Processes on TiO_2 Obtained from Studies of the Reaction of O_2 with OH Groups Adsorbed at Electronic Defects on TiO_2 (110). *Journal of Physical Chemistry B* **2002**, *107* (2), 534–545.

(123) Hoffmann, M. R.; Martin, S. T.; Choi, W.; Bahnemann1', D. W.; Keck, W. M. Environmental Applications of Semiconductor Photocatalysis. *Chem. Rev* **1995**, *95*, 69–96.

(124) Munuera, G.; Rives-Arnau, V.; Saucedo, A. Photo-Adsorption and Photo-Desorption of Oxygen on Highly Hydroxylated TiO_2 Surfaces. Part 1.—Role of Hydroxyl Groups in Photo-Adsorption. *Journal of the Chemical Society, Faraday Transactions 1: Physical Chemistry in Condensed Phases* **1979**, *75* (0), 736–747.

(125) Jeon, J.-P.; Kweon, H.; Jang, J.; Ju, M. J.; Baek, J.-B.; Jeon, J.-P.; Kweon, D. H.; Jang, B. J.; Ju, M. J.; Baek, J.-B. Enhancing the Photocatalytic Activity of TiO_2 Catalysts. *Adv Sustain Syst* **2020**, *4* (12), 2000197.

(126) Fang, M. J., Tsao, C. W., & Hsu, Y. J. Semiconductor nanoheterostructures for photoconversion applications. *Journal of Physics D: Applied Physics*, **2020**, *53*(14), 143001.

(127) Bakar, S. A.; Ribeiro, C. A Comparative Run for Visible-Light-Driven Photocatalytic Activity of Anionic and Cationic S-Doped TiO_2 Photocatalysts: A Case Study of Possible Sulfur Doping through Chemical Protocol. *J Mol Catal A Chem* **2016**, *421*, 1–15.

(128) Drummer, S.; Madzimbamuto, T.; Chowdhury, M. Green Synthesis of Transition-Metal Nanoparticles and Their Oxides: A Review. *Materials 2021, Vol. 14, Page 2700* **2021**, *14* (11), 2700.

(129) Sudha, D.; Sivakumar, P. Review on the Photocatalytic Activity of Various Composite Catalysts. *Chemical Engineering and Processing: Process Intensification* **2015**, *97*, 112–133.

(130) Negem, M.; Nady, H. Benchmark Electrocatalysis Activity of 3D-Ni-Co-TiO_2 Nanocomposites for Hydrogen Fuel Production Via Alkaline Electrolytes. *J Mater Eng Perform* **2020**, *29* (10), 6940–6951.

(131) Rajeshwar, K.; Thomas, A.; Janaky, C. Photocatalytic Activity of Inorganic Semiconductor Surfaces: Myths, Hype, and Reality. *Journal of Physical Chemistry Letters* **2015**, *6* (1), 139–147.

(132) Suryanarayana, C.; Norton, M. G. X-Rays and Diffraction. *X-Ray Diffraction* **1998**, 3–19.

(133) Bunaciu, A. A.; Udriştioiu, E. gabriela; Aboul-Enein, H. Y. X-Ray Diffraction: Instrumentation and Applications. **2015**, *45* (4), 289–299.

(134) Whittig, L. D.; Allardice, W. R. X-Ray Diffraction Techniques. *Methods of Soil Analysis, Part 1: Physical and Mineralogical Methods* **2018**, 331–362.

(135) Agarwal, B. K. *X-ray spectroscopy: an introduction* (Vol. 15). **2013**, Springer.

(136) Harris, W.; White, G. N. X-Ray Diffraction Techniques for Soil Mineral Identification. *Methods of Soil Analysis, Part 5: Mineralogical Methods* **2015**, *5*, 81–115.

(137) Mos, Y. M.; Vermeulen, A. C.; Buisman, C. J. N.; Weijma, J. X-Ray Diffraction of Iron Containing Samples: The Importance of a Suitable Configuration. *1401183* **2018**, *35* (6), 511–517.

(138) Waseda, Y.; Matsubara, E.; Shinoda, K. Fundamental Properties of X-Rays. *X-Ray Diffraction Crystallography* **2011**, 1–20.

(139) Iwashita, N. X-Ray Powder Diffraction. *Materials Science and Engineering of Carbon* **2016**, 7–25.

(140) Stanjek, H.; Häusler, W. Basics of X-Ray Diffraction. *Hyperfine Interactions 2004 154:1* **2004**, *154* (1), 107–119.

(141) Lee, M. *X-Ray diffraction for materials research: from fundamentals to applications*. **2017**, CRC Press.

(142) Wang, Z. L. New Developments in Transmission Electron Microscopy for Nanotechnology. *Advanced Materials* **2003**, *15* (18), 1497–1514.

(143) Franken, L. E.; Boekema, E. J.; Stuart, M. C. A. Transmission Electron Microscopy as a Tool for the Characterization of Soft Materials: Application and Interpretation. *Advanced Science* **2017**, *4* (5), 1600476.

(144) Davis, C. Q.; Freeman, D. M. Using a Light Microscope to Measure Motions with Nanometer Accuracy. *https://doi.org/10.1117/1.601967* **1998**, *37* (4), 1299–1304.

(145) McConnell, G.; Trägårdh, J.; Amor, R.; Dempster, J.; Reid, E.; Amos, W. B. A Novel Optical Microscope for Imaging Large Embryos and Tissue Volumes with Sub-Cellular Resolution Throughout. *Elife* **2016**, *5* (September).

(146) Zhu, Y.; Dürr, H. The Future of Electron Microscopy. *Phys Today* **2015**, *68* (4), 32–38.

(147) Zaefferer, S. A Critical Review of Orientation Microscopy in SEM and TEM. *Crystal Research and Technology* **2011**, *46* (6), 607–628.

(148) Alberti, G.; Nuzzaci, G. 1.6.5 SEM and TEM Techniques. *World Crop Pests* **1996**, *6* (Eriophyoid Mites Their Biology, Natural Enemies and Control), 399–410.

(149) Zhou, W.; Apkarian, R. P.; Lin Wang, Z.; Joy, D. Fundamentals of Scanning Electron Microscopy.

(150) Inkson, B. J. Scanning Electron Microscopy (SEM) and Transmission Electron Microscopy (TEM) for Materials Characterization. *Materials Characterization Using Nondestructive Evaluation (NDE) Methods* **2016**, 17–43.

(151) Reimer, L. Scanning Electron Microscopy: Physics of Image Formation and Microanalysis, Second Edition. *Meas Sci Technol* **2000**, *11* (12), 1826.

(152) Henini, M. Scanning Electron Microscopy: An Introduction. *III-Vs Review* **2000**, *13* (4), 40–44.

(153) Ul-Hamid, A. A Beginners' Guide to Scanning Electron Microscopy. *A Beginners' Guide to Scanning Electron Microscopy* **2018**.

(154) Zhou, W., & Wang, Z. L. *Scanning microscopy for nanotechnology: techniques and applications*. Springer science & business media. **2007**, (Eds.).

(155) Inkson, B. J. Scanning Electron Microscopy (SEM) and Transmission Electron Microscopy (TEM) for Materials Characterization. *Materials Characterization Using Nondestructive Evaluation (NDE) Methods* **2016**, 17–43.

(156) Kannan, M. Transmission electron microscope—Principle, components and applications. *A textbook on fundamentals and applications of nanotechnology*, **2018**, 93-102.

(157) Malenica, M.; Vukomanović, M.; Kurtjak, M.; Masciotti, V.; Dal Zilio, S.; Greco, S.; Lazzarino, M.; Krušić, V.; Perčić, M.; Badovinac, I. J.; Wechtersbach, K.; Vidović, I.; Baričević, V.; Valić, S.; Lučin, P.; Kojc, N.; Grabušić, K. Perspectives of Microscopy Methods for Morphology Characterisation of Extracellular Vesicles from Human Biofluids. *Biomedicines* **2021**, *9* (6), 603.

(158) Lee, M. *X-Ray diffraction for materials research: from fundamentals to applications*. **2017**. CRC Press.

(159) Giannuzzi, L. A.; Stevie, F. A. A Review of Focused Ion Beam Milling Techniques for TEM Specimen Preparation. *Micron* **1999**, *30* (3), 197–204.

(160) J Bollmann, T. R.; van Gastel, R.; W Zandvliet, H. J.; -, al; Man, K. L.; Altman -, M. S.; Poelsema, B.; Altman, M. S.; Altman, M. S. Trends in Low Energy Electron Microscopy. *Journal of Physics: Condensed Matter* **2010**, *22* (8), 084017.

(161) Diebold, A. C.; Foran, B.; Kisielowski, C.; Muller, D. A.; Pennycook, S. J.; Principe, E.; Stemmer, S. Thin Dielectric Film Thickness Determination by Advanced Transmission Electron Microscopy. *Microscopy and Microanalysis* **2003**, *9* (6), 493–508.

(162) Maciejewska, B. M.; Jasiurkowska-Delaporte, M.; Vasylenko, A. I.; Kozioł, K. K.; Jurga, S. Experimental and Theoretical Studies on the Mechanism for Chemical Oxidation of Multiwalled Carbon Nanotubes. *RSC Adv* **2014**, *4* (55), 28826–28831.

(163) Mohrhusen, L.; Osmić, M. Sterical Ligand Stabilization of Nanocrystals versus Electrostatic Shielding by Ionic Compounds: A Principle Model Study with TEM and XPS. *RSC Adv* **2017**, *7* (21), 12897–12907.

(164) Aziz, M.; Ismail, A. F. X-Ray Photoelectron Spectroscopy (XPS). *Membrane Characterization* **2017**, 81–93.

(165) Greczynski, G.; Hultman, L. X-Ray Photoelectron Spectroscopy: Towards Reliable Binding Energy Referencing. *Prog Mater Sci* **2020**, *107*, 100591.

(166) Hüfner, S. *Photoelectron spectroscopy: principles and applications*. **2013**, Springer Science & Business Media.

(167) Van der Heide, P. X-Ray Photoelectron Spectroscopy: An Introduction to Principles and Practices. **2012**.

(168) Fadley, C. S. X-ray photoelectron spectroscopy: Progress and perspectives. *Journal of Electron Spectroscopy and Related Phenomena*, **2010**, *178*, 2-32.

(169) Benigna, J. Photoelectron Spectroscopy in Advanced Placement Chemistry. *J Chem Educ* **2014**, *91* (9), 1299–1305.

(170) Stevie, F. A.; Donley, C. L. Introduction to X-Ray Photoelectron Spectroscopy. *Journal of Vacuum Science & Technology A: Vacuum, Surfaces, and Films* **2020**, *38* (6), 063204.

(171) Seyama, H.; Soma, M.; Theng, B. K. G. X-Ray Photoelectron Spectroscopy. *Dev Clay Sci* **2013**, *5* (C), 161–176.

(172) Seah, M. P. The Quantitative Analysis of Surfaces by XPS: A Review. *Surface and Interface Analysis* **1980**, *2* (6), 222–239.

(173) Jablonski, A.; Powell, C. J. Relationships between Electron Inelastic Mean Free Paths, Effective Attenuation Lengths, and Mean Escape Depths. *J Electron Spectros Relat Phenomena* **1999**, *100* (1–3), 137–160.

(174) Watts, J. F., & Wolstenholme, J, *An introduction to surface analysis by XPS and AES*. **2019**, John Wiley & Sons.

(175) Proctor, A., & Sherwood, P. M. Data analysis techniques in x-ray photoelectron spectroscopy. *Analytical Chemistry*, **1982**, *54*(1), 13-19.

(176) Bosch Ojeda, C.; Sanchez Rojas, F. Recent Applications in Derivative Ultraviolet/Visible Absorption Spectrophotometry: 2009–2011: A Review. *Microchemical Journal* **2013**, *106*, 1–16.

(177) Passos, M. L. C.; Sarraguça, M. C.; Saraiva, M. L. M. F. S. Spectrophotometry | Organic Compounds. *Encyclopedia of Analytical Science* **2019**, 236–243.

(178) Ricciardi, P. UV-Visible-near IR Reflectance Spectrophotometry in a Museum Environment. *Spectroscopy, Diffraction and Tomography in Art and Heritage Science* **2021**, 103–131.

(179) L.C. Passos, M.; M.F.S. Saraiva, M. L. Detection in UV-Visible Spectrophotometry: Detectors, Detection Systems, and Detection Strategies. *Measurement* **2019**, *135*, 896–904.

(180) Perkampus, H. *UV-VIS Spectroscopy and Its Applications*; **2013**, Springer Science & Business Media.

(181) Tan, K.; Cheng, X. Specular Reflection Effects Elimination in Terrestrial Laser Scanning Intensity Data Using Phong Model. *Remote Sensing 2017, Vol. 9, Page 853* **2017**, *9* (8), 853.

(182) Torrent, J.; Barrón, V. Diffuse Reflectance Spectroscopy. *Methods of Soil Analysis, Part 5: Mineralogical Methods* **2015**, *5*, 367–385.

(183) Mishra, V.; Warshi, M. K.; Sati, A.; Kumar, A.; Mishra, V.; Kumar, R.; Sagdeo, P. R. Investigation of Temperature-Dependent Optical Properties of TiO_2 Using Diffuse Reflectance Spectroscopy. *SN Appl Sci* **2019**, *1* (3), 1–8.

(184) Nowak, M.; Kauch, B.; Szperlich, P. Determination of Energy Band Gap of Nanocrystalline SbSI Using Diffuse Reflectance Spectroscopy. *Review of Scientific Instruments* **2009**, *80* (4), 046107.

(185) López, R.; Gómez, R. Band-Gap Energy Estimation from Diffuse Reflectance Measurements on Sol-Gel and Commercial TiO_2: A Comparative Study. *J Solgel Sci Technol* **2012**, *61* (1), 1–7.

(186) Kang, X.; Liu, S.; Dai, Z.; He, Y.; Song, X.; Tan, Z. Titanium Dioxide: From Engineering to Applications. *Catalysts 2019, Vol. 9, Page 191* **2019**, *9* (2), 191.

(187) Hamad, H.; Bailón-García, E.; Maldonado-Hódar, F. J.; Pérez-Cadenas, A. F.; Carrasco-Marín, F.; Morales-Torres, S. Synthesis of Ti_xO_y Nanocrystals in Mild Synthesis Conditions for the Degradation of Pollutants under Solar Light. *Appl Catal B* **2019**, *241*, 385–392.

(188) Naldoni, A.; Altomare, M.; Zoppellaro, G.; Liu, N.; Kment, Š.; Zbořil, R.; Schmuki, P. Photocatalysis with Reduced TiO_2: From Black TiO_2 to Cocatalyst-Free Hydrogen Production. *ACS Catal* **2019**, *9* (1), 345–364.

(189) Gupta, T.; Samriti; Cho, J.; Prakash, J. Hydrothermal Synthesis of TiO_2 Nanorods: Formation Chemistry, Growth Mechanism, and Tailoring of Surface Properties for Photocatalytic Activities. *Mater Today Chem* **2021**, *20*, 100428.

(190) Lee, Y. R.; Kim, J.; Ahn, W. S. Synthesis of Metal-Organic Frameworks: A Mini Review. *Korean Journal of Chemical Engineering 2013 30:9* **2013**, *30* (9), 1667–1680.

(191) Walton, R. I. Subcritical Solvothermal Synthesis of Condensed Inorganic Materials. *Chem Soc Rev* **2002**, *31* (4), 230–238.

(192) Malekshahi Byranvand, M.; Nemati Kharat, A.; Fatholahi, L.; Malekshahi Beiranvand, Z. A Review on Synthesis of Nano-TiO_2 via Different Methods. *Journal of Nanostructures* **2013**, *3* (1), 1–9.

(193) Bian, Z.; Zhu, J.; Li, H. Solvothermal Alcoholysis Synthesis of Hierarchical TiO_2 with Enhanced Activity in Environmental and Energy Photocatalysis. *Journal of Photochemistry and Photobiology C: Photochemistry Reviews* **2016**, *28*, 72–86.

(194) Courtecuisse, V. G.; Chhor, K.; Bocquet, J. F.; Pommier, C. Kinetics of the Titanium Isopropoxide Decomposition in Supercritical Isopropyl Alcohol. *Ind Eng Chem Res* **1996**, *35* (8), 2539–2545.

(195) Kominami, H.; Kato, J. I.; Murakami, S. Y.; Kera, Y.; Inoue, M.; Inui, T.; Ohtani, B. Synthesis of Titanium (IV) Oxide of Ultra-High Photocatalytic Activity: High-Temperature Hydrolysis of Titanium Alkoxides with Water Liberated Homogeneously from Solvent Alcohols. *J Mol Catal A Chem* **1999**, *144* (1), 165–171.

(196) Demazeau, G. Solvothermal Processes: A Route to the Stabilization of New Material. *J Mater Chem* **1999**, *9* (1), 15–18.

(197) Gonzalo-Juan, I., & Riedel, R. Ceramic synthesis from condensed phases. *ChemTexts*, **2016**, *2*(2), 1-21.

(198) Takahashi, Y.; Suzuki, H.; Nasu, M. Rutile Growth at the Surface of TiO_2 Films Deposited by Vapour-Phase Decomposition of Isopropyl Titanate. *Journal of the Chemical Society, Faraday Transactions 1: Physical Chemistry in Condensed Phases* **1985**, *81* (12), 3117–3125.

(199) Naldoni, A.; Allieta, M.; Santangelo, S.; Marelli, M.; Fabbri, F.; Cappelli, S.; Bianchi, C. L.; Psaro, R.; Dal Santo, V. Effect of Nature and Location of Defects on Band gap Narrowing in Black TiO_2 Nanoparticles. *J Am Chem Soc* **2012**, *134* (18), 7600–7603.

(200) Rajaraman, T. S.; Parikh, S. P.; Gandhi, V. G. Black TiO_2: A Review of Its Properties and Conflicting Trends. *Chemical Engineering Journal* **2020**, *389*, 123918.

(201) Wang, B.; Shen, S.; Mao, S. S. Black TiO_2 for Solar Hydrogen Conversion. *Journal of Materiomics* **2017**, *3* (2), 96–111.

(202) Leshuk, T.; Parviz, R.; Everett, P.; Krishnakumar, H.; Varin, R. A.; Gu, F. Photocatalytic Activity of Hydrogenated TiO_2. *ACS Appl Mater Interfaces* **2013**, *5* (6), 1892–1895.

(203) Hubert, J. C.; Wijnberg, J. B. P. A.; Speckamp, W. N. $NaBH_4$ Reduction of Cyclic Imides. *Tetrahedron* **1975**, *31* (11–12), 1437–1441.

(204) Martelli, P.; Caputo, R.; Remhof, A.; Mauron, P.; Borgschulte, A.; Z̈ttel, A. Stability and Decomposition of $NaBH_4$. *Journal of Physical Chemistry C* **2010**, *114* (15), 7173–7177.

(205) Vilardi, G.; Verdone, N.; Bubbico, R. Combined Production of Metallic-Iron Nanoparticles: Exergy and Energy Analysis of Two Alternative Processes Using Hydrazine and $NaBH_4$ as Reducing Agents. *J Taiwan Inst Chem Eng* **2021**, *118*, 97–111.

(206) Xia, T.; Wallenmeyer, P.; Anderson, A.; Murowchick, J.; Liu, L.; Chen, X. Hydrogenated Black ZnO Nanoparticles with Enhanced Photocatalytic Performance. *RSC Adv* **2014**, *4* (78), 41654–41658.

(207) Jiang, L.; Chen, D.; Qin, L.; Liang, J.; Sun, X.; Huang, Y. Enhanced Photocatalytic Activity of Hydrogenated $BiVO_4$ with Rich Surface-Oxygen-Vacancies for Remarkable Degradation of Tetracycline Hydrochloride. *J Alloys Compd* **2019**, *783*, 10–18.

(208) Wen, Y.; Qu, D.; An, L.; Gao, X.; Jiang, W.; Wu, D.; Yang, D.; Sun, Z. Defective G-C_3N_4 Prepared by the $NaBH_4$ Reduction for High-Performance H_2 Production. *ACS Sustain Chem Eng* **2019**, *7* (2), 2343–2349.

(209) Jo, W. K.; Kim, Y. G.; Tonda, S. Hierarchical Flower-like NiAl-Layered Double Hydroxide Microspheres Encapsulated with Black Cu-Doped TiO_2 Nanoparticles: Highly Efficient Visible-Light-Driven Composite Photocatalysts for Environmental Remediation. *J Hazard Mater* **2018**, *357*, 19–29.

(210) Fang, W.; Xing, M.; Zhang, J. A New Approach to Prepare Ti^{3+} Self-Doped TiO_2 via $NaBH_4$ Reduction and Hydrochloric Acid Treatment. *Appl Catal B* **2014**, *160–161* (1), 240–246.

(211) Kılınç, D.; Şahin, Ö. Effective TiO_2 Supported Cu-Complex Catalyst in $NaBH_4$ Hydrolysis Reaction to Hydrogen Generation. *Int J Hydrogen Energy* **2019**, *44* (34), 18858–18865.

(212) Zhang, K.; Suh, J. M.; Choi, J. W.; Jang, H. W.; Shokouhimehr, M.; Varma, R. S. Recent Advances in the Nanocatalyst-Assisted $NaBH_4$ Reduction of Nitroaromatics in Water. *ACS Omega* **2019**, *4* (1), 483–495.

(213) Choudhury, B.; Dey, M.; Choudhury, A. Defect Generation, d-d Transition, and Band Gap Reduction in Cu-Doped TiO_2 Nanoparticles. *International Nano Letters 2013 3:1* **2013**, *3* (1), 1–8.

(214) Tsai, C. Y.; Hsi, H. C.; Kuo, T. H.; Chang, Y. M.; Liou, J. H. Preparation of Cu-Doped TiO_2 Photocatalyst with Thermal Plasma Torch for Low-Concentration Mercury Removal. *Aerosol Air Qual Res.* **2013**, *13* (2), 639–648.

(215) Makkar, M.; Viswanatha, R. Frontier Challenges in Doping Quantum Dots: Synthesis and Characterization. *RSC Adv* **2018**, *8* (39), 22103–22112.

(216) Bai, B.; Xu, M.; Li, J.; Zhang, S.; Qiao, C.; Liu, J.; Zhang, J.; Bai, B.; Xu, M.; Li, J. Z.; Zhang, S. P.; Liu, J. J.; Zhang, J. T.; Qiao, C. Dopant Diffusion Equilibrium Overcoming Impurity Loss of Doped QDs for Multimode Anti-Counterfeiting and Encryption. *Adv Funct Mater* **2021**, *31* (25), 2100286.

(217) Cumpson, P. J. Angle-Resolved XPS and AES: Depth-Resolution Limits and a General Comparison of Properties of Depth-Profile Reconstruction Methods. *J Electron Spectros Relat Phenomena* **1995**, *73* (1), 25–52.

(218) Iqbal, J.; Jan, T.; Ul-Hassan, S.; Ahmed, I.; Mansoor, Q.; Umair Ali, M.; Abbas, F.; Ismail, M. Facile Synthesis of Zn Doped CuO Hierarchical Nanostructures: Structural, Optical and Antibacterial Properties. *AIP Adv* **2015**, *5* (12), 127112.

(219) Behera, M.; Nayak, J.; Banerjee, S.; Chakrabortty, S.; Tripathy, S. K. A Review on the Treatment of Textile Industry Waste Effluents towards the Development of Efficient Mitigation Strategy: An Integrated System Design Approach. *J Environ Chem Eng* **2021**, *9* (4), 105277.

(220) Rathinam, R., Govindaraj, M., Vijayakumar, K., & Pattabhi, S. Removal of Colour from Aqueous Rhodamine B Dye Solution by Photo electrocoagulation Treatment Techniques. *Journal of Engineering, Scientific Research and Application*, **2015**, *1*(2), 80-89.

(221) Carmen, Z., & Daniela, S. *Textile organic dyes-characteristics, polluting effects and separation/elimination procedures from industrial effluents-a critical overview*, **2012**, (Vol. 3, pp. 55-86). Rijeka: IntechOpen.

(222) Salleh, M. A. M.; Mahmoud, D. K.; Karim, W. A. W. A.; Idris, A. Cationic and Anionic Dye Adsorption by Agricultural Solid Wastes: A Comprehensive Review. *Desalination* **2011**, *280* (1–3), 1–13.

(223) Ismail, M.; Akhtar, K.; Khan, M. I.; Kamal, T.; Khan, M. A.; M. Asiri, A.; Seo, J.; Khan, S. B. Pollution, Toxicity and Carcinogenicity of Organic Dyes and Their Catalytic Bio-Remediation. *Curr Pharm Des* **2019**, *25* (34), 3645–3663.

(224) Rahman, Q. I.; Ahmad, M.; Misra, S. K.; Lohani, M. Effective Photocatalytic Degradation of Rhodamine B Dye by ZnO Nanoparticles. *Mater Lett* **2013**, *91*,

(225) Xu, D.; Ma, H. Degradation of Rhodamine B in Water by Ultrasound-Assisted TiO_2 Photocatalysis. *J Clean Prod* **2021**, *313*, 127758.

(226) Aarthi, T.; Madras, G. Photocatalytic Degradation of Rhodamine Dyes with Nano-TiO_2. *Ind Eng Chem Res* **2007**, *46* (1), 7–14.

(227) Soares, E. T., Lansarin, M. A., & Moro, C. C. A study of process variables for the photocatalytic degradation of rhodamine B. *Brazilian Journal of Chemical Engineering*, **2007**, *24*, 29-36.

(228) Ajmal, A.; Majeed, I.; Malik, R. N.; Idriss, H.; Nadeem, M. A. Principles and Mechanisms of Photocatalytic Dye Degradation on TiO_2 Based Photocatalysts: A Comparative Overview. *RSC Adv* **2014**, *4* (70), 37003–37026.

(229) Ayodhya, D.; Veerabhadram, G. A Review on Recent Advances in Photodegradation of Dyes Using Doped and Heterojunction Based Semiconductor Metal Sulfide Nanostructures for Environmental Protection. *Mater Today Energy* **2018**, *9*, 83–113.

(230) Hashimoto, K.; Hiramoto, M.; Sakata, T. Temperature-Independent Electron Transfer: Rhodamine B/Oxide Semiconductor Dye-Sensitization System. **1988**, *92*, 4272–4274.

(231) Pingmuang, K.; Chen, J.; Kangwansupamonkon, W.; Wallace, G. G.; Phanichphant, S.; Nattestad, A. Composite Photocatalysts Containing $BiVO_4$ for Degradation of Cationic Dyes. *Scientific Reports 2017 7:1* **2017**, *7* (1), 1–11.

(232) Wang, J. L.; Xu, L. J. Advanced Oxidation Processes for Wastewater Treatment: Formation of Hydroxyl Radical and Application. *Crit Rev Environ Sci Technol* **2012**, *42* (3), 251–325.

(233) Zhao, X., Liu, J., Fan, J., Chao, H., & Peng, X. Recent progress in photosensitizers for overcoming the challenges of photodynamic therapy: from molecular design to application. *Chemical Society Reviews*, **2021**, *50*(6), 4185-4219.

(234) Hairom, N. H. H.; Mohammad, A. W.; Ng, L. Y.; Kadhum, A. A. H. Utilization of Self-Synthesized ZnO Nanoparticles in MPR for Industrial Dye Wastewater Treatment Using NF and UF Membrane. *Desalination Water Treat* **2015**, *54* (4–5), 944–955.

(235) Vasiljevic, Z. Z.; Dojcinovic, M. P.; Vujancevic, J. D.; Jankovic-Castvan, I.; Ognjanovic, M.; Tadic, N. B.; Stojadinovic, S.; Brankovic, G. O.; Nikolic, M. v. Photocatalytic Degradation of Methylene Blue under Natural Sunlight Using Iron Titanate Nanoparticles Prepared by a Modified Sol–Gel Method. *R Soc Open Sci* **2020**, *7* (9).

(236) Saeed, M.; Usman, M.; Haq, A. ul. Catalytic Degradation of Organic Dyes in Aqueous Medium. *Photochemistry and Photophysics-Fundamentals to Applications* **2018**.

(237) Tang, J.; Li, D.; Feng, Z.; Tan, Z.; Ou, B. A Novel $AgIO_4$ Semiconductor with Ultrahigh Activity in Photodegradation of Organic Dyes: Insights into the Photosensitization Mechanism. *RSC Adv* **2013**, *4* (5), 2151–2154.

(238) Lai, Y. J.; Lee, D. J. Pollutant Degradation with Mediator Z-Scheme Heterojunction Photocatalyst in Water: A Review. *Chemosphere* **2021**, *282*, 131059.

(239) Talukdar, S.; Dutta, R. K. A Mechanistic Approach for Superoxide Radicals and Singlet Oxygen Mediated Enhanced Photocatalytic Dye Degradation by Selenium Doped ZnS Nanoparticles. *RSC Adv* **2015**, *6* (2), 928–936.

(240) DeRosa, M. C.; Crutchley, R. J. Photosensitized Singlet Oxygen and Its Applications. *Coord Chem Rev* **2002**, *233–234*, 351–371.

(241) Li, G.; Yi, L.; Wang, J.; Song, Y. Hydrodynamic Cavitation Degradation of Rhodamine B Assisted by Fe^{3+}-Doped TiO_2: Mechanisms, Geometric and Operation Parameters. *Ultrason Sonochem* **2020**, *60*, 104806.

(242) Kubiak, A.; Bielan, Z.; Kubacka, M.; Gabała, E.; Zgoła-Grześkowiak, A.; Janczarek, M.; Zalas, M.; Zielińska-Jurek, A.; Siwińska-Ciesielczyk, K.; Jesionowski, T. Microwave-Assisted Synthesis of a TiO_2-CuO Heterojunction with Enhanced Photocatalytic Activity against Tetracycline. *Appl Surf Sci.* **2020**, *520*, 146344.

(243) Brynildsen, M. P.; Winkler, J. A.; Spina, C. S.; MacDonald, I. C.; Collins, J. J. Potentiating Antibacterial Activity by Predictably Enhancing Endogenous Microbial ROS Production. *Nature Biotechnology 2013 31:2* **2013**, *31* (2), 160–165.

(244) Ma, H. Y.; Zhao, L.; Guo, L. H.; Zhang, H.; Chen, F. J.; Yu, W. C. Roles of Reactive Oxygen Species (ROS) in the Photocatalytic Degradation of Pentachlorophenol and Its Main Toxic Intermediates by TiO_2/UV. *J Hazard Mater* **2019**, *369*, 719–726.

(245) Cui, W.; Li, J.; Sun, Y.; Wang, H.; Jiang, G.; Lee, S. C.; Dong, F. Enhancing ROS Generation and Suppressing Toxic Intermediate Production in Photocatalytic NO Oxidation on O/Ba Co-Functionalized Amorphous Carbon Nitride. *Appl Catal B* **2018**, *237*, 938–946.

(246) Wang, D.; Zhao, L.; Guo, L. H.; Zhang, H. Online Detection of Reactive Oxygen Species in Ultraviolet (UV)-Irradiated Nano-TiO_2 Suspensions by Continuous Flow Chemiluminescence. *Anal Chem* **2014**, *86* (21), 10535–10539.

(247) Fernández-Castro, P.; Vallejo, M.; San Román, M. F.; Ortiz, I. Insight on the Fundamentals of Advanced Oxidation Processes. Role and Review of the Determination Methods of Reactive Oxygen Species. *Journal of Chemical Technology & Biotechnology* **2015**, *90* (5), 796–820.

(248) Ikram, M.; Hussain, I.; Hassan, J.; Haider, A.; Imran, M.; Aqeel, M.; Ul-Hamid, A.; Ali, S. Evaluation of Antibacterial and Catalytic Potential of Copper-Doped Chemically Exfoliated Boron Nitride Nanosheets. *Ceram Int* **2020**, *46* (13), 21073–21083.

(249) Yadav, H. M.; Otari, S. v.; Koli, V. B.; Mali, S. S.; Hong, C. K.; Pawar, S. H.; Delekar, S. D. Preparation and Characterization of Copper-Doped Anatase TiO_2 Nanoparticles with Visible Light Photocatalytic Antibacterial Activity. *J Photochem Photobiol A Chem* **2014**, *280*, 32–38.

(250) Chan, Y. H.; Huang, C. F.; Ou, K. L.; Peng, P. W. Mechanical Properties and Antibacterial Activity of Copper Doped Diamond-like Carbon Films. *Surf Coat Technol* **2011**, *206* (6), 1037–1040.

(251) Ma, G.; Liang, X.; Li, L.; Qiao, R.; Jiang, D.; Ding, Y.; Chen, H. Cu-Doped Zinc Oxide and Its Polythiophene Composites: Preparation and Antibacterial Properties. *Chemosphere* **2014**, *100*, 146–151.

(252) Bhuyan, T.; Khanuja, M.; Sharma, R.; Patel, S.; Reddy, M. R.; Anand, S.; Varma, A. A Comparative Study of Pure and Copper (Cu)-Doped ZnO Nanorods for Antibacterial and Photocatalytic Applications with Their Mechanism of Action. *Journal of Nanoparticle Research* **2015**, *17* (7), 1–11.

(253) Yao, X.; Zhang, X.; Wu, H.; Tian, L.; Ma, Y.; Tang, B. Microstructure and Antibacterial Properties of Cu-Doped TiO_2 Coating on Titanium by Micro-Arc Oxidation. *Appl Surf Sci* **2014**, *292*, 944–947.

(254) Johnson, J. R.; Russo, T. A. Extraintestinal Pathogenic *Escherichia Coli*: "The Other Bad *E. Coli*." *Journal of Laboratory and Clinical Medicine* **2002**, *139* (3), 155–162.

(255) Zhang, L.; Jiang, Y.; Ding, Y.; Daskalakis, N.; Jeuken, L.; Povey, M.; O'Neill, A. J.; York, D. W. Mechanistic Investigation into Antibacterial Behaviour of Suspensions of ZnO Nanoparticles against *E. Coli*. *Journal of Nanoparticle Research* **2010**, *12* (5), 1625–1636.

(256) Dasari, T. P.; Pathakoti, K.; Hwang, H. M. Determination of the Mechanism of Photoinduced Toxicity of Selected Metal Oxide Nanoparticles (ZnO, CuO, Co_3O_4 and TiO_2) to *E. Coli* Bacteria. *Journal of Environmental Sciences* **2013**, *25* (5), 882–888.

(257) Jia, Y.; Zhan, S.; Ma, S.; Zhou, Q. Fabrication of TiO_2-Bi_2WO_6 Binanosheet for Enhanced Solar Photocatalytic Disinfection of *E. Coli*: Insights on the Mechanism. *ACS Appl Mater Interfaces* **2016**, *8* (11), 6841–6851.

(258) Santos, M. A., Silva, F. L., Lira, B. O., Fh, J. L. C., Vasconcelos, A. G., Araujo, A. R., ... & Brand, G. D. Probing human proteins for short encrypted antimicrobial peptides reveals Hs10, a peptide with selective activity for gram-negative bacteria. *Biochimica et Biophysica Acta (BBA)-General Subjects*, **2022**, 130265.

(259) Bhakdi, S.; Mackman, N.; Menestrina, G.; Gray, L.; Hugo, F.; Seeger, W.; Holland, I. B. The Hemolysin of *Escherichia Coli*. *European Journal of Epidemiology 1988 4:2* **1988**, *4* (2), 135–143.

(260) Tu, Y.; Lv, M.; Xiu, P.; Huynh, T.; Zhang, M.; Castelli, M.; Liu, Z.; Huang, Q.; Fan, C.; Fang, H.; Zhou, R. Destructive Extraction of Phospholipids from *Escherichia Coli* Membranes by Graphene Nanosheets. *Nature Nanotechnology 2013 8:8* **2013**, *8* (8), 594–601.

(261) Zhou, Z.; Li, B.; Liu, X.; Li, Z.; Zhu, S.; Liang, Y.; Cui, Z.; Wu, S. Recent Progress in Photocatalytic Antibacterial. *ACS Appl Bio Mater* **2021**, *4* (5), 3909–3936.

(262) Lebedev, A.; Anariba, F.; Tan, J. C.; Li, X.; Wu, P. A Review of Physiochemical and Photocatalytic Properties of Metal Oxides against *Escherichia Coli*. *J Photochem Photobiol A Chem* **2018**, *360*, 306–315.

(263) Venkata, P.; Reddy, L.; Kavitha, B.; Reddy, A. K.; Kim, K.-H. TiO_2-Based Photocatalytic Disinfection of Microbes in Aqueous Media: A Review. **2017**.

(264) Inam, M.; Foster, J. C.; Gao, J.; Hong, Y.; Du, J.; Dove, A. P.; O'Reilly, R. K. Size and Shape Affects the Antimicrobial Activity of Quaternized Nanoparticles. *J Polym Sci A Polym Chem* **2019**, *57* (3), 255–259.

(265) Scheurwater, E. M.; Burrows, L. L. Maintaining Network Security: How Macromolecular Structures Cross the Peptidoglycan Layer. *FEMS Microbiol Lett* **2011**, *318* (1), 1–9.

(266) Mittler, R. ROS Are Good. *Trends Plant Sci* **2017**, *22* (1), 11–19.

(267) Imlay, J. A. Where in the World Do Bacteria Experience Oxidative Stress? *Environ Microbiol* **2019**, *21* (2), 521–530.

(268) Marcén, M.; Ruiz, V.; Serrano, M. J.; Condón, S.; Mañas, P. Oxidative Stress in *E. Coli* Cells upon Exposure to Heat Treatments. *Int J Food Microbiol* **2017**, *241*, 198–205.

(269) Cabiscol Català, E., Tamarit Sumalla, J., & Ros Salvador, J. Oxidative stress in bacteria and protein damage by reactive oxygen species. *International Microbiology,* **2000**, *vol. 3, núm. 1,* p. 3-8.

(270) Liang, J. Y.; Cheng, C. W.; Yu, C. H.; Chen, L. Y. Investigations of Blue Light-Induced Reactive Oxygen Species from Flavin Mononucleotide on Inactivation of *E. Coli*. *J Photochem Photobiol B* **2015**, *143*, 82–88.

(271) Yang, M. J., Hung, Y. A., Wong, T. W., Lee, N. Y., Yuann, J. M. P., Huang, S. T., ... & Liang, J. Y. Effects of blue-light-induced free radical formation from catechin

hydrate on the inactivation of Acinetobacter baumannii, including a carbapenem-resistant strain. **2018**, *Molecules*, *23*(7), 1631.

(272) Nosaka, Y.; Daimon, T.; Nosaka, A. Y.; Murakami, Y. Singlet Oxygen Formation in Photocatalytic TiO_2 Aqueous Suspension. *Physical Chemistry Chemical Physics* **2004**, *6* (11), 2917–2918.

(273) Li, R.; Jia, Z.; Trush, M. A. Defining ROS in Biology and Medicine. *React Oxyg Species (Apex)* **2016**, *1* (1), 9.

(274) Dharmaraja, A. T. Role of Reactive Oxygen Species (ROS) in Therapeutics and Drug Resistance in Cancer and Bacteria. *J Med Chem* **2017**, *60* (8), 3221–3240.

(275) Hong, Y.; Drlica, K.; Zhao, X. Antimicrobial-Mediated Bacterial Suicide. *Antimicrobial Resistance in the 21st Century* **2018**, 619–642.

(276) Wang, J.; Guo, Y.; Liu, B.; Jin, X.; Liu, L.; Xu, R.; Kong, Y.; Wang, B. Detection and Analysis of Reactive Oxygen Species (ROS) Generated by Nano-Sized TiO_2 Powder under Ultrasonic Irradiation and Application in Sonocatalytic Degradation of Organic Dyes. *Ultrason Sonochem* **2011**, *18* (1), 177–183.

(277) Liao, Y.; Brame, J.; Que, W.; Xiu, Z.; Xie, H.; Li, Q.; Fabian, M.; Alvarez, P. J. Photocatalytic Generation of Multiple ROS Types Using Low-Temperature Crystallized Anodic TiO_2 Nanotube Arrays. *J Hazard Mater* **2013**, *260*, 434–441.

(278) You, D. G.; Deepagan, V. G.; Um, W.; Jeon, S.; Son, S.; Chang, H.; Yoon, H. I.; Cho, Y. W.; Swierczewska, M.; Lee, S.; Pomper, M. G.; Kwon, I. C.; Kim, K.; Park, J. H. ROS-Generating TiO_2 Nanoparticles for Non-Invasive Sonodynamic Therapy of Cancer. *Scientific Reports 2016 6:1* **2016**, *6* (1), 1–12.

(279) Guo, Y.; Cheng, C.; Wang, J.; Wang, Z.; Jin, X.; Li, K.; Kang, P.; Gao, J. Detection of Reactive Oxygen Species (ROS) Generated by TiO_2(R), TiO_2(R/A) and TiO_2(A) under Ultrasonic and Solar Light Irradiation and Application in Degradation of Organic Dyes. *J Hazard Mater* **2011**, *192* (2), 786–793.

(280) Ma, H. Y.; Zhao, L.; Guo, L. H.; Zhang, H.; Chen, F. J.; Yu, W. C. Roles of Reactive Oxygen Species (ROS) in the Photocatalytic Degradation of Pentachlorophenol and Its Main Toxic Intermediates by TiO_2/UV. *J Hazard Mater* **2019**, *369*, 719–726.

(281) Patermarakis, G.; Fountoukidis, E. Disinfection of Water by Electrochemical Treatment. *Water Res* **1990**, *24* (12), 1491–1496.

(282) Liu, L.; Liu, Z.; Bai, H.; Sun, D. D. Concurrent Filtration and Solar Photocatalytic Disinfection/Degradation Using High-Performance Ag/TiO_2 Nanofiber Membrane. *Water Res* **2012**, *46* (4), 1101–1112.

(283) Culotta, V. C. Superoxide Dismutase, Oxidative Stress, and Cell Metabolism. *Curr Top Cell Regul* **2001**, *36* (C), 117–132.

(284) Varnagiris, S.; Urbonavicius, M.; Sakalauskaite, S.; Daugelavicius, R.; Pranevicius, L.; Lelis, M.; Milcius, D. Floating TiO_2 Photocatalyst for Efficient Inactivation of *E. Coli* and Decomposition of Methylene Blue Solution. *Science of The Total Environment* **2020**, *720*, 137600.

(285) Riley, P. A. Free Radicals in Biology: Oxidative Stress and the Effects of Ionizing Radiation. **2009**, *65* (1), 27–33.

(286) Pitzschke, A.; Forzani, C.; Hirt, H. Reactive Oxygen Species Signaling in Plants. *undefined* **2006**, *8* (9–10), 1757–1764.

(287) Mamane, H.; Shemer, H.; Linden, K. G. Inactivation of *E. Coli*, B. Subtilis Spores, and MS2, T4, and T7 Phage Using UV/H_2O_2 Advanced Oxidation. *J Hazard Mater* **2007**, *146* (3), 479–486.

(288) Rubio, C. P.; Cerón, J. J. Spectrophotometric Assays for Evaluation of Reactive Oxygen Species (ROS) in Serum: General Concepts and Applications in Dogs and Humans. *BMC Veterinary Research 2021 17:1* **2021**, *17* (1), 1–13.

(289) Ighodaro, O. M.; Akinloye, O. A. First Line Defence Antioxidants-Superoxide Dismutase (SOD), Catalase (CAT) and Glutathione Peroxidase (GPX): Their Fundamental Role in the Entire Antioxidant Defence Grid. *Alexandria Journal of Medicine* **2019**, *54* (4), 287–293.

(290) Bergamini, C.; Gambetti, S.; Dondi, A.; Cervellati, C. Oxygen, Reactive Oxygen Species and Tissue Damage. *Curr Pharm Des* **2005**, *10* (14), 1611–1626.

(291) Redmond, R. W.; Kochevar, I. E. Spatially Resolved Cellular Responses to Singlet Oxygen. **2006**, *82* (5), 1178–1186.

(292) Jurtshuk, P. Bacterial Metabolism General Concepts Heterotrophic Metabolism
.

(293) Yu, Y.; Wu, K.; Wang, D. Dye-Sensitized Solar Cells with Modified TiO_2 Surface Chemical States: The Role of Ti^{3+}. *Appl Phys Lett* **2011**, *99* (19), 192104.

(294) Kim, S. G.; Dhandole, L. K.; Seo, Y. S.; Chung, H. S.; Chae, W. S.; Cho, M.; Jang, J. S. Active Composite Photocatalyst Synthesized from Inactive Rh & Sb Doped TiO_2 Nanorods: Enhanced Degradation of Organic Pollutants & Antibacterial Activity under Visible Light Irradiation. *Appl Catal A Gen* **2018**, *564*, 43–55.

(295) Raffi, M.; Mehrwan, S.; Bhatti, T. M.; Akhter, J. I.; Hameed, A.; Yawar, W.; Ul Hasan, M. M. Investigations into the Antibacterial Behavior of Copper Nanoparticles against *Escherichia Coli*. *Ann Microbiol* **2010**, *60* (1), 75–80.

(296) Vatansever, F.; de Melo, W. C. M. A.; Avci, P.; Vecchio, D.; Sadasivam, M.; Gupta, A.; Chandran, R.; Karimi, M.; Parizotto, N. A.; Yin, R.; Tegos, G. P.; Hamblin, M. R. Antimicrobial Strategies Centered around Reactive Oxygen Species - Bactericidal Antibiotics, Photodynamic Therapy and Beyond. *FEMS Microbiol Rev* **2013**, *37* (6), 955.

(297) Kumar, S. R.; Imlay, J. A. How *Escherichia Coli* Tolerates Profuse Hydrogen Peroxide Formation by a Catabolic Pathway. *J Bacteriol* **2013**, *195* (20), 4569.

(298) Zhang, L.; Wu, B.; Zhang, G.; Gan, Y.; Zhang, S. Enhanced Decomplexation of Cu(II)-EDTA: The Role of Acetylacetone in Cu-Mediated Photo-Fenton Reactions. *Chemical Engineering Journal* **2019**, *358*, 1218–1226.

(299) Wang, M.; Zhao, Q.; Yang, H.; Shi, D.; Qian, J. Photocatalytic Antibacterial Properties of Copper Doped TiO_2 Prepared by High-Energy Ball Milling. *Ceram Int* **2020**, *46* (10), 16716–16724.

(300) Bensouici, F.; Bououdina, M.; Dakhel, A. A.; Tala-Ighil, R.; Tounane, M.; Iratni, A.; Souier, T.; Liu, S.; Cai, W. Optical, Structural and Photocatalysis Properties of Cu-Doped TiO_2 Thin Films. *Appl Surf Sci* **2017**, *395*, 110–116.

(301) Ebrahimpour, M.; Alipour, H.; Rakhshah, S. Influence of Water Hardness on Acute Toxicity of Copper and Zinc on Fish. *Toxicol Ind Health* **2010**, *26* (6), 361–365.

(302) Liu, T.; Wang, L.; Lu, X.; Fan, J.; Cai, X.; Gao, B.; Miao, R.; Wang, J.; Lv, Y. Comparative Study of the Photocatalytic Performance for the Degradation of Different Dyes by $ZnIn_2S_4$: Adsorption, Active Species, and Pathways. *RSC Adv* **2017**, *7* (20), 12292–12300.

(303) Erdural, B.; Bolukbasi, U.; Karakas, G. Photocatalytic Antibacterial Activity of TiO_2–SiO_2 Thin Films: The Effect of Composition on Cell Adhesion and Antibacterial Activity. *J Photochem Photobiol A Chem* **2014**, *283*, 29–37.

(304) Yu, Y.; Xu, D. Single-Crystalline TiO_2 Nanorods: Highly Active and Easily Recycled Photocatalysts. *Appl Catal B* **2007**, *73* (1–2), 166–171.

APPENDIX

The Experiment of Photocatalytic Dye Degradation

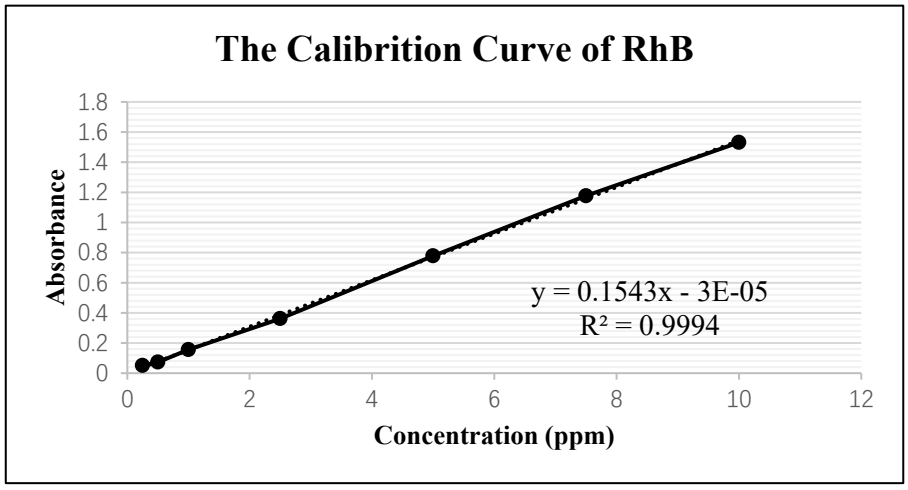

Figure A. 1. The calibration curve for calculating RhB degradation concentration.

Cu ions Leaching Experiment

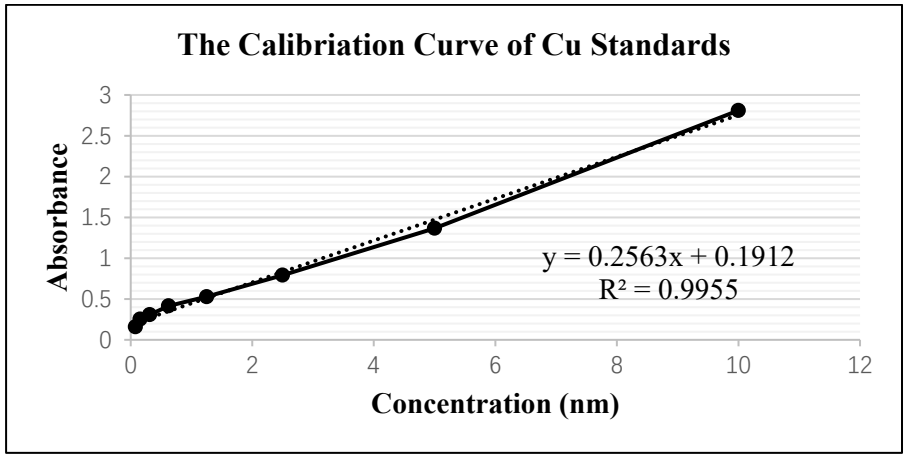

Figure A. 2. The calibration curve for calculating the concentration of Cu ions leaching.